Inland water episodic event management using opensource geospatial and numerical modelling

Thesis for the Degree of Doctor of Philosophy
in
Civil Engineering

Riddick Kakati

186104029

Under the supervision of
Prof. Subashisa Dutta & Prof. Santosha K. Dwivedy

Indian Institute of Technology Guwahati
Guwahati-781039
Assam, India

September 2023

Inland water episodic event management using opensource geospatial and numerical modelling

Riddick Kakati

Department of Civil Engineering
Indian Institute of Technology Guwahati
Guwahati-781039
Assam, India

Doctoral committee

Prof. Arup K. Sarma (Chairman)
Department of Civil Engineering, Indian Institute of Technology Guwahati

Prof. Bimlesh Kumar
Department of Civil Engineering, Indian Institute of Technology Guwahati

Prof. Pankaj Biswas
Department of Mechanical Engineering, Indian Institute of Technology Guwahati

Viva-voce committee

Prof. Arup K. Sarma (Chairman)
Department of Civil Engineering, Indian Institute of Technology Guwahati

Prof. Suresh A. Kartha
Department of Civil Engineering, Indian Institute of Technology Guwahati

Dr. Rajiv K. Kar
School of Health Sciences, Indian Institute of Technology Guwahati

Dr. Soumendra Nath Kuiry
Department of Civil Engineering, Indian Institute of Technology Madras

Thesis examiners

Prof. Sudhanshu Panda
Institute for Environmental Spatial Analysis, University of North Georgia

Dr. Soumendra Nath Kuiry
Department of Civil Engineering, Indian Institute of Technology Madras

Funding sources

MHRD (Government of India) scholarship (July 2018-July 2023)

NAMASTE+ (DAAD) fellowship and research grant at the Georg-August-Universität Göttingen, Germany (October 2022-February 2023)

Field visits and laboratory setup: Technology Innovation Hub, Indian Institute of Technology Guwahati (TIH, IITG)

Synopsis: 16 March 2023 **Viva-voce:** 31 August 2023

ACKNOWLEDGEMENTS

It is an honour and a privilege to be able to thank all of those who helped me finish my dissertation. Firstly, I would like to acknowledge my supervisor, Professor Subashisa Dutta, for everything he's done for me throughout my doctorate program. His tolerance, support, and constructive criticism have been invaluable to my studies and professional development. I am extremely grateful to my co-supervisor, Professor Santosha K. Dwivedy, for his insightful suggestions, helpful feedback, and unwavering support throughout my research. I want to express my profound gratitude to the members of my doctoral committee: Professors Arup K. Sarma, Bimlesh Kumar, and Pankaj Biswas, and to my thesis examiners: Professor Sudhanshu Panda and Dr. Soumendra Nath Kuiry, for their insightful comments, suggestions, and contributions to my research. I am also very thankful to Professor Stefan Siebert and Dr. Neda Abbasi for their help, support, and guidance in my research.

Throughout my doctorate journey, I am indebted to my seniors Dr. Suman Padhee, Dr. Satish Laveti, Dr. Vinay Chembolu, Dr. Chandan Pradhan, and Dr. Anjaneyulu Akkimi for their support, encouragement, and invaluable counsel. Their role as a mentor to me, as well as their direction and motivation, has been really helpful. In addition, I appreciate the help and encouragement of our lab assistant Mr. Bazal Hoque and my other peers and friends Dr. Nandi, Abhishek, Mridupawan, Lasyamayee, Om, Saikat, Avinash, Somesh, Dhritilekha, Shreya, Tori, and Arpita. Their boundless energy, unwavering commitment, and tireless effort have been an endless well of inspiration.

Finally, I want to thank my family, who has been my support and constant motivation during this entire academic process. Their unconditional support, heartfelt affection, and unwavering faith in me have been the rationale for my accomplishments. For all they did for me, taught me, and sacrificed for me, I will be immensely grateful. I appreciate everyone's kind words and encouragement while I worked towards completing my doctorate.

Riddick Kakati/-

-Riddick Kakati

DECLARATION

I, Riddick Kakati, declare that:

- The research work presented in my PhD thesis, titled "Inland water episodic event management using opensource geospatial and numerical modelling" is entirely original and conducted solely by me.
- This thesis has not been submitted for any degree or qualification in any university or institution before.
- Whenever I have used any resources, including theory, concepts, texts, data, graphs, or figures from other sources, I have given proper credit by citing them in the text of my thesis.
- I affirm that my thesis is plagiarism-free to the best of my knowledge, and I take full responsibility for any issues related to plagiarism.
- My thesis supervisors are not responsible for any possible instance of plagiarism in my submitted work.

Riddick Kakati

Place: IIT Guwahati
Date: 31.08.2023

Riddick Kakati
186104029

Indian Institute of Technology Guwahati
Department of Civil Engineering, Guwahati-781039, Assam

CERTIFICATE

This is to certify that the thesis titled **"Inland water episodic event management using opensource geospatial and numerical modelling"** submitted by **Riddick Kakati**, in partial fulfilment of the requirements for the award of the degree of Doctor of Philosophy, to Indian Institute of Technology Guwahati, Assam, India, is a record of the bonafide research work carried out by him under our guidance and supervision at the Department of Civil Engineering, Indian Institute of Technology Guwahati, Assam, India. To the best of our knowledge, no portion of the work described in this thesis has been submitted for the award of any degree at any other institution.

Subashisa Dutta
Professor
Department of Civil Engineering
IIT Guwahati
Guwahati-781039
Assam, India
subashisa@iitg.ac.in

Santosha K. Dwivedy
Professor
Department of Mechanical Engineering
IIT Guwahati
Guwahati-781039
Assam, India
dwivedy@iitg.ac.in

Publications

Journals

I Chembolu, V., Kakati, R., & Dutta, S. (2019). A laboratory study of flow characteristics in natural heterogeneous vegetation patches under submerged conditions. *Advances in Water Resources*, 133, 103418.

II Kakati, R., Chembolu, V., & Dutta, S. (2022). Experimental and Numerical Investigation of Hybrid River Training Works using OpenFOAM. *Water Resources Management*, 36(8), 2847-2863.

Book chapters

I Kakati, R., Chembolu, V., & Dutta, S. (2022). 3D modelling of hybrid river training works. *River Hydraulics: Hydraulics, Water Resources and Coastal Engineering* Vol. 2, 371-377.

II Kakati, R., Chembolu, V., & Dutta, S. (2022). Three-dimensional hydrodynamic modelling of permeable and impermeable river training works using CCHE 3D model and laboratory experiments. *In Recent Trends in River Corridor Management: Select Proceedings of RCRM 2021*, 153-164. Singapore: Springer Nature Singapore.

III Kakati, R., Dwivedy, S.K. & Dutta, S., (2023). Development of a fully automated atmospheric correction technique for applications in Google Earth Engine. *In Recent Development in River Corridor Management: Select Proceedings of RCRM 2022*, 337-348. Singapore: Springer Nature Singapore.

Contribution report

Except Journal Paper I, all the publications mentioned above are mainly the work of the author. Journal Paper I is the main work of Chembolu, V. where the author contributed with the development of laboratory setup used for testing of nature based river management solutions. The same setup was used for calibration and validation of the hydrodynamic model, that was used for performance evaluation of engineered river training works as compared to natural mangrove structure.

Conferences

- **Hydro 2018, NIT Patna, India**
  Kakati, R., Chembolu, V., & Dutta, S. 3D Modelling of Hybrid River Training Works. NIT Patna. Oral Presentation, 19-21 December 2018.
- **International Conference on River Corridor Research and Management (RCRM 2021), IIT Jammu & IIT Guwahati, India**
  Kakati, R., Chembolu, V., & Dutta, S. Three-Dimensional Hydrodynamic Modelling of Permeable and Impermeable River Training Works using CCHE 3D Model and Laboratory Experiments. IIT Jammu & IIT Guwahati. Oral Presentation, 25-27 February 2021.
- **American Geophysical Union (AGU 2021), New Orleans, LA, USA**
  Kakati, R., Dutta, S & Dwivedy, S.K. Real Time Mapping of Chlorophyll-a in the Brahmaputra River using Google Earth Engine. New Orleans, LA, USA. Poster Presentation, 13-17 December 2021.
- **2nd International Conference on River Corridor Research and Management (RCRM 2022), IIT Guwahati & IIT Jammu, India**
  Kakati, R., Dutta, S & Dwivedy, S.K. Development of a fully automated atmospheric correction technique for applications in Google Earth Engine. IIT Guwahati & IIT Jammu. Oral Presentation, 30 May-1 June 2022.
- **Two-day Pre-Event of 2nd UN-WGI Congress 2022 (Online), Gauhati University, Guwahati, Assam, India**
  Kakati, R., Dutta, S & Dwivedy, S.K. Satellite based hydro-ecological processes modelling in Brahmaputra river. Gauhati University, Guwahati, Assam, India. Oral Presentation, 23-24 June 2022.
- **American Geophysical Union (AGU 2022), Chicago, IL, USA**
  Kakati, R., Dutta, S & Dwivedy, S.K. Cloud based prediction of water depths in the Brahmaputra River using optical imagery from Sentinel 2. Chicago, IL, USA. Poster Presentation/Oral Presentation at the Google Booth, 12-16 December 2022.
- **European Geophysical Union (EGU 2023), Vienna, Austria**
  Kakati, R., Dutta, S & Dwivedy, S.K. Performance of natural mangrove structure in downstream velocity reduction as compared to engineered porcupine and geobag structure using OpenFOAM. Vienna, Austria. Poster Presentation, 23-28 April 2023.

Abstract

Inland water episodic events are rapid and transient changes in the typical conditions of rivers, lakes, or other bodies of freshwater caused by floods, droughts, heatwaves, or other extreme weather conditions, as well as pollution, industrial accidents, and other human activities. The aim of this study is to devise a system for monitoring and managing such events by focusing on natural solutions based on riparian vegetation, which plays an important role in preserving ecological balance and water quality, strengthening riverbanks, providing habitats for numerous species, regulating stream temperature, and cycling nutrients. For efficient analysis and customized data representation, as well as to leave room for future improvements and modifications in the source codes, an opensource approach has been employed.

Firstly, an attempt has been made to model episodic events in terms of range of values shown by proxy water quality and riparian vegetation quantity/health indicators. To analyze and process raw satellite data for acquiring these information, a cloud computing Google Earth Engine (*GEE*) based web-*GIS* application has been developed. The graphical user interface allows for a code-free interface that can process data and generate results on any device platform with a standard internet connection. In the absence of atmospherically corrected level 2 surface reflectance products, which is a necessity prior to data processing, raw satellite imageries can be used to generate results with the use of a state-of-the-art fully automated Dark Object Subtraction based approximate atmospheric correction technique. When compared to the Level 2 surface reflectance product, it achieved similar results in terms of image-based land use/land cover classification accuracy.

In addition, it provided a good estimate of the range of derived water quality parameters for the river Ganga in India, when compared to reported field measurements. Using Level 2 data, this application was further used to examine the temporal patterns of river influence on riparian vegetation along the Iranian and Indian rivers Zayandeh-Rood and Brahmaputra respectively. In the non-riparian zone of Iran (overall accuracy of 86%; Cohen Kappa score of 69%) and India (overall accuracy of 92%; Cohen Kappa score of 86%), there was a high correlation between $NDVI$ and $GNDVI$. Similar findings were obtained for riparian vegetation zones in Iran (overall accuracy of 97%; Cohen Kappa score of 94%) and India (overall accuracy of 100%; Cohen Kappa score of 100%), indicating that the two indices are highly correlated. These indices can be used to estimate the amount of nutrients in a system. In addition, nutrient exchanges as a result of interactions between river and riparian vegetation zones have been observed. These are continuous and cyclic processes that play

a significant role in regulating the health and quantity of vegetation, thereby sustaining the river ecosystem.

For a detailed analysis of these proxy based nutrient exchanges, a three-dimensional hydrodynamic opensource model (*OpenFOAM*) has been used to simulate water flow on a laboratory scale. Firstly, to test its effectiveness, the performance of the model has been compared with a commercial model (*CCHE3D*). The *OpenFOAM* model has been found to be much effective in this case when engineered river training works *viz.*, porcupine, and a geobag layout are modelled. Previous research indicated that the permeable river training works such as porcupines are a popular and cost-effective option for braided river training. In times of extreme inundation, however, these structures frequently fail to perform adequately. On the other hand, impermeable structures such as geobags have the problem of scour holes forming at the nose. In light of the preceding, this study also tested a novel hybrid layout that incorporates both impermeable and permeable river training works. Validation with experimental flume data, yielded fairly acceptable results (R^2 >74%). Additionally, it was observed that efficacy of the hybrid layout can be enhanced by decreasing the gap between the permeable and impermeable structures, thereby enabling them to operate as a cohesive entity.

As a nature-based alternative to these engineered structures, for the first time, a commonly seen riparian vegetation type (mangrove) has been further simulated to study the induced secondary currents and velocity gradients within the flow. It has been found that these generated secondary currents and velocity gradients form a mechanism that might drive the nutrient exchanges. The hybrid layout reduces downstream velocity 1.33%, 11.62%, and 13.34% better than the geobag, dual-screen porcupine, and single-screen porcupine respectively. In terms of velocity increase at the deflection zone, the hybrid layout is 0.49%, 0.65%, and 0.92% more efficient. Compared to hybrid layout, mangrove structure further reduces flow velocity by 0.75% and deflects by 1.09%. The magnitude of secondary currents for the mangrove structure is also found to be the highest. These findings indicate that through the utilisation of suitable input and boundary conditions, modelling studies can effectively facilitate the planning of river training interventions. Computer modelling can aid in the effective and sustainable management of water resources for dynamic rivers such as the Brahmaputra and the Ganga. Furthermore, modelling an optimal river training layout and testing its efficacy in mitigating bank erosion and pollution control prior to implementation can be very beneficial for efficient water resources management.

Contents

List of Figures

List of Tables

List of abbreviations

A: Agriculture class in image classification
$AISA$: Airborne Imaging Spectrometer for Applications space program
ALI: Advanced Land Imager space program
$ALOS$: Advanced Land Observing Satellite space program
ANN: Artificial Neural Network
API: Application Programming Interface
$ASTER$: Advanced Spaceborne Thermal Emission and Reflection Radiometer space program
ATM: Airborne Thematic Mapper
$AVHRR$: Advanced Very High Resolution Radiometer space program
$AVNIR$: Advanced Visible and Near Infrared Radiometer space program
B: Barren land class in image classification
$blockMesh$: Module for mesh generation in *OpenFOAM*
BOD: Biochemical Oxygen Demand
CAD: Computer Aided Design
$CASI$: Compact Airborne Spectrographic Imager space program
$CCHE$: Hydrodynamic model developed by the National Center for Computational Hydroscience and Engineering Mississippi
$CDOM$: Colored Dissolved Organic Matter
CFD: Computational Fluid Dynamics
$Chl-a$: Chlorophyll-a
CNN: Convolutional Neural Network
COD: Chemical Oxygen Demand
$COST-DOS$: Dark Object Subtraction with a Fourier series approximation for the cos of solar zenith angle $\{\cos(\theta_z)\}$
$COVID$: Novel Corona Virus Disease
$CZCS$: Coastal Zone Color Scanner space program
DES: Detached Eddy Simulation turbulence model
DN: Digital Number
DO: Dissolved Oxygen
DOS: Dark Object Subtraction
EMR: Electromagnetic Radiation
EO: Earth Observation
$ETM+$: Enhanced Thematic Mapper Plus space program
EVI: Enhanced Vegetation Index
F: Forest class in image classification
$FLUENT$: Fluid Flow Analysis System developed by Analysis of Systems finite element analysis software ($ANSYS$)
$FreeCAD$: An opensource CAD designing software
GEE: Google Earth Engine
$GEEApps$: Google Earth Engine Application Development Platform
$GIMP$: GNU's Not Unix (GNU) Image Manipulation Program
GIS: Geographic Information System
$GNDVI$: Greenness Normalized Difference Vegetation Index
GUI: Graphical User Interface
$HEC-RAS$: United States Army Corps of Engineers River Analysis System
$HyspIRI$: Hyperspectral Infrared Imager
IDE: Integrated Development Environment

$IPCC - AR5 - RCP$: Intergovernmental Panel on Climate Change Assessment Report for Representative Concentration Pathway
IRS: Indian Remote Sensing space program
JavaScript: A computer programming language
kqRwallFuntion: Wall boundary condition module in *OpenFOAM*
$HICO$: Hyperspectral Imager for the Coastal Ocean space program
$IKONOS$: An earth observation satellite
$LANDSAT$: *LANDSAT* space program
$LISS$: Linear Imaging and Self Scanning Sensor space program
LES: Large Eddy Simulations turbulence model
mask: A built in function of *GEE* used to filter pixels
$MASTER$: *MODIS/ASTER* airborne simulator
Matplotlib: Package for creating visualizations in *Python*
$MERIS$: Medium Resolution Imaging Spectrometer space program
$MIKE21C$, $MIKE21fm$: Two-dimensional hydrodynamic models developed by Danish Hydraulic Institute (*DHI*)
$MNDWI$: Modified Normalized Difference Water Index
$MODIS$: Moderate Resolution Imaging Spectroradiometer space program
MSS: Multispectral Scanner
MWR: Microwave Radiometers
$NDCI$: Normalized Difference Chlorophyll Index
$NDTI$: Normalized Difference Turbidity Index
$NDVI$: Normalized Difference Vegetation Index
$NDWI$: Normalized Difference Water Index
NIR: Near Infrared
NumPy: Package for scientific computing with *Python*
OLI: Operational Land Imager
OOP: Object Oriented Programming
OpenFOAM: Open Field Operation and Manipulation hydrodynamic model
Pandas: Package for data analysis and manipulation with *Python*
ParaView: An application for interactive and scientific visualization
$PROBA - CHRIS$: Compact High Resolution Imaging Spectrometer on *PROBA* space program
Python: A computer programming language
QA: Quality Assessment
QP: Quadratic Programming
R: River class in image classification
$RANS$: Reynolds Averaged Navier Stokes equations
RF: Random Forest
RTC: Radiative Transfer Code
$SAC - D$: Satélite de Aplicaciones Científicas-D (*Aquarius*) space program
$SeaWIFS$: Sea viewing Wide Field of view Sensor space program
Sentinel: *Sentinel* space program
Signum: A built in function of *GEE* used to process images
$SIMPLE$: Semi-Implicit Method for Pressure Linked Equations
simpleFOAM: *SIMPLE* model in *OpenFOAM*
$SLFMR$: Scanning Low Frequency Microwave Radiometer

SMOS: Soil Moisture and Ocean Salinity space program
snappyHexMesh: Mesh refinement module in *OpenFOAM*
SPOT: Satellite pour l'Observation de la Terre space program
SST: Sea Surface Temperature/Shear Stress Transport
STARRS: States and Regions Remote Sensing space program
stl: Stereolithography, a file format for digital three-dimensional objects
SVM: Support Vector Machines
TIRS: Thermal Infrared Sensor
TM: Thematic Mapper
U: Urban land class in image classification
UAV: Unmanned Aerial Vehicle
USEPA: United States Environmental Protection Agency
USGS: United States Geological Survey
W: Wetland class in image classification

List of symbols

%: Percentage
α, β, α_1, β_1, α_2, β_2: Constants in $\kappa-\varepsilon$, $\kappa-\omega$, and $\kappa-\omega$ SST turbulence models
ε, ω: Turbulence specific dissipation rate
κ: Turbulence kinetic energy
μm: Micrometer (micron)
ν: Fluid kinematic viscosity
ν_t: Turbulence viscosity
ρ, ρ_i: Pixel surface reflectance
ρ_f: Discharge
τ_{vi}: Atmospheric transmittance from the ground surface to satellite
τ_{zi}: Atmospheric transmittance from sun to the ground surface
θ_z: Sun zenith angle
C_i: i^{th} class
d_{50}: Particle size finer than 50% in particle size distribution
DN, DN_i: Digital number
E_{down}: Surface downwelling spectral irradiance due to scattered solar flux in the atmosphere
E_o: Solar spectral irradiance of the sun on a perpendicular surface outside the atmosphere
$f\left(C_i, T\right)/|T|$: Probability that the example belongs to class C_i
F_1, F_2: Blending functions
G_i: Gain factor
H: Porcupine height
H_i: Path radiance
$H.P.$: Horsepower
Hz: Hertz
i, j: Unit vectors
L_λ: Pixel radiance
O_i: Offset
Kg: Kilogram
km: Kilometer
m: Meter
N: Number of trees
R^2: Coefficient of regression
s: Seconds
sr: Steradian
t: Time
T: Training set
u: Velocity magnitude at the measured location
U_{avg}: Depth averaged velocity
W: Weber
x, y, z: Coordinate axes
X, Y: Pixel location coordinates
y': Depth of measurement location from the flume bed
Y_{max}: Total flow depth

Preface

India is blessed with an abundant and rich water supply. Despite a vast and intricate network of rivers, lakes, groundwater, and reservoirs supplying water for various uses, the system nevertheless struggles with water scarcity (droughts) and excess availability (floods) due to the asymmetry in the distribution of water. In addition, there is always the problem of water pollution. Moreover, economic constraints, difficult environmental conditions, and the dynamic nature of the rivers make it difficult to conduct frequent field surveys to monitor these rivers. Effective solutions for water management and cost-efficient technology for continuously monitoring rivers are essential for addressing these episodic events. The aim of this study is to develop such a system for near real time monitoring. In terms of management, this study emphasizes the adoption of natural solutions based on riparian vegetation.

Thesis objectives

The following objectives have been established for this study in light of the research needs, which require an understanding of the natural hydrodynamic and ecological processes that sustain the river ecosystem and its alterations connected with anthropogene:

- Development of a Google Earth Engine (*GEE*) cloud computing based global near real time integrated hydro-ecological inland water monitoring system
- Understanding the coupling between the river and its surrounding riparian vegetation zones in maintaining the river ecosystem, and managing its episodic events using proxy indicators
- Using the three-dimensional hydrodynamic *OpenFOAM* model to comprehend the proxy based nutrient exchange mechanisms between a river and its surrounding riparian vegetation zones

Thesis outline

There are five chapters detailing the research presented in this thesis. Field, laboratory, satellite, and hydrodynamic modelling-based techniques have been incorporated to investigate the nutrient exchange mechanisms at play between the riparian vegetation zones and the surrounding river systems. Each chapter of the thesis is dedicated to one or more specific research objectives described in the previous section. At first, a real time hydro-ecological monitoring satellite-based web-*GIS* application has been developed on the opensource

GEE cloud computing platform, and validated with the Indian rivers of Ganga and Brahmaputra. This application has then been utilised in the Indian rivers of Ganga and Brahmaputra, along with the Iranian river Zayandeh-Rood to map the river-floodplain nutrient exchanges, and its time lagged response in vegetation quantity/health. Further, to understand the physics behind these phenomena, a detailed study has been conducted using three-dimensional hydrodynamic opensource *OpenFOAM* model, which has been calibrated and validated with data from laboratory experiments. Each chapter of the thesis is comprehensively outlined below:

- **Chapter 1: Background and Motivation**
  This chapter discusses in brief the contemporary techniques for monitoring water quality, as well as the need for research. Every subsequent chapter of this thesis that deals with a specific objective includes its own in-depth literature review.
- **Chapter 2: Web-GIS application development**
  This section details the methodology for the development of the near real time hydro-ecological monitoring interface.
- **Chapter 3: Understanding hydro-ecological exchange mechanisms**
  This chapter deals with mapping nutrient transfer processes between river and its riparian vegetation zones.
- **Chapter 4: Modelling hydro-ecological interactions**
  This chapter describes the turbulence characteristics generated by riparian vegetation structure (mangrove) and its comparison with engineered river training structure in preventing river bank erosion and controlling pollution.
- **Chapter 5: Conclusions and future scope**
  This chapter summarises the findings and proposes the prospects for the future.

An effort to promote open research...

1

Background and Motivation

An introduction to the rivers Ganga, Brahmaputra and the Zayandeh-Rood, followed by a literature review on inland water management in terms of river training, ecological modelling and research gaps

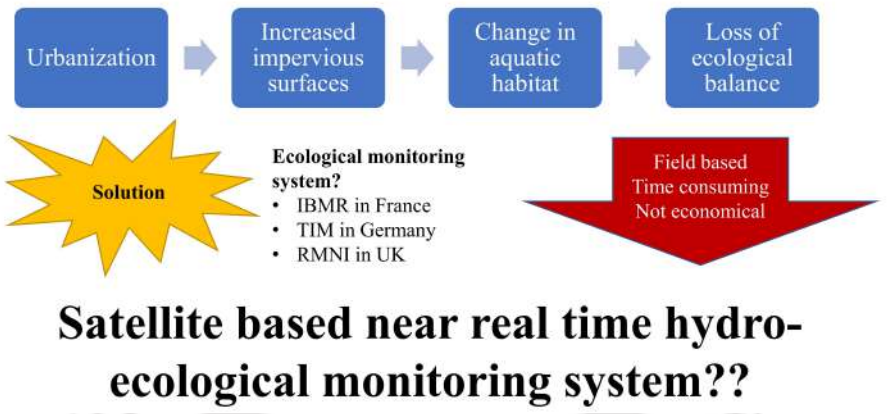

Contents

1.1 General

This chapter discusses the research problem of this study, and it has been presented gradually through a brief literature review of each of the objectives. The first section gives an overview of the research problem and the selected study areas. It is followed by the section on current river bank erosion management principles. The next section outlines various techniques that have been employed till date in ecological modelling. Then, a discussion on the research gaps, along with the need for the research have been presented. Finally, the chapter ends with a summary, which is also its final section.

1.2 Introduction

The fundamental premise of ecological theory states that, the environment has an effect on all living things (Kemmerer and Butler, 1977). With increasing anthropogenic activities causing changes in riverine habitats, which have served as a lifeline to humanity since the dawn of civilization, there is a need for real-time monitoring to enable necessary management strategies. To meet this requirement, a web-*GIS* application was developed and tested on three major rivers: the Ganga and Brahmaputra in India, which experience monsoon weather, the Zayandeh-Rood in Iran, which experiences dry weather. Due to its near real time monitoring capabilities, the application can also be used for episodic event management.

The Brahmaputra River is a transboundary river that originates in the Tibetan Himalayas and flows for approximately 2,900 km before discharging into the Bay of Bengal. It flows through China, India, and Bangladesh and is known for its unique ecosystem that supports a diverse range of biodiversity. The river provides water for irrigation, transportation, and fishing for millions of people in the region and supports many endangered species, including the Gangetic dolphin, and the one-horned rhinoceros (Borah et al., 2010; Pradhan et al., 2021). The Ganga, also known as the Ganges, is a sacred river in India that originates in the Himalayas and flows for about 2,525 km before flowing into the Bay of Bengal. It is India's most important river, providing water to millions of people while also supporting agriculture and industry. However, the river has been severely polluted by industrial and human waste (Figure 1.1), posing health risks and environmental issues (Dwivedi et al., 2018). The

Zayandeh-Rood is a river in central Iran that has played a significant role in the region's history and culture. The river is approximately 400 km long and flows through the city of Ishfahan. It is a vital source of water for the region's agriculture and industry. In recent years, the Zayandeh-Rood has also faced water scarcity and pollution problems (Figure 1.1), resulting in environmental and social issues (Neysiani et al., 2022). Overall, these three rivers highlight the importance of riverine habitats and the need for effective management strategies to address the impact of anthropogenic activities.

Figure 1.1: News articles reporting pollution in the river Ganga and consequences of anthropogenic interferences in the river Zayandeh-Rood

1.3 Inland water management

From 1920 to 1998, the largest riverine island Majuli in Assam, India, experienced an annual erosion rate of 1.9 km^2 (Kotoky et al., 2003). Extreme sediment load movement, meandering, and sand bar formation in the middle of rivers are all results of erosion, which is mostly attributable to energy dispipation mechanisms due to natural and anthropogenic changes (Karmaker and Dutta, 2016; Chembolu et al., 2019; Pradhan et al., 2022; Nandi et al., 2022). Previous studies on river bank erosion and protection show that in large rivers, where many morphological and hydrodynamic changes are observed, flow deflectors such as dikes (spurs) and bendway weirs are the most adaptable river bank protection strategies (Yoo, 2003). The most common forms of river bank protection in big alluvial rivers include stone pitching, gabions, rock riprap, retaining walls, bend weirs, and spurs (Julien, 2018). Low-cost alternatives, such as porcupine screens, which moderately reduce flow velocities, are often employed in underdeveloped countries like India and Bangladesh (Aamir and Sharma, 2015). The rivers' response to the intervention, the structures' design and proportions, and the significance of the region to be protected all play a

role in determining the type of river training work that must be undertaken (Sarker et al., 2011; Karmaker and Dutta, 2016). To simulate the morphological change processes of alluvial streams, numerical models have been utilised in the study of channel flow and morphology (Jia and Wang, 1999; Karmaker and Dutta, 2016).

Finding environmentally friendly solutions to the challenges of river bank erosion is important in light of the requirement for sustainable development. Plantations of vegetation on river banks can significantly reduce flow velocity. Järvelä (2002) conducted comprehensive studies to analyse the flow resistance produced by natural plants and discovered that the flow resistance provided by natural plants is dependent on flow conditions. Wilson et al. (2003) carried out thorough laboratory tests to investigate the flow structure of submerged flexible vegetation with and without frond foliage and discovered that vegetation with frond foliage prevented turbulent mixing at the canopy top, hence reducing erosion and scour. Flume studies conducted by Järvelä (2005) revealed that the flow structure and turbulence features in natural flexible vegetation (wheat) followed a logarithmic profile, with the maximum value of Reynolds' stresses and turbulence intensity recorded at the canopy top. According to a series of experiments conducted by Wilson (2007) on both artificial and natural flexible grasses in a submerged environment, the roughness coefficient is largely dependent on plant height. When studying the mixing mechanisms in vegetated open channel flows, Shucksmith et al. (2010) found that longitudinal mixing was greater in submerged than in emergent vegetation. Ortiz et al. (2013) conducted laboratory tests to investigate the impacts of mean and turbulence flow structure surrounding circular patch of vegetation on suspended sediment depositions and discovered that flow adjustment was two-dimensional in emergent vegetation and three-dimensional in submerged vegetation with shear layers in horizontal and vertical planes, and that in emergent vegetation there was an area of stable wake zone behind the patch, resulting in enhanced deposition with less mean velocity and turbulent kinetic energy. Devi and Kumar (2015) conducted a series of laboratory experiments on a staggered vegetative bed to explore flow characteristics along the channel and discovered that the velocity drops by up to 15% as the flow moves from upstream to downstream, with more erosion occurring at the upstream vegetative portion than downstream. Devi et al. (2016) conducted a series of tests to explore the drag and turbulence features of mixed plant density over a mobile bed channel with downward seepage and discovered that the presence of seepage increased the velocity near the bed and corresponding turbulence parameters, and that higher vegetation density downstream reduced sediment movement, which can be beneficial for river restoration projects. Using controlled laboratory experiments, Chembolu et al. (2019) and Modalavalasa et al. (2023) found that the shape and alignment of vegetation patches, as well as the way these patches interacted with the

secondary currents of the flow, significantly influenced the rivers' overall velocity patterns and momentum exchanges.

1.4 Ecological modelling

There have been numerous ecological studies in which ecological parameters were related to physical parameters (Kemmerer and Butler, 1977; Gitelson, 1992; Gitelson et al., 1993; George, 1997; Karaska et al., 2004; Burtenshaw et al., 2004; Kobara and Heyman, 2007; Gitelson et al., 2008; Olmanson et al., 2013). Various remote sensing technique exists, which can be used to map various ecological parameters (Table 1.1). The ocean-colour sensors can detect signals from below the surface due to the greater penetration of visible radiation, and this characteristic can be exploited to predict time series of chlorophyll images. Thermal or chlorophyll fronts often indicate areas of high biological productivity. Chlorophyll can then related to phytoplankton biomass, which is the primary food source within water bodies.

Remote sensing techniques have been widely used to estimate concentrations of water quality constituents, including chlorophyll, dissolved organic matter, and suspended matter (Table 1.2). Kemmerer and Butler (1977) used remote sensing to locate fish by analyzing water color, turbidity, chlorophyll, and other factors. Gitelson (1992) and Gitelson et al. (1993) developed algorithms for remote sensing of water quality by collecting data on reflectance spectra and water quality constituent concentrations. George (1997) tested established chlorophyll retrieval algorithms for Class 1 waters and developed maps showing the spatial distribution of phytoplankton in larger lakes in the English Lake District. Han and Rundquist (1997) conducted experiments using the NIR/red ratio to estimate chlorophyll content in a relatively cloudy mid-western reservoir. Using *LANDSAT* Thematic Mapper (*TM*) data collected at two separate times, Brivio et al. (2001) calculated the distribution of phytoplankton chlorophyll concentrations in Lake Garda (Italy). Hedger et al. (2002) used remote sensing alongside a computational fluid dynamics and ecological model to examine the spatial distribution of Chlorophyll- a (*chl-a*). Spectral indices were developed by Shafique et al. (2003) using correlations between ground-truth data and spectral bands to estimate *chl-a*, turbidity, and phosphorus. Tyler et al. (2006) used a linear mixture modelling approach to derive accurate estimates of *chl-a* from *LANDSAT TM* imagery in waters with high and heterogeneous concentrations of suspended sediment. Hunter et al. (2008) examined the spectral dissimilarities of four major phytoplankton color groups and developed simple spectral indices to quantify the concentration

of potential biomarker pigments. Water temperature, *chl-a*, and total soluble solids were analyzed by Bresciani et al. (2009) using remote sensing techniques in three shallow eutrophic lakes. Jutla et al. (2011) examined the correlation between Sea Surface Temperature (*SST*), phytoplankton abundance, and cholera outbreaks in coastal waters of the Bay of Bengal, and found that coastal phytoplankton blooming occurred during high river discharges with terrestrial nutrients. Reese et al. (2011) concluded that *SST* fronts in a coastal upwelling system provided an important habitat feature for fishes.

Olmanson et al. (2013) used hyperspectral imagery to create pixel-level maps for three major rivers and identified spectral characteristics to develop models to map water quality characteristics. Tamminga et al. (2015) used a *UAV* to characterize the channel morphology and hydraulic habitat of a river in Canada. Using satellite remote sensing data, Wolanin et al. (2015) presented and compared the retrieval of chlorophyll fluorescence from hyperspectral instrument measurements. According to an analysis conducted by Hestir et al. (2015), the *HyspIRI* mission is ideally suited for accurately measuring a wide range of biophysical variables, making it an ideal candidate for use in measuring freshwater ecosystems. Kar et al. (2016) used hyperspectral remote sensing to identify the spatial variability of metal pollutants in a river in India and developed a multivariate regression analysis to assess the varying concentrations of metal ions present in water based on the spectral depth of the corresponding absorption feature. Nurdin et al. (2017) used fishing-catch data and satellite data of *chl-a* and *SST* to identify the relationship between fish distribution and *chl-a*/*SST*, detect potential fishing grounds, and determine the impact of climate change on fish distribution based on temperature projections of *IPCC-AR5-RCP*s in 2017, and found that the ecological habitat was significantly associated with the preferred range of *chl-a* and *SST* in the archipelagic waters of Spermonde.

1.5 Research gaps and need for research

From the previous studies, it has been observed that very few studies have been conducted to study the response of natural vegetation in influencing the hydrodynamic and ecological characteristics of rivers. Due to complex and dynamic nature of Himalayan rivers in India, it is difficult to conduct field as well as scaled down physical model studies. Also, very few research works have been done, and limited publications have focused on their complexity. The numerical methods used for modelling river training works can be used for understanding the hydrodynamic response of riparian vegetation based

natural solutions. Further, utilizing the vegetation resistance properties, which depends on its structure and also its level of submergence, an optimal natural bank erosion protection layout can be designed from these numerical modelling simulations.

In terms of modelling of ecological characteristics, satellite remote sensing has been used in many previous studies, but most of the time optical satellite imageries in India are covered with cloud, so appropriate atmospheric correction scheme must be applied before processing the images for water quality parameters. During certain periods of time, level 2 surface reflectance products are also not available. Further, all the previous studies have only considered either terrestrial, or aquatic ecological parameters, and there are no studies based on satellite remote sensing that have simultaneously mapped both. There is a need for a robust near real time ecological monitoring system, that will result in effective and sustainable river management. The aim of this research is to design an opensource integrated river hydro-ecological management framework (Figure 1.2) using satellite based and numerical modelling techniques. A near real time monitoring system will also aid in managing episodic events.

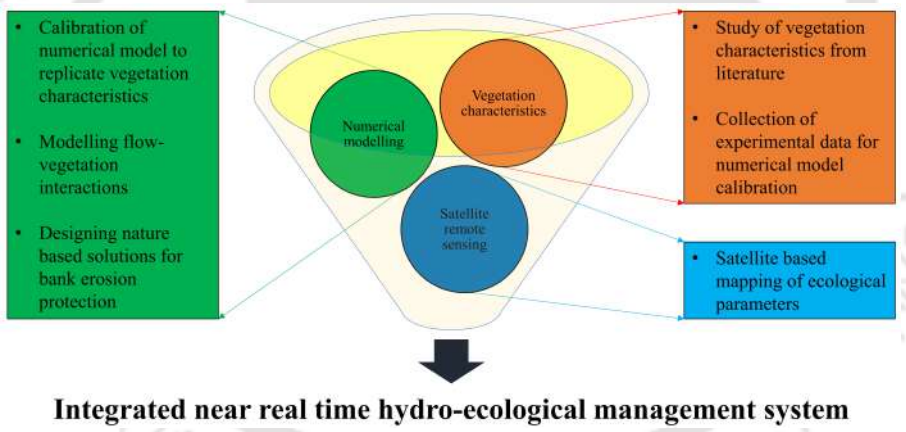

Figure 1.2: Components of the integrated real time hydro-ecological management system

1.6 Summary

This study aims to design an open-source integrated river hydro-ecological management framework using satellite based and numerical modelling techniques. It has been observed that very few studies have been conducted on the

response of natural vegetation in influencing the hydrodynamic and ecological characteristics of rivers, particularly in the complex and dynamic Himalayan rivers of India. Utilizing the vegetation structural properties, an optimal natural bank erosion protection layout can be designed from numerical modelling simulations. Satellite remote sensing has been used in many previous studies to model ecological characteristics, but most of the time, optical satellite imageries in India are covered with clouds, and an appropriate atmospheric correction schemes must be applied before processing the images for water quality parameters. Therefore, a robust near real time ecological monitoring system is needed for effective and sustainable river management, which can also aid in managing episodic events.

Table 1.1: Ocean remote sensing sensors (Klemas, 2012)

Sensor	Parameters
Color scanner	Ocean color (Chlorophyll concentration, suspended sediment, attenuation coefficients)
Infrared radiometer	Sea surface temperature (surface temperature, current patterns)
Synthetic aperture radar	Short waves (swell, internal waves, oil slicks, etc.)
Altimeter	Topography and roughness of sea surface (sea level, currents, wave height)
Scatterometer	Amplitude of short surface waves (surface wind velocity, roughness)
Microwave radiometer	Microwave brightness temperature (salinity, surface temperature, water vapour, soil moisture)

Table 1.2: Satellites used for ocean remote sensing (Klemas, 2012; Franz et al., 2015; Liu et al., 2021)

Sensor	Agency	Satellite	Operating dates	Spatial resolution (m)	Number of bands	Spectral coverage (nm)
CZCS	NASA	Nimbus-7	1978-1986	825	6	433-12,500
SeaWIFS	NASA	Orb View-2	1997-2010	1,100	8	402-885
MODIS-Terra	NASA	Terra	Launch 1997	250/500/1000	36	405-14,385
MODIS-Aqua	NASA	Aqua	Launch 2002	250/500/1000	36	405-14,385
MERIS	ESA	Envisat-1	Launch 2002	300/1200	15	412-1,050
VIIRS	NASA	SuomiNPP	Launch 2011	370/740	22	412-12,013
OLI	USGS	LANDSAT 8/9	Launch 2013	30	11	4.33×10^{-7}-1.251×10^{-5}
OLCI	ESA	Sentinel 3	Launch 2016	300	21	4.00×10^{-7}-2.280×10^{-6}

2

Web-GIS application development

This chapter describes the detailed methodology for the development of the Google Earth Engine cloud computing web-GIS application interface

Contents

2.1 General

To carry out the data processing in this study, a web-*GIS* application was developed. This chapter details the methodology adopted for its development. The first section presents a review of literature on various atmospheric correction models that can be adopted for raw satellite imagery processing, followed by a brief overview of the methodology. Then, the detailed procedure has been described in the section called "Methodology". The following section discusses the results obtained. Next comes the discussion of the results. Finally the chapter ends with a summary section.

2.2 Introduction

A variety of earth monitoring applications, including the assessment of the global energy balance and the detection of changes in land cover, have long advocated the use of satellite imagery. Problems arise due to the presence of the atmosphere because solar Electromagnetic Radiation (*EMR*) reflected by the Earth and measured by the detectors in the satellite must travel through its way from the sun to the Earth and back. When *EMR* travels through the atmosphere, it comes into contact with molecules of the various gases and the particles that make up the atmosphere. Scattering and absorption are the two basic processes that are often used to characterize this interaction (Lillesand et al., 2015). *EMR* undergoes a transformation when it interacts with Earth's surface. During this process, path radiance refers to emitted radiation that does not interact with the earth before entering detectors. This path radiance is typically undesirable information since it tells nothing about the character of the land surface (Adams and Gillespie, 2006; Gao, 2009). Water and vegetation, which are not as reflective as other surfaces, have a greater effect on the atmosphere. This is a particularly serious issue for applications that rely on multi-spectral satellite data for monitoring, including those in agriculture and land use research. It affects the quantity of *EMR* perceived by the array of detectors in a satellite, which changes with wavelength (Chavez Jr, 1988; Chavez et al., 1996; Mustak, 2013; Lillesand et al., 2015). Thus, atmospheric correction is necessary, particularly for Rayleigh scattering generated by gases, water vapour and aerosols which affects the bands near the visible part of the electromagnetic spectrum (Mustak, 2013).

The data from the sensor called digital number (DN), needs to be free from the atmospheric interferences, which can be achieved through the generation of surface reflectance, which normalises data from different time periods and sources. Radiative transfer codes (RTC) help in determining an accurate relationship between surface reflectance and radiance of the sensor by the use of atmospheric optical depth on the date of satellite pass (Moran et al., 1992). An RTC with realistically simulated atmospheres may be used instead of actual weather data when actual data is unavailable. For a variety of simulated atmospheres, aerosol kinds, sun zenith angles, and ground altitudes, Richter (1990) proposed employing a library of atmospheric correction functions created using an RTC to predict surface reflectance. For situations when no atmospheric data is available, this library might allow for rapid analysis of satellite images. Using a $N \times N$ pixel window and suitable weighting factors for the difference in reflectance, it further enhanced the estimate by approximating a correction for the adjacency effect. But the high cost and prolonged implementation process associated with an RTC makes it challenging for applications, which require rapid and frequent generation of processed data.

There have been a number of proposals for easier atmospheric correction techniques for images in the visible and near infrared spectra that are gathered by satellites (Otterman and Fraser, 1976; Singh, 1988; Dozier and Frew, 1981; Kneizys, 1988). The amount and precision of atmospheric data needed to apply a simplified technique varies widely, and very few procedures may be used when no atmospheric data is available. To save the hassle of taking separate readings of the atmosphere and the site itself, it is also possible to extrapolate information about atmospheric conditions from the image itself. Surface reflectance factors are often retrieved using scene-derived atmospheric information in conjunction with an RTC, in image-based atmospheric correction methods. In order to estimate path radiance, Ahern et al. (1977) used a clear lake in the image, and then used a radiative transfer algorithm to deduce atmospheric transmittance and downwelling irradiance from this estimate. Recently, several investigations have relied on the Dark Object Subtraction (DOS) approach, which is a simplified version of this technique (Ding et al., 2015; Mustak, 2013; Wicaksono and Hafizt, 2018; Li et al., 2022).

The DOS technique eliminates the requirement for radiative transfer coding by subtracting the path radiance from the scene's darkest object, which need not be a body of pure water. This is accomplished by disregarding the transmittance and downwelling radiance components (Chavez et al., 1996). Images where scattering is the primary cause of attenuation benefit from the DOS approach for correction (Moran et al., 1992). It is based on the concept that some of the image's pixels should be black (zero reflectance), and these pixels are referred to as "*Dark Objects*". Examples of objects with DN values

of zero or close to zero include dark areas cast by shadows and bodies of clear water. A first order atmospheric adjustment, such as the one achieved by the simple *DOS* approach (Vincent, 1972; Rowan et al., 1976), is preferable to no correction at all. The approach involves selecting a constant haze value (DN) for each spectral band by attributing the influence of the atmosphere to the smallest DN value in the histogram of the whole scene. The improved *DOS* (Chavez Jr, 1988) approach tends to rectify the haze in terms of atmospheric scattering and path radiance by using the power law of the relative scattering effect of the atmosphere.

In addition to capabilities for processing level 2 surface reflectance tiles, the Cos of Solar Zenith angle (*COST-DOS*) approach (Chavez et al., 1996) was automated within the developed web-*GIS* interface to process raw imageries directly. This *COST-DOS* approach is basically the improved *DOS* model with the incorporation of a Fourier series approximation for the solar zenith angle $\{\cos(\theta_z)\}$ term. Processing raw images with the automated *DOS* technique is important for achieving near real time processing capabilities, because the generation of level 2 surface reflectance products takes some time and also, in some cases, these tiles are not available (*e.g.*, for periods like in the years 2016-2018, where *Sentinel 2* level 2 tiles are unavailable for river Brahmaputra in Guwahati). The results obtained using automated *DOS* were validated with level 2 surface reflectance products, using commonly used supervised machine learning based classification algorithms *viz*., Random Forest Classifier and Support Vector Machines. Further, its ability to qualitatively estimate Normalized Difference Chlorophyll Index (*NDCI*) developed by Mishra and Mishra (2012), and replicate temporal trends was also accessed. The following section describes the aforementioned procedures comprehensively.

2.3 Methodology

A series of atmospheric correction (for Level 1 imageries), water body identification (for aquatic ecological parameter estimation), and water body removal (for terrestrial ecological parameter estimation) algorithms have been incorporated into the application interface to generate maps for aquatic and terrestrial ecological parameters. Figure 2.1 depicts the process flowchart in detail. This study was carried out entirely with opensource *GEE* (for processing raw satellite images) and *Python 3.8* (for analysis). More details on these are presented in Appendix A.

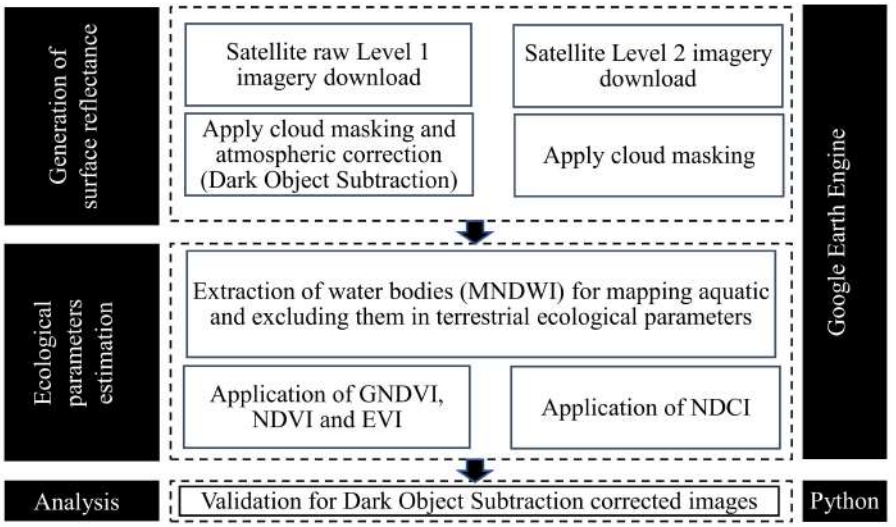

Figure 2.1: Methodology flowchart

2.3.1 DOS model {from Chavez et al. (1996)}

The following equation may be used as a generic representation of the DN values captured by imaging systems:

$$DN_i\,(X,Y) = G_i \times L_\lambda\{(X,Y)\} + O_i \tag{2.1}$$

$DN_i\,(X,Y)$ = pixel (X,Y) output DN in the band i
G_i = band i gain factor
$L_\lambda\{(X,Y)\}$ = pixel (X,Y) radiance in the band i
O_i = band i offset

Rearranging Equation 2.1, the following equation for radiance $L_\lambda\,(X,Y)$ is obtained:

$$L_\lambda\,(X,Y) = \frac{DN_i\,(X,Y) - O_i}{G_i} \tag{2.2}$$

To convert these radiances to surface reflectance (ρ), the general model as per Moran et al. (1992) is given as:

$$\rho_i(X,Y) = \frac{\pi \times \{L_\lambda(X,Y) - H_i\}}{\tau_{vi} \times \{E_o \times \cos(\theta_z) \times \tau_{zi} + E_{down}\}} \tag{2.3}$$

$\rho_i(X,Y)$ = Surface reflectance
H_i = Path radiance
τ_{vi} = Atmospheric transmittance from the ground surface to satellite
E_o = Solar spectral irradiance of the sun on a perpendicular surface outside the atmosphere $\left(Wm^{-2}sr^{-1}\mu m^{-1}\right)$
θ_z = Solar zenith angle
τ_{zi} = Atmospheric transmittance from sun to the ground surface
E_{down} = Surface downwelling spectral irradiance due to scattered solar flux in the atmosphere $\left(Wm^{-2}\mu m^{-1}\right)$

In this model, the improved *DOS* technique (Chavez et al., 1996) suggested the following values:

$\tau_{zi} = \cos(\theta_z)$
$\tau_{vi} = 1$ (for nadir view)
$E_{down} = 0$
H_i = dark object (value of darkest pixel in image)

2.3.2 Random Forest Classifier {from Breiman (2001)}

The Random Forest (*RF*) classifier uses a collection of tree classifiers from a supplied input vector. Each of the tree classifiers is produced from a random vector sampled separately from the input vector and which then searches, on a unit scale, for the most popular class. In this study, a random forest classifier was used, which builds a tree using a random feature or feature combination at each node. Bagging was used for each feature/feature combination, which is a technique for generating a training dataset by randomly drawing with replacement N samples, where N is the size of the original training set. Attribute selection in random forest is done using the Gini Index, which measures the relevance of an attribute with the class. The Gini index is defined as follows for a given training set T, where we randomly choose one instance (pixel) and assign it to a class C_i:

$$\sum\sum_{j\neq 1} = \{f(C_i,T)/|T|\}\{f(C_j,T)/|T|\} \tag{2.4}$$

where the probability that the example belongs to class C_i is denoted by $f(C_i, T)/|T|$.

When a tree is expanded to its maximum depth on fresh training data, a new set of features is learned. Parameters that must be set by the user while creating a random forest classifier are the number of trees to be produced and the number of characteristics to be utilized at each node. Selective feature searching is performed at each node to find the optimal branching. Thus, N trees make up the random forest classifier, with N being the user-defined maximum number of trees to be produced. Each instance from the datasets is then sent down each of the N trees to be classified. In such situation, the forest will choose the category that received the most votes (out of a possible N).

2.3.3 Support Vector Machines {from Vapnik (2013)}

Support Vector Machines (SVM) is based on statistical learning theory, whose goal is to locate the thresholds that will result in the most effective class separation. In a two class problem where the classes can be separated using linear features, SVM's choose a hyperplane that creates the most separation between them. The gap between the two classes is measured by adding together their respective nearest spots' distances to the hyperplane. Standard Quadratic Programming (QP) optimization methods may be used to the issue of maximising the margin. The margin is calculated based on the vectors or points that are closest to the hyperplane, which are referred to as "support vectors". If the two classes cannot be separated linearly, SVM's will look for the hyperplane that minimizes a quantity proportional to the amount of misclassification mistakes while maximizing the margin. SVM's can also be modified to work with nonlinear decision spaces. To lessen the computational burden of working with high-dimensional feature spaces, kernel functions are used.

2.3.4 Generation of surface reflectance

For the generation of analysis ready (surface reflectance) images from raw satellite imagery, a novel automated DOS correction technique was used in this study. When the user chooses Level 1 tiles for analysis, it is applied automatically. In the first step, it chooses the first image that falls within the time range the user specifies. When no images are found within the time range

specified by the user, an error message is displayed along with instructions to review the search parameters. The quality assessment band (QA) bitwise masking algorithm is used to remove the clouds. To obtain the darkest pixel value, each raster was converted to a dictionary datatype, which consists of key-value pairs. This was done using the *GEE* built in function "*ee.Dictionary*". In this study, the key corresponded to the pixel value and the value corresponded to the count of that pixel value. Then, a histogram was generated for the dictionary variable using the *GEE* built in function "*ee.Reducer.histogram*". Now, this histogram will automatically generate a key having 0 value and some count. To remove such values, the built in "*signum*" function was first used to identify the 0 values, and then the *GEE* built in *mask* function was used to remove those values. The first value in the dictionary variable remaining after removing the 0 value corresponds to the darkest pixels in the imagery.

2.3.5 App development

Within the "*GEE Apps*" platform, the modules developed for estimating the aforementioned terrestrial and aquatic ecological parameters have been combined into a Graphical User Interface (GUI) using Javascript. The app-based interface is much faster than the code editor interface, and the user no longer needs to be proficient in computer programming to manage data processing using *GEE*. Furthermore, new modules can be easily added to the interface. There are client-side and server-side components to each module. The app has a multi-stage interface, with the first asking the user to choose initial parameters like time frame and area of interest. Once the necessary inputs have been selected, the second stage will appear. It consists of microwave images for the selected period, as well as the surface reflectance tile and various buttons for selecting algorithms for quantitative $chl-a$ estimation (dummy algorithms, that can be replaced with accurate algorithms developed in the future). When the user selects an algorithm, the application advances to the next stage, which displays the final result. When the user clicks on a location in one of the generated maps, an interactive display shows the values of all the parameters. The app's user interface is depicted in Figure 2.2. The online app can be accessed at the following address:

https://riddickkakati.users.earthengine.app/view/aems

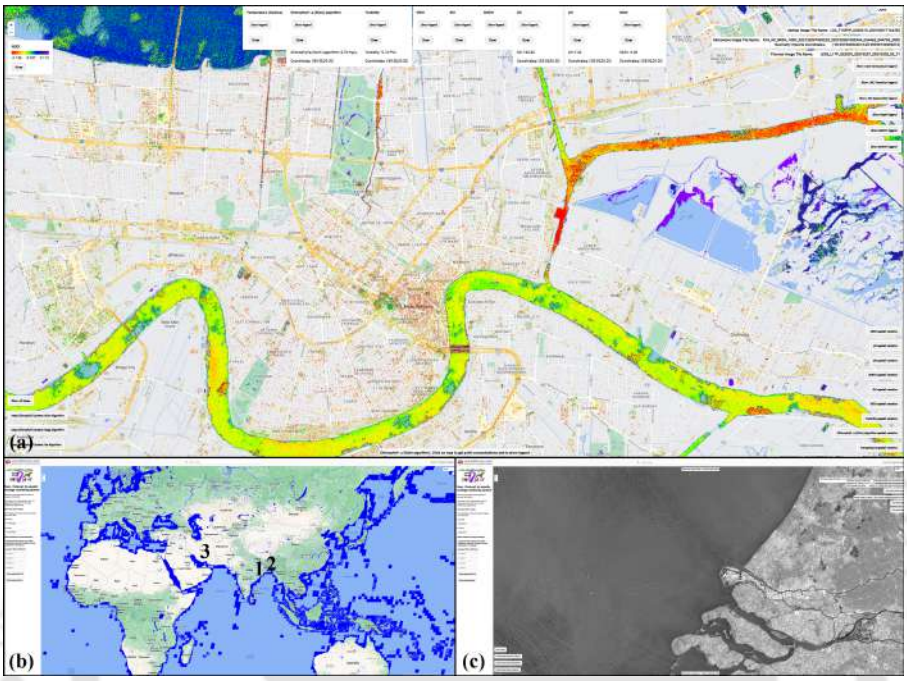

Figure 2.2: App developed and used in this study (a) *NDCI* map in New Orleans, United States of America (b) Graphical user interface showing study areas: (1) Uttar Pradesh, India (2) Assam, India (3) Ishfahan, Iran (c) Sentinel 1 processed microwave amplitude imagery (GEE dataset) of Rotterdam, Netherlands within the app interface

2.4 Results

One of the primary difficulties in enabling near real time monitoring capabilities is generating the surface reflectances (ρ) before any analysis is performed. Due to its unavailability during certain periods, the ability to process Level 1 raw satellite imagery has been incorporated into the developed web-*GIS* application, that has been described in the previous section. By implementing the *DOS* (Chavez et al., 1996) atmospheric correction procedure, the amount of path-radiance measured in the Level 1 imageries was reduced. Because of its effectiveness and simplicity, this method has been widely used in biophysical remote sensing studies (Teillet and Fedosejevs, 1995; Phinn et al., 2008; Hadjimitsis et al., 2010; Wicaksono and Hafizt, 2013; Wicaksono, 2017; Wicaksono and Hafizt, 2018). This procedure involves estimating the darkest pixel in each band of a satellite image and then subtracting that value from each pixel in that band. For this study, this process was automated within *GEE*

to eliminate the need for human intervention, resulting in processed data for further analysis and aiding in the generation of products in near real time. The *Sentinel 2A* Level 1 C dataset used for the analysis was downloaded from the data catalogue within the interface. Then this dataset was processed through the code editor using Equation 2.3 to obtain the surface reflectance values. Validation of the obtained approximate atmospherically corrected imageries was done by comparing it with the level 2 surface reflectance products using the *RF* and *SVM* classifiers described in the previous section. The following section discusses the results of the image classification.

2.4.1 DOS performance in image classification

The classification algorithms *viz.*, *RF* and *SVM* have been used to evaluate the efficiency of the automated *DOS* based *Sentinel 2* Level 1C imageries near the river Brahmaputra in Assam, India (Figure 2.3). These classifiers were trained to identify six classes *viz.*, agriculture, barren land, forest, river, urban and wetland. Training and testing data were selected using *Google Earth Pro*, where the true colour satellite imageries were used for generating the ground-truth. The details of the number of elements within each class used for ground-truths are listed in Table 2.1. The results of the analysis are shown in Figure 2.4. Comparison of the classification results are displayed in Figure 2.5. In terms of image classification, Figure 2.5 shows that the *Sentinel 2* Level 2 surface reflectance product performs similarly to the automated *DOS*-based approximate surface reflectance.

Table 2.1: Details of image classification

Classes	Type of pixel	Quantity
Agriculture (A)	Training	33
	Testing	15
Barren land (B)	Training	82
	Testing	19
Forest (F)	Training	42
	Testing	23
River (R)	Training	27
	Testing	16
Urban (U)	Training	119
	Testing	18
Wetland (W)	Training	93
	Testing	14

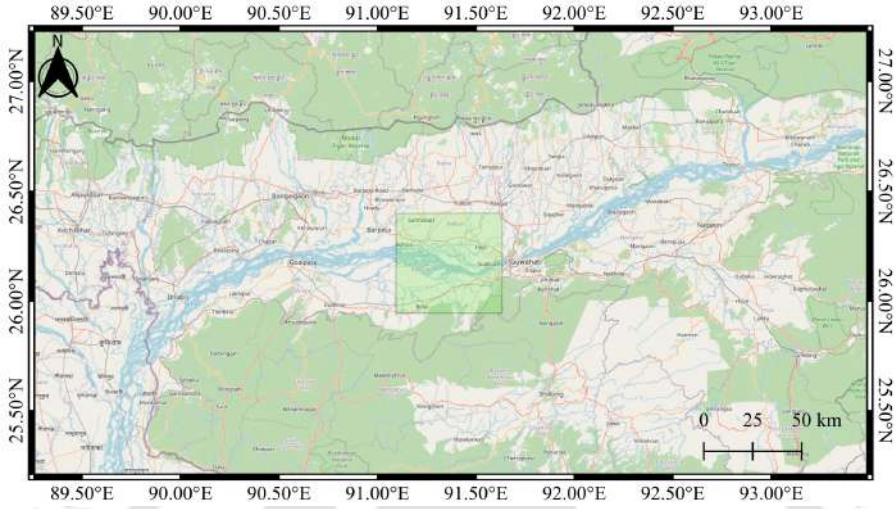

Figure 2.3: Study area for image classification and trend replication in Assam, India

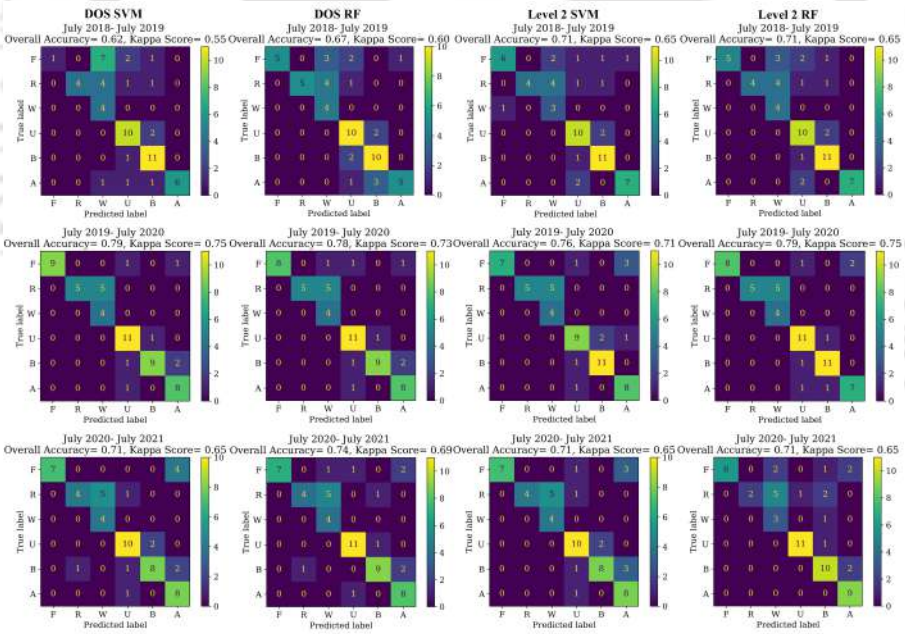

Figure 2.4: Confusion matrices for classification using automated DOS and level 2 surface reflectance

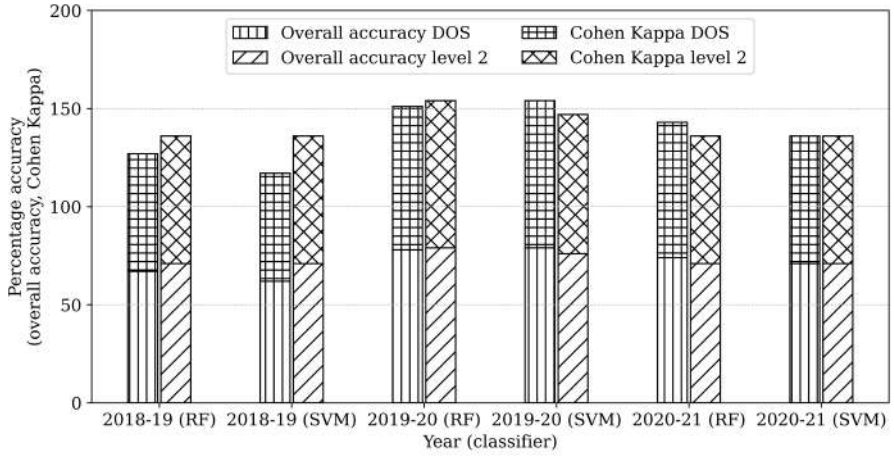

Figure 2.5: Accuracy assessment of automated DOS as compared to Level 2 imageries

2.4.2 DOS performance in temporal trend estimation

Similar to the comparison of performance in image classification described in the preceding section, the results generated by *LANDSAT 8* level 2 and *Sentinel 2 DOS* were evaluated in order to determine the applicability of *DOS* in trend analysis. This study was conducted on the river Brahmaputra in India (Figure 2.3). The temporal variation of ecological parameters *viz.*, Enhanced Vegetation Index (*EVI*), Normalized Difference Vegetation Index (*NDVI*), Greenness Normalized Difference Vegetation Index (*GNDVI*), and Normalized Difference Chlorophyll Index (*NDCI*) from 2016 to 2022 was investigated. Figure 2.6 displays the results obtained. *DOS* was able to roughly approximate the trend, but the range of values obtained was significantly different.

2.4.3 DOS performance in $NDCI$ estimation

The Ganga river of Uttar Pradesh, India has been chosen to evaluate the accuracy of $NDCI$ predictions using *DOS*, for a better comparison with field reported values in the literature. Absolute $chl-a$ values from $NDCI$ were calculated using equation 2.5 from United States Environmental Protection Agency (USEPA, 2008; Meena et al., 2021).

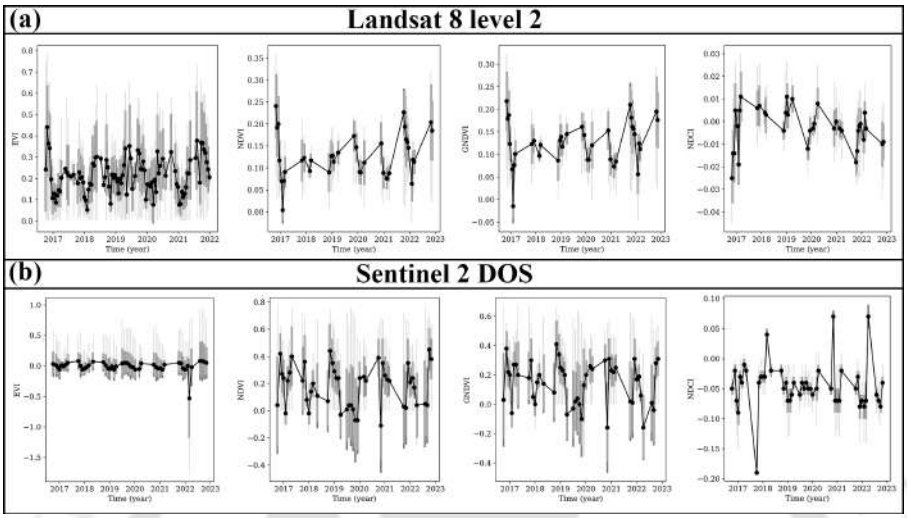

Figure 2.6: Comparison between LANDSAT 8 Level 2 and Sentinel 2 DOS in temporal trend replication

$$Chl - a(\mu g/L) = 194.325 \times NDCI^2 + 86.115 \times NDCI + 14.039 \qquad (2.5)$$

2.5 Discussion

For remote sensing applications, the scientific and policymaking communities are increasingly turning to *GEE* (Gorelick et al., 2017). The combination of a massive database of satellite products and cloud computing power makes it possible to perform massive analyses in a matter of seconds. Furthermore, its javascript-based app development platform allows advanced users to create *GUI*-based apps for repetitive tasks, as well as users who are unfamiliar with javascript coding. Because they are built on a web-based *GIS* platform, these resources can be accessed from anywhere with an internet connection and used by a wide range of interested parties and policymakers. Amid the worldwide outbreak of *COVID-19*, enhancing the availability of water quality information through web-based *GIS* has become a top priority for both governmental and corporate entities (Balla et al., 2022). Considering these requirements, an attempt has been made in this study to develop a near real time hydro-ecological monitoring web-*GIS* application.

Despite the fact that the app developed in this study is based on global indices, there have been very few validation studies of such indices under Indian conditions. Additionally, most indices have been validated in the literature with Level 2 surface reflectance products. The effectiveness of the automated *DOS* in image classification and the use of data from the previous literature to qualitatively estimate *NDCI* have been assessed in this section. To obtain surface reflectance images from the *Sentinel 2A* raw level 1C images, the automated *DOS* algorithm was executed within *GEE* code editor. The resulting images were extracted and classified using both *RF* and *SVM* algorithms. On the other hand, *Sentinel 2A* level 2 surface reflectance images were also extracted and classified using the same classifiers. The performance of the automated *DOS* algorithm was evaluated through classification accuracy using the confusion matrix method. Comparison of the classification results are displayed in Figure 2.5. In terms of image classification, Figure 2.5 shows that the *Sentinel 2* Level 2 surface reflectance product performs similarly to the automated *DOS*-based approximate surface reflectance. In terms of trend replication, the performance of *DOS* was satisfactory for qualitative estimation, however, there were significant differences when the values were compared quantitatively.

When comparing the field values reported by Prasad et al. (2020) and Bhattacharjee et al. (2022) for May 2017, October 2017, and May 2021 (Figure 2.7), the estimates from the automated *DOS* based *NDCI* are very close to the measured values. A disparity emerged between the predicted range by automated *DOS* and the field predicted values in these dates because of a lack of knowledge regarding the boundaries of the area under consideration in the literature, which led to the consideration of the entire image tile that fell within that area for analysis. Comparatively higher mismatches on other dates could be attributed to the time lag associated with field data collection and satellite passes.

2.6 Summary

The popularity of *GEE* for remote sensing applications has risen significantly owing to its vast satellite database and robust cloud computing capabilities. In this chapter, the development of a web-*GIS* platform to facilitate hydro-ecological monitoring in near real time has been discussed, which can process both level 1 raw, as well as level 2 surface reflectance satellite products. Further, the performance of the *DOS* algorithm, which was automated in this study, was evaluated in terms of efficiency in image classification, qualitative estimation,

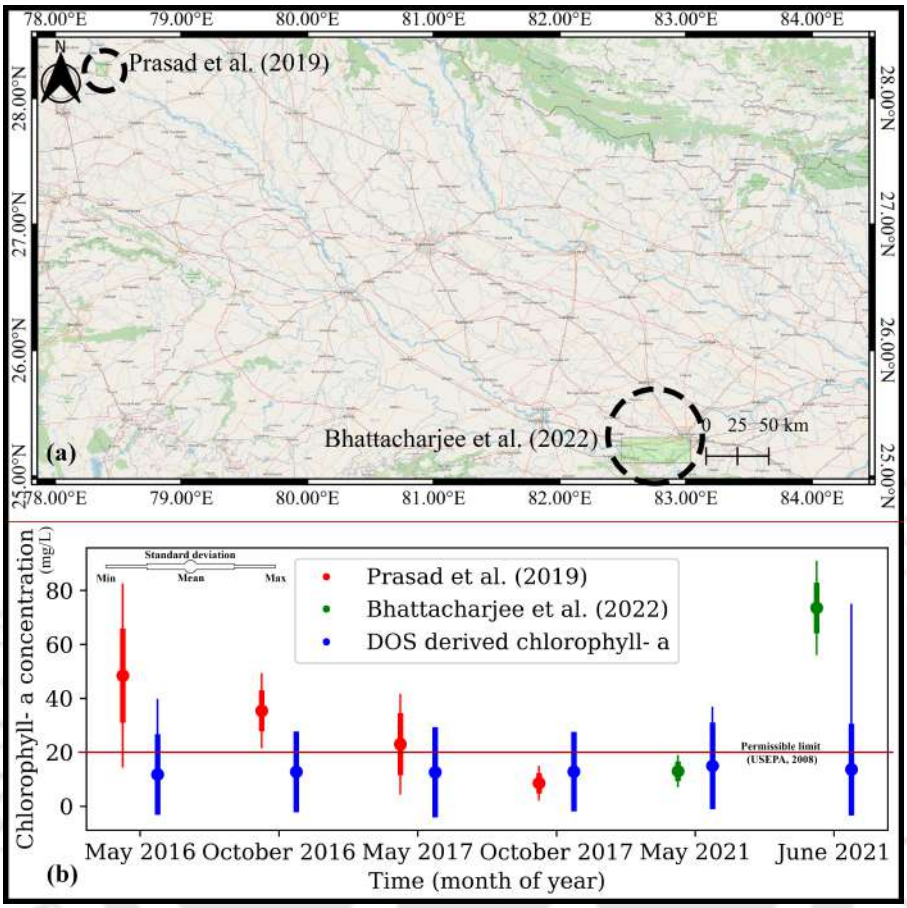

Figure 2.7: (a) Study areas for validation (b) Comparison of DOS based chl-a with field values reported in the literature for the river Ganga

and trend replication. The results indicated acceptable qualitative performance, but notable disparities in quantitative estimation. The app was further used to map nutrient exchange mechanisms in riparian vegetation zones of rivers using level 2 products, which is discussed in the next chapter.

3

Understanding hydro-ecological exchange mechanisms

This chapter discusses the nutrient exchange mechanisms between river and flood plains that sustains the river ecological habitat

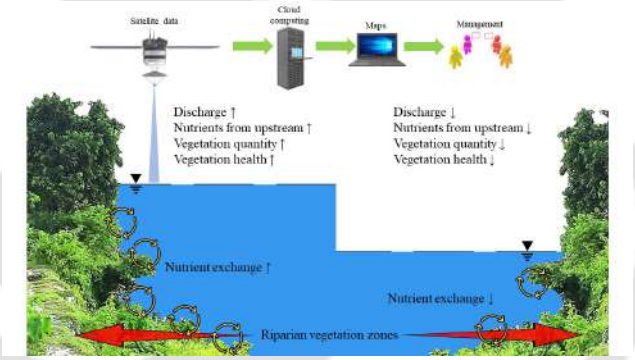

Contents

3.1 General

The web-*GIS* application developed in this study, that was described in the previous chapter has been further used to map nutrient exchange mechanisms in riparian vegetation zones along the rivers in Iran and India. These observed nutrient exchange mechanisms have been discussed in this chapter. The chapter begins with the section "Introduction", which presents a literature review of various water quality parameters that can be estimated with satellite remote sensing. The next section describes the methodology adopted. After that, the next section deals with the results obtained. It is followed by a discussion on it. The chapter ends with a summary of the results and their discussions.

3.2 Introduction

Over the course of human history, rivers have been indispensable to our survival as vital components of the water cycle and as pathways for the transport of water, sediments and nutrients. Even the earliest of civilizations (such as the Egyptians on the Nile, the Mesopotamians on the Tigris/Euphrates rivers, the ancient Chinese on the Yellow River, and the ancient Indians on the Indus) got their starts on riverbanks. The ecological habitat of many rivers has been drastically altered as a result of human intervention, such as the river Ganga, once celebrated for its cleanliness but now ranked as the world's fifth most polluted river (Flynn, 2016). The catastrophic state of declining water quality in the river, and minimal riparian vegetation cover is a direct result of human actions on the river that are not being closely monitored.

Since it would be costly and inefficient to conduct frequent field surveys to monitor these activities, remote sensing-based techniques integrated into web-*GIS* platforms can act like a rapid and cost-effective method for monitoring rivers in near real time. There is extensive literature on the estimation of water quality parameters like chlorophyll-a ($chl-a$) and turbidity in rivers, which can be used to facilitate satellite-based water quality monitoring. $Chl-a$ is the most significant indicator of trophic status because it links nutrient levels, particularly phosphorus, to algal production (Gholizadeh et al., 2016). The first attempt to determine its concentration in rivers through the use of satellite remote sensing was made by Kuhn et al. (2019). Using *Sentinel* and *LANDSAT* images, it has been studied in Indian rivers by Prasad et al. (2020),

and Bhattacharjee et al. (2022). Meena et al. (2021) utilised *NDCI* as one of the parameters to assess water quality in Indian rivers. Remote sensing has also been used to estimate parameters like dissolved oxygen (*DO*) and *pH* (Bejarano et al., 2020) in the Ganga river of India (Das et al., 2022). Water temperature is another vital ecological indicator that can be estimated with the help of thermal spectral bands of *LANDSAT* (Vanhellemont, 2020). In this section, riparian and non-riparian vegetation zones along the rivers Zayandeh-Rood and Brahmaputra in Iran and India, respectively were analysed using the app developed in Chapter 2 with a combination of water quality and vegetation indices to determine spatio-temporal variation in derived ecological parameters.

3.3 Methodology

Identification of water bodies is a prerequisite for creating maps of aquatic ecological parameters. Normalized Difference Water Index ($NDWI$) and Modified Normalized Difference Water Index ($MNDWI$) can be used for this purpose. $MNDWI$ was found to be more reliable than $NDWI$ in identifying water bodies (Szabo et al., 2016). A combination of $MNDWI$, $NDVI$ and EVI was used in this study for a more accurate water body identification. Land pixels are identified and masked out of the images if the $NDVI$ is greater than 0.1 and the $MNDWI$ is greater than 0.1, or if the $MNDWI$ is greater than $NDVI$. In the case of Level 2 imageries, it is applied directly, and for Level 1 imageries, the result of *DOS* is used. Following water body masking, the resulting images are used to derive $NDCI$. Provisions have also been made for the future incorporation of algorithms capable of quantitative estimation of *chl-a* on a global scale. Within the interface of the app, algorithms from Prasad et al. (2020) have been used for quantitative analysis using *LANDSAT* imageries, and equations from Ha et al. (2017), Page et al. (2018), and Kuhn et al. (2019) have been used for *Sentinel* images. However, these algorithms can currently only be used in the regions for which they were developed. Table 3.1 shows the various bands available in the *LANDSAT 8* and *Sentinel 2* satellites, whereas Table 3.2 shows the various algorithms that have been used in the application.

To generate terrestrial ecological parameter maps, water bodies must be excluded. The water bodies were removed from the analysis using the same algorithm used to identify them in the estimation of aquatic ecological parameters. The resulting images are used to obtain $NDVI$, EVI, and $GNDVI$. A summary of all the previously mentioned indices and empirical formulae along

with their references are presented in Table 3.2. The methodology adopted is presented in Figure 3.1.

Table 3.1: Bands of Sentinel 2 and Landsat 8 satellites

Band name	Landsat 8		Sentinel 2	
	Wave-length range (μm)	Central wave-length (μm)	Wave-length range (nm)	Central wave-length (nm)
Coastal Aerosol	0.43 -0.45	0.44	443 -453	443
Blue	0.45 -0.51	0.48	496 -511	490
Green	0.53 -0.59	0.56	526 -546	560
Red	0.64 -0.67	0.66	650 -680	665
NIR	0.85 -0.88	0.86	832 -918	865
SWIR 1	1.57 -1.65	1.61	1610 -1700	1650
SWIR 2	2.11 -2.29	2.20	2025 -2125	2100
Panchromatic	0.50 -0.68	0.59	-	-
Cirrus	1.36 -1.38	1.37	1360 -1390	1375
TIRS 1	10.60 -11.19	10.80	-	-
TIRS 2	11.50 -12.51	12.00	-	-
Red Edge 1	-	-	698 -712	705
Red Edge 2	-	-	731 -745	740
Red Edge 3	-	-	773 -793	783
Narrow NIR	-	-	856 -879	865
Water Vapor	-	-	945 -960	945

3.4 Results

The results of validation shown in Chapter 2 indicate that on using automated *DOS*, the app is only suitable for qualitative analysis. In quantitative analyses, it performed less effectively than Level 2 surface reflectance products in predicting values. Therefore, the Level 2 surface reflectance products have been used for all subsequent analyses. Since *Sentinel* Level 2 products were not available for the river Brahmaputra from 2016 to 2018, *LANDSAT 8* images were used entirely for this investigation. The performance of *LANDSAT*-based *DOS* imageries was not evaluated in this study due to their lower spatial resolution when compared to *Sentinel* imageries. Figure 3.2 displays the study areas that were considered for this analysis.

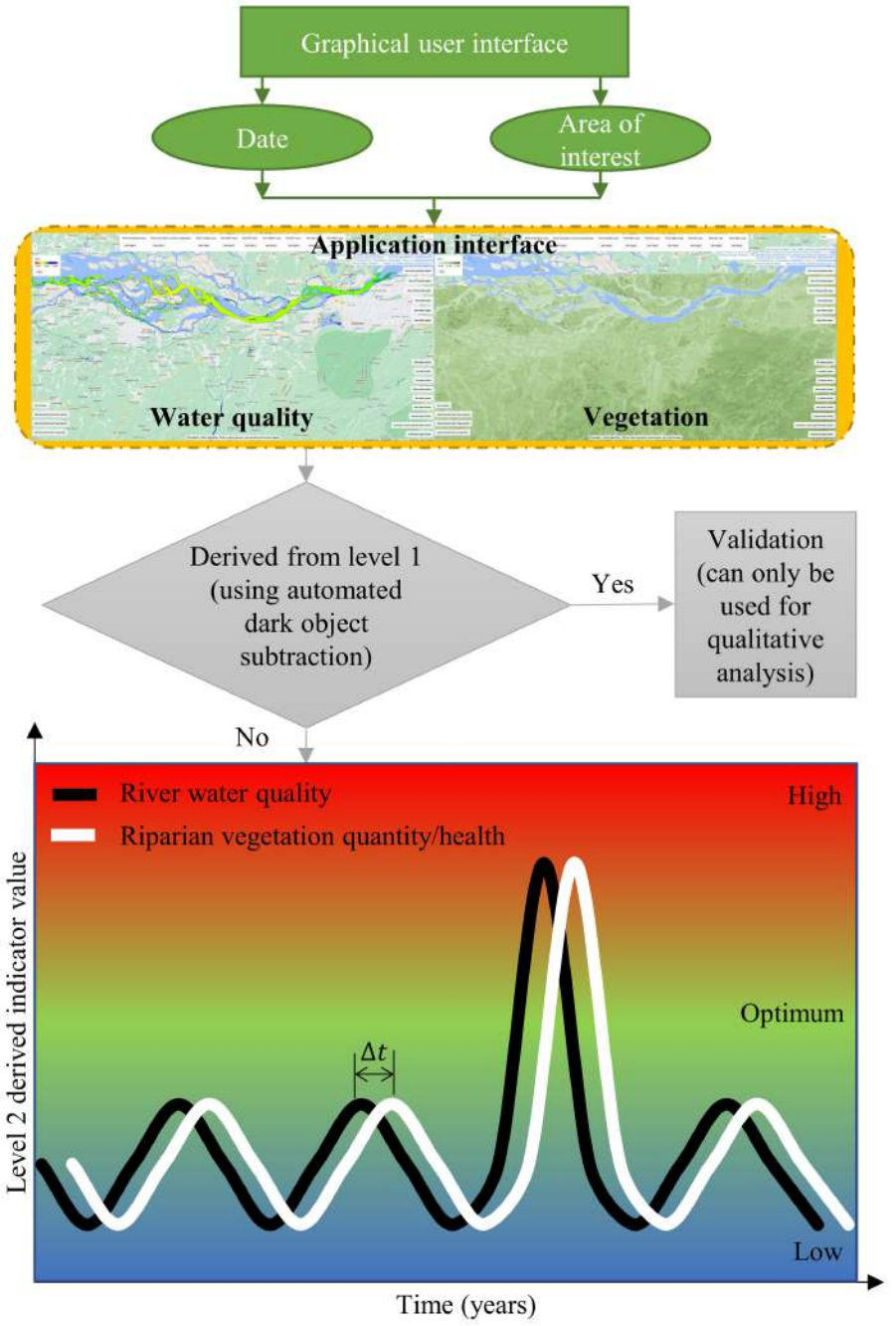

Figure 3.1: Methodology adopted for understanding nutrient exchange mechanisms betweeen river and its riparian vegetation zones

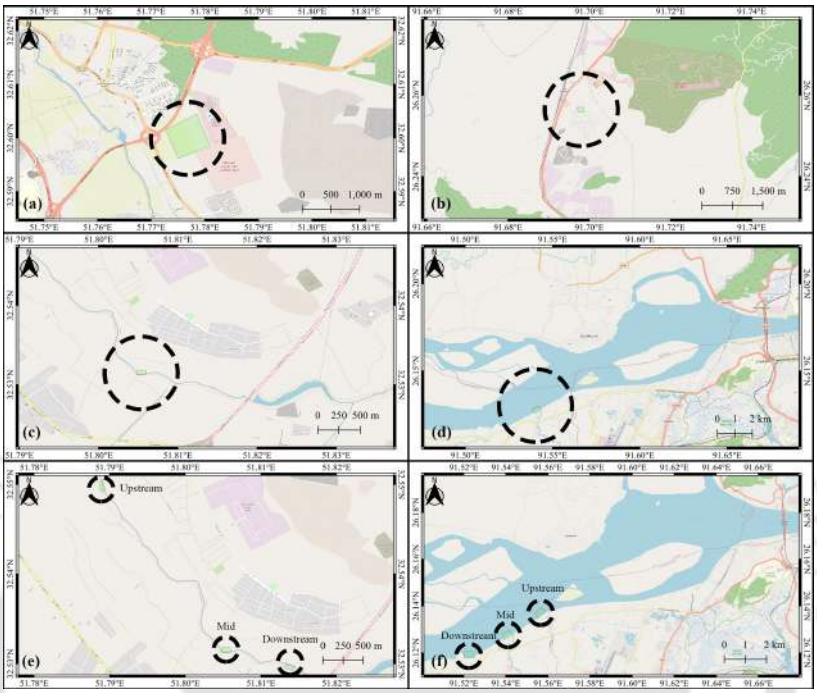

Figure 3.2: Study areas considered. (a) non-riparian zone near Ishfahan east ring expressway, Iran (b) non-riparian zone near Guwahati, India (c) riparian zone on the banks of Zayandeh-Rood river (d) riparian zone on the banks of Brahmaputra river (e,f) additional riparaian zones considered in the upstream and downstream on the banks of rivers Zayandeh-Rood and Brahmaputra respectively for spatial analysis.

3.4.1 Temporal variation of ecological parameters

In this section, the app developed in this study is used to perform a temporal change detection analysis to better understand the interactions of riparian vegetation zones with river water and their impact on water quality. In this case, four study areas were assessed, *viz.*, two non-riparian zones and two riparian zones (Figure 3.2) located in a humid climate zone (Assam, India) and arid climate zone (Isfahan, Iran), respectively. The river Ganga was excluded from this analysis due to its extremely sparse riparian vegetation. In the case of riparian zones, the analysis was further carried out for two more locations (upstream and downstream) to gain a better understanding of the processes on a spatial domain.

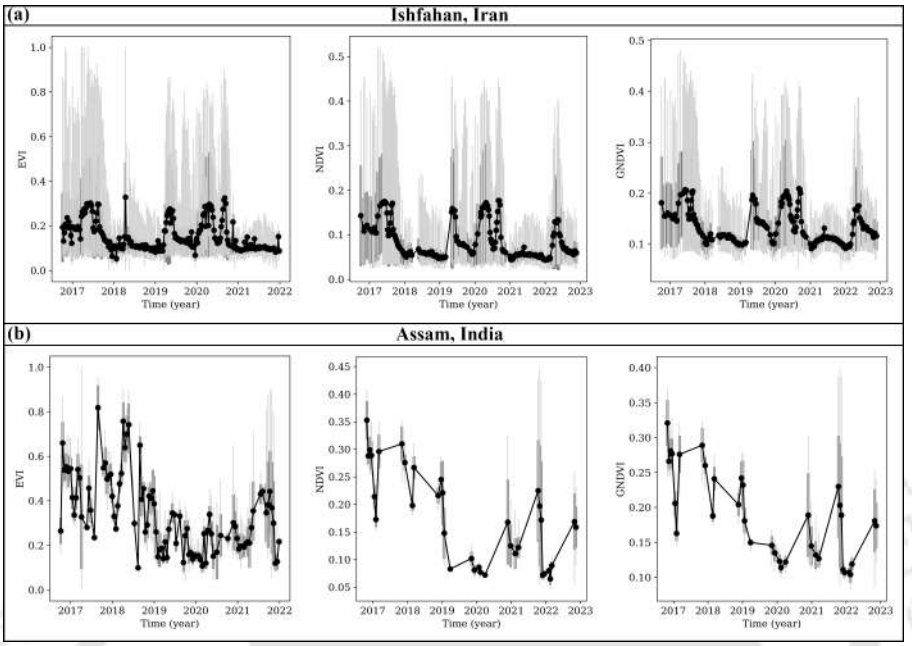

Figure 3.3: Temporal variation of ecological parameters for non-riparian zones: mean (black), standard deviation (dark grey); minimum, maximum (light grey)

3.4.1.1 Variation in non-riparian zones

In the case of non-riparian zones (Figure 3.2), the temporal variation of ecological parameters *viz.*, EVI, $NDVI$, and $GNDVI$ from 2016 to 2022 was investigated. Since the interpretations of EVI and $NDVI$ are similar, the *LANDSAT* EVI database was used directly, and the $NDVI$ was calculated from the *LANDSAT* Level 2 surface reflectance product, in order to make a comparison between the *USGS* EVI dataset and the application processed dataset. It was found that the app was able to replicate the trend exactly; however, there are fewer data points when compared to the EVI dataset because the app uses a cloud cover threshold of 20 percent.

A sinusoidic pattern is captured for site in Iran due to arid climatic conditions and relatively higher cloud-free periods; however, there are random peaks and troughs (Figure 3.3). The sinusoidal pattern is somewhat roughly captured for the site in India, which has a humid climate and relatively higher cloudy periods; however, there are random peaks and troughs in this case too (Figure 3.3).

3.4.1.2 Variation in riparian zones

A similar analysis was performed with the addition of $NDCI$ for the case of riparian zones (Figure 3.2), and the sinusoid pattern as observed in the previous section for the site in Iran was observed here too (Figure 3.4). These trends are also roughly replicated for the site in India (Figure 3.4), which has a humid environment and considerably higher cloudy periods. However, in addition to the sinusoidal pattern, a cyclic pattern has also been observed in this case. This observed pattern resembles the average annual fluctuation in river discharge for the river Zayandeh-Rood with a slight lag (Figure 3.4). It was replicated even in terrestrial datasets *viz.*, $NDVI$, $GNDVI$ and EVI, where water was excluded.

The annual trend of discharge was extracted for the river station Qale-Shahrokh from (Zolfagharpour et al., 2022). The average annual trends for $NDVI$, $GNDVI$, EVI and $NDCI$ were also calculated. These were then normalized with average values and plotted in Figure 3.4. Furthermore, it can be seen that $NDVI$, $GNDVI$, and EVI are in the same phase, with $NDCI$ and discharge approximately lagging by $\pi/2$ on the temporal domain (Figure 3.4).

Computed $NDCI$ for the river Zayandeh-Rood vary from 0 to 0.04, corresponding to $chl-a$ ranging from 16 to 20 mg/L. Similarly, the river Brahmaputra has a range of -0.03 to 0.02, corresponding to 13 to 18 mg/L. Since these levels are much below than the allowable limit for eutrophication (USEPA, 2008), no such occurrence was observed throughout the study period.

3.4.2 Temporal gradient analysis of ecological parameters

Similar to previous analyses, a temporal gradient analysis was performed on riparian vegetation and non-riparian zones in Iran and India to identify episodic events. In addition, for $NDCI$, a temporal change detection and gradient analysis were performed on the Ganga. The gradient analysis was done by subtracting the mean values between two consecutive dates for the whole time series data set obtained from 2016 to 2022 for the ecological parameters specified in previous sections. As in previous cases, $LANDSAT$ EVI product was utilised directly for EVI, and other indices were derived using $LANDSAT$ Level 2 surface reflectance.

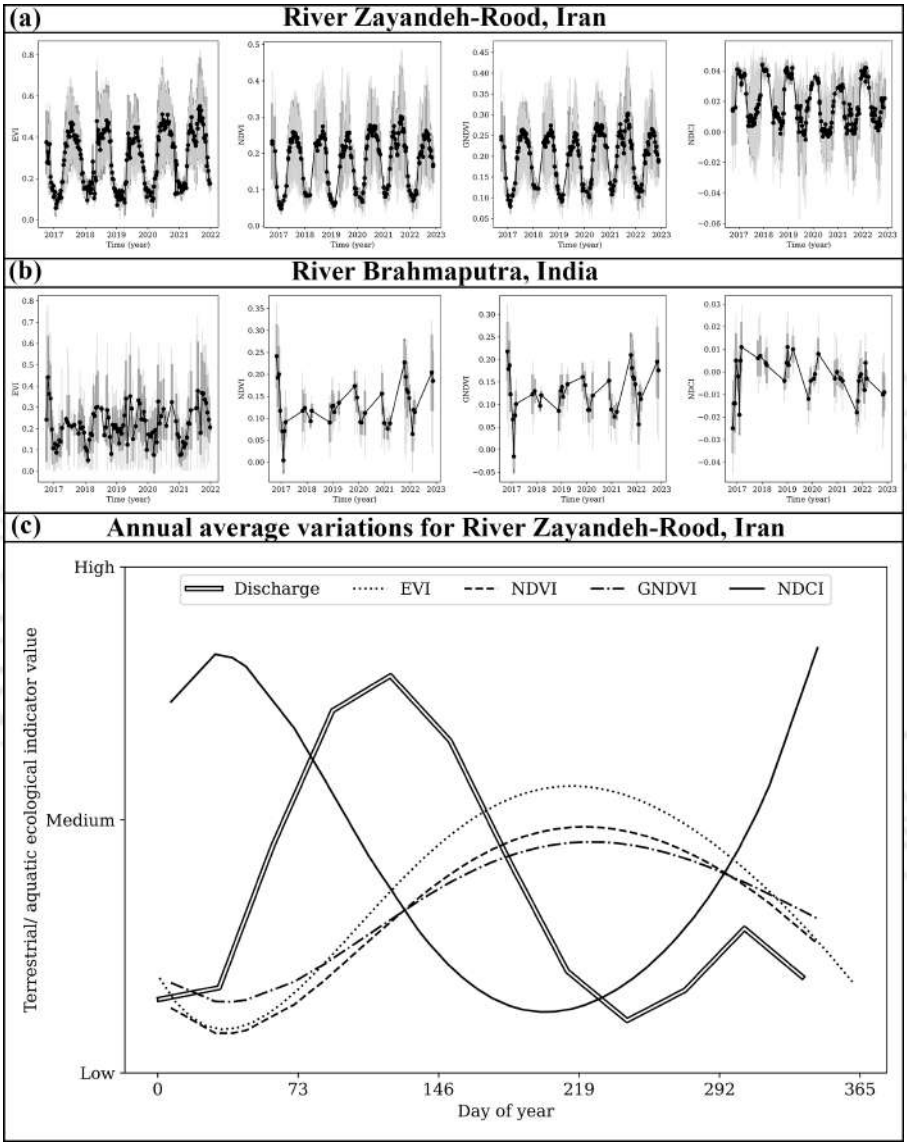

Figure 3.4: (a,b): Temporal variation of ecological parameters for riparian zones: mean (black), standard deviation (dark grey); minimum, maximum (light grey) (c): normalized smoothened annual average temporal variations of discharge, EVI, $NDVI$, $GNDVI$, and $NDCI$ for River Zayandeh-Rood, Iran

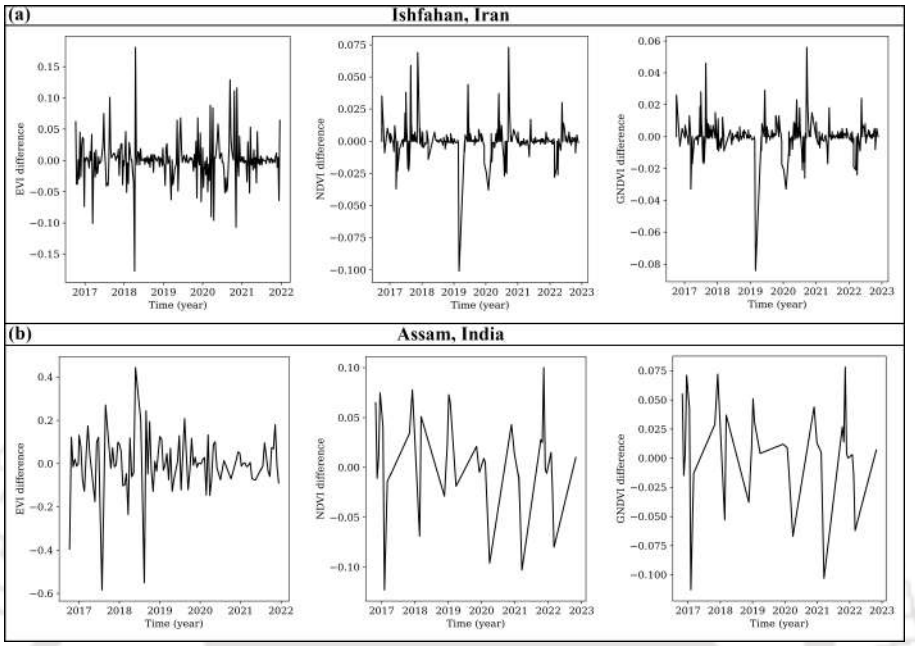

Figure 3.5: Temporal gradient analysis for non-riparian zones

3.4.2.1 Temporal variation in non-riparian zones

Due to the lack of riparian vegetation zones along the Ganga, vegetation parameters could not be calculated. Hence, assessments for the Ganga River have been disregarded for the non-riparian zones. Figure 3.5 shows the results of temporal gradient analysis in non-riparian zones of Ishfahan and Assam. Similar to previous cases, there is no distinct cyclic pattern and there are random peaks and troughs. Moreover, no episodic events were identified throughout the course of the study.

3.4.2.2 Temporal variation in riparian zones

Except for the river Ganga, where vegetation indices could not be calculated due to lack of vegetation, all of the ecological parameters evaluated in this study are taken into account. As can be seen in Figure 3.6, the cyclic pattern was also present in this case. Nevertheless, there was no evidence of episodic events throughout the time frame of this investigation. It can be seen that the

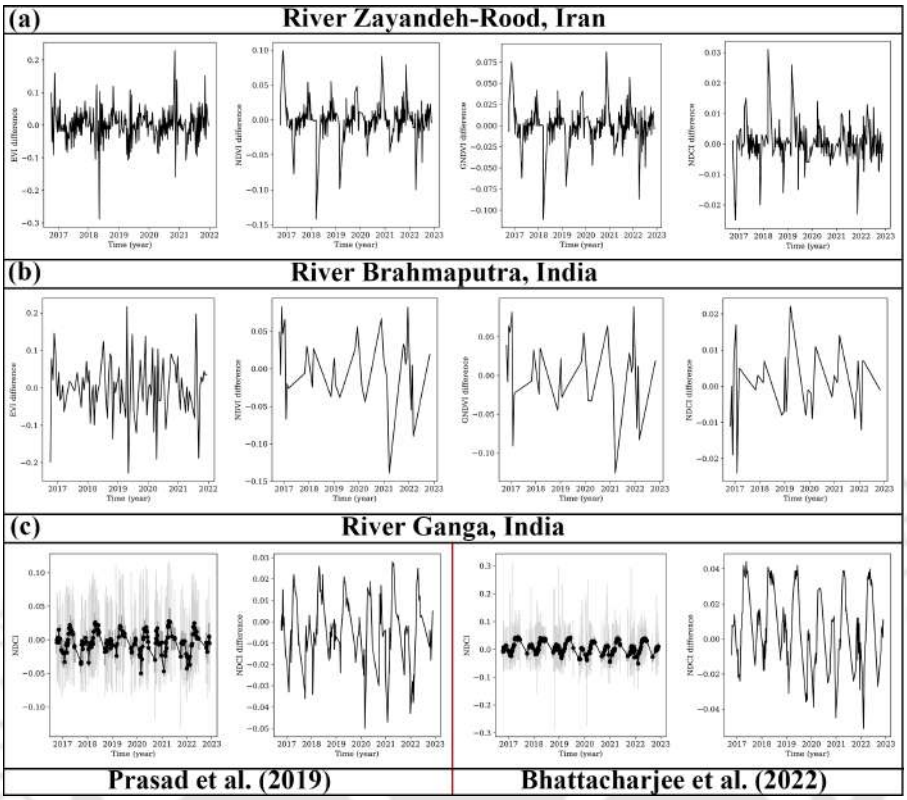

Figure 3.6: Temporal gradient analysis for riparian vegetation zones

significant decline in river water quality for the river Ganga, as reported by Prasad et al. (2020) and Bhattacharjee et al. (2022), is part of a periodic cycle, which has been happening for a very long time before the time period addressed in this study. As compared to the Brahmaputra and the Zayandeh-Rood, the $NDCI$ variations seen on the Ganga are much higher.

3.4.3 Spatial variation of NDCI in riparian zones

A study of the temporal variation of $NDCI$ was also conducted at upstream and downstream locations for both arid (Ishafan, Iran) and humid (Assam, India) climatic conditions in order to rule out the possibility of localised influences on the sites considered so far. These locations were chosen so that there are no connecting channels that could increase discharge or nutrient load. These areas are depicted in Figure 3.2. Figure 3.7 shows that the sinusoidal discharge

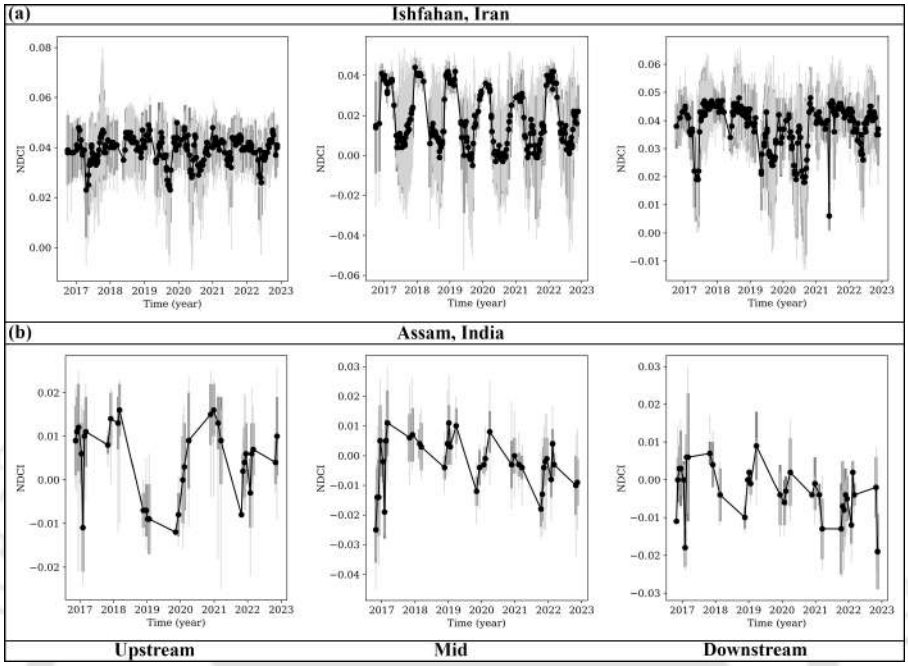

Figure 3.7: Temporal variation of ecological parameters along with minimum, mean, maximum, and standard deviation for upstream and downstream locations

pattern observed in the preceding sections is present in all $NDCI$ cases. In all of these cases, the pattern was clearly replicated for arid climatic conditions due to more cloud free periods. The range of $NDCI$ values in Figure 3.7 also shows that there is no nutrient transport from upstream to downstream, suggesting that the river's carrying capacity has a limit beyond which excess nutrients are released into flood plains. On the contrary, if the nutrient concentration in the river drops below a certain threshold, the river will absorb nutrients from the floodplains.

3.5 Discussion

In this study, a web-*GIS* application for multiparameter ecological monitoring was developed and used to investigate nutrient exchange mechanisms between riparian vegetation and non-riparian zones. A high correlation between vegetation quantity ($NDVI$) and vegetation health ($GNDVI$) has been observed for both non-riparian and riparian vegetation (Figure 3.8), indicating that if vegetation quantity increases, so does vegetation health. This is a result of an

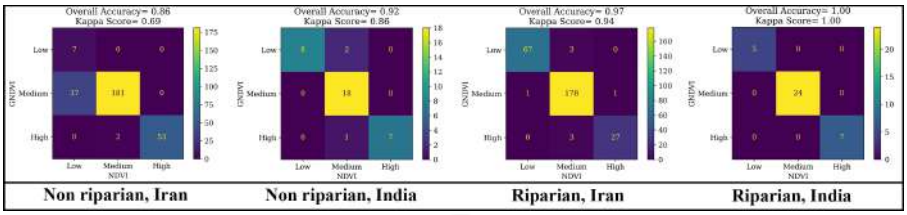

Figure 3.8: Comparison between $GNDVI$ and $NDVI$

increase in the system's nutrients, which play a significant role in regulating the quantity and quality of vegetation. When the temporal variation of EVI, $NDVI$, and $GNDVI$ for non-riparian zones was plotted, no cyclic pattern was observed, but it was observed for riparian vegetation zones.

3.5.1 Nutrient exchange mechanism for riparian zones

A river carries sediments along with its discharge, and complex energy dissipation mechanisms along its course cause continuous erosion and deposition (Goswami, 1985; Chang, 1998; Karmaker and Dutta, 2011; Ashmore, 2013; Karmaker and Dutta, 2013; Picco et al., 2013; Karmaker and Dutta, 2016; Chembolu and Dutta, 2018; Pradhan et al., 2019, 2021; Nandi et al., 2022). According to the sediment balance theory (Lane, 1955), sediment discharge is directly proportional to river discharge. These sediments are composed of organic and inorganic components, with the majority of the organic components serving as nutrients for the aquatic ecosystem. There is also a continuous lateral exchange of nutrients from the flood-plain to the river, as reported by Golombek et al. (2021). As $NDCI$ increases as a result of an increase in river water and sediment discharge, a subsequent increase in the $NDVI$ and $GNDVI$ indices is observed as a result of the lateral nutrient exchange mechanism. Similar findings have been reported by Li et al. (2023) in terms of the effect of land use on water quality. There is also a time lag due to the vegetation's response to nutrient changes.

The results showed that the riparian vegetation zones exhibited a sinusoidal cyclic pattern identical to the river discharge for both terrestrial and aquatic ecological parameters, with a lag between them. The $NDCI$ was also found to fluctuate much more in the Ganga than in the Brahmaputra or the Zayandeh-Rood. This implies that a constant nutrient supply-exchange mechanism between upstream and the floodplains sustains the rivers' ecological habitat, resulting in a healthy ecosystem. The larger $NDCI$ fluctuations in the Ganga

may be linked to the lack of riparian vegetation zones in its floodplains, which facilitate these nutrient exchange processes that serve to sustain $NDCI$ levels. Disrupting the rivers' flow also disrupts this nutrient supply, which has consequences for the environment farther downstream. Certain courses of rivers often experience stagnation and flow disruptions as a result of human involvement, either via river training or as a natural response to human activity. As the temporal fluctuation pattern of indices like $NDVI$ and $GNDVI$ follows the discharge pattern, it can be concluded that river discharge is a major driver of riparian vegetation dynamics.

3.5.2 Riparian vegetation as a river water quality indicator

As demonstrated in the previous sections, an increase in nutrient content in the river leads to an increase in vegetation cover as well as its health. Yet, high nutrient concentration causes the eutrophication of ecosystems (Khan and Mohammad, 2014). The Ganga's water quality has been widely reported to have declined dramatically in recent years (Prasad et al., 2020; Bhattacharjee et al., 2022). According to this study, riparian vegetation is severely diminished or absent along contaminated river lengths. In the case of the Brahmaputra, the range of values represented by the indices $NDCI$, $NDVI$, and $GNDVI$ indicates that ecological health has been preserved owing to the continual interactions between riparian vegetation and the river. As a result, the presence of riparian vegetation acts as a proxy indication of river water quality in terms of its trophic status. The absence of riparian vegetation on the banks of the Ganga also hinders its capacity to cleanse itself from the anthropogenic stressors that it experiences as it flows through Uttar Pradesh, the state with the largest population in India at about 200 million (Susuman et al., 2016). However, the river Brahmaputra, which flows through approximately six times lesser populous states in India, is far less impacted due to the existence of riparian vegetation zones and lower human stressors. Hence, riparian vegetation plantations along the banks of the river Ganga may serve as an efficient and long-term solution to the issue of its declining water quality.

3.6 Summary

This chapter discusses on the nutrient exchange mechanisms, that were identified between a river and its surrounding riparian vegetation zones using the web-

GIS application developed for this study. The findings revealed a strong relationship between vegetation quantity and health in both riparian and non-riparian zones, demonstrating the influence of nutrient input on the health of the vegetation system. It was found that river discharge was a key factor in riparian vegetation dynamics, with the rivers' natural habitat being sustained by a consistent nutrient supply-exchange mechanism. Since its absence interferes with the river's ability to purify itself, riparian vegetation can therefore serve as a proxy indication of the quality of river water. The absence of riparian vegetation and anthropogenic stresses have had a significant negative influence on the water quality of the Ganga. Therefore, the problem of decreasing water quality of the river Ganga may be effectively and permanently resolved through riparian vegetation plantations along its banks. In order to gain a comprehensive understanding of the observed nutrient exchange mechanisms, a three-dimensional hydrodynamic model was set up and is described in the following chapter.

Table 3.2: Various algorithms used in the application

Indices/Empirical formula	Reference
$MNDWI = \frac{\rho_{green} - \rho_{SWIR}}{\rho_{green} + \rho_{SWIR}}$	Xu (2006)
$NDCI = \frac{\rho_{rededge1} - \rho_{red}}{\rho_{rededge1} + \rho_{red}}$	Mishra and Mishra (2012)
$Chl - a(mg/L) = -426.431 + 439.787 \times \left(\frac{\rho_{green}}{\rho_{red}}\right)$ $Chl - a(mg/L) = 8.939 \times 10^{-5} \times e^{\left(16.819 \times \frac{\rho_{blue}}{\rho_{red}}\right)}$ $Chl - a(mg/L) = -297.069 \times \ln\left(\frac{\rho_{red}}{\rho_{blue}}\right) + 116.453$ $Chl - a(mg/L) = 1268.37 \times \left(\frac{\rho_{red}}{\rho_{blue}^{13.301}}\right)$	Prasad et al. (2020)
$Chl - a(mg/L) = 0.80 \times e^{\left(0.35 \times \frac{\rho_{green}}{\rho_{red}}\right)}$	Ha et al. (2017)

$Chl-a(mg/L) = 14.039 + 86.115 \times \left(\frac{\rho_{rededge1}-\rho_{red}}{\rho_{rededge1}+\rho_{red}}\right) + 194.325 \times \left(\frac{\rho_{rededge1}-\rho_{red}}{\rho_{rededge1}+\rho_{red}}\right)^2$	Page et al. (2018)
$\log_{10}\{Chl-a(mg/L)\} = 0.241 - 2.055 \times \{\log_{10}\left(\frac{\rho_{blue}}{\rho_{green}}\right)\} + 1.178 \times \{\log_{10}\left(\frac{\rho_{blue}}{\rho_{green}}\right)\}^2$ $-0.554 \times \{\log_{10}\left(\frac{\rho_{blue}}{\rho_{green}}\right)\}^3 + 0.470 \times \{\log_{10}\left(\frac{\rho_{blue}}{\rho_{green}}\right)\}^4$	Kuhn et al. (2019)
$NDVI = \frac{\rho_{NIR}-\rho_{red}}{\rho_{NIR}+\rho_{red}}$	Kriegler et al. (1969)
$EVI = G \times \frac{\rho_{NIR}-\rho_{red}}{\rho_{NIR}+C_1\times\rho_{red}+C_2\times\rho_{blue}+L}$ G = Gain Factor L = Canopy background adjustment C_1, C_2 = Coefficients for aerosol resistance	Huete et al. (1999)
$GNDVI = \frac{\rho_{NIR}-\rho_{green}}{\rho_{NIR}+\rho_{green}}$	Gitelson et al. (1996)

4

Modelling hydro-ecological interactions

This chapter focusses on modelling the momentum exchanges between river and its flood plain that drives the nutrient exchange mechanisms

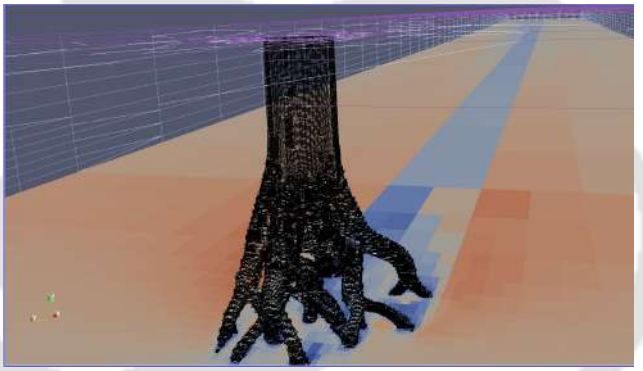

Contents

4.1 General

This chapter discusses the physics that govern the nutrient exchange mechanisms that were observed in the previous chapter, using hydrodynamic modelling. The first section provides a literature review of the various river training works and river bank erosion protection measures. It is followed by the section on the methodology adopted. Then follows the section on the results obtained. After that, the next section presents a discussion of the results obtained. At the end, there is a summary, which gives an overview of the whole chapter.

4.2 Introduction

Alluvial rivers are usually meandering and braided. Within a short period of time, these rivers undergo significant and dynamic morphological changes (Goswami, 1985; Chang, 1998; Karmaker and Dutta, 2011; Ashmore, 2013; Karmaker and Dutta, 2013; Picco et al., 2013; Karmaker and Dutta, 2016; Chembolu and Dutta, 2018; Pradhan et al., 2019, 2021; Nandi et al., 2022). River training works in hydraulic engineering help to redirect main flow, maintain desired water depth, protect riverbanks from erosion, create stable pools for aquatic habitat, and trap suspended sediment in backwater zones (Mayerle et al., 1995; Duan et al., 2009; Jennifer et al., 2011; Gu et al., 2016). They are divided into two categories: permeable and impermeable. However, its type is determined by the construction and river geomorphologic principles, layout, dimensions, the importance of the protected area, and the rivers' feedback in terms of hydraulic, morphologic and environmental response (Sarker et al., 2011; Gilja et al., 2019; Oberhagemann et al., 2020; Markovic Brankovic et al., 2021). Their deployment is based on field experience and limited research (Aamir and Sharma, 2015; Karmaker and Dutta, 2016). Numerous reported cases of the inadequacy of permeable river training works in the form of porcupine screens (Figure 4.1) in the Brahmaputra river of India have resulted in massive losses (Principal Accountant General, Indian Audit and Accounts Department, 2011). Similarly, in the case of impermeable river training works like geobags (Figure 4.1), local scouring is unavoidable and can lead to failure due to overtopping, sliding, puncturing, and pull-out dislodgement (Akter et al., 2012; Hossain, 2016). Scour hole formation occurs even in structures other than river groynes, such as Longitudinal Training Dams (Vermeulen et al., 2018; Wal, 2020). Under these circumstances, it is necessary to technically

supervise the design of river training works before their deployment in large rivers (Wal, 2020). Physical model experiments are required to investigate these phenomena, but they have limitations such as high cost, time-consuming, the uncertainty of scale effect, and limited measuring points (Jing et al., 2002; lin Tang et al., 2007; Kalita et al., 2014; Gu et al., 2016; Kalita, 2020). Due to these constraints, numerically-based river models are used, which are more practical for simulating near-actual field conditions (Molls et al., 1995; Mohapatra, 2006; lin Tang et al., 2007; Kalita et al., 2014; Taormina and Chau, 2015; Gu et al., 2016; Karmaker and Dutta, 2016; Naik et al., 2018; Das, 2018; Mali et al., 2020). They are regarded as effective adaptive management approaches that can be used to test hypotheses that interpret various river processes (Kidova et al., 2021).

Several research studies have already been conducted using physical models to study the behaviour of various river training structures (Teraguchi et al., 2010; Sarker et al., 2011; Rahman and Osman, 2015; Aamir and Sharma, 2015). According to Oberhagemann (2011) and Aamir and Sharma (2015), porcupine and geobag layouts resulted in significant reductions in flow velocity and promoted sediment deposition. Several researchers, on the other hand, have used numerical river models in various river training work studies. Gao (2009) used *2D FLUENT* to model concrete tetrahedral frame revetments, Jia and Wang (1999) used *CCHE-2D*, Karmaker and Dutta (2016) used *2D MIKE 21C*, Gu et al. (2016) used *3D FLUENT*, and Gilja et al. (2019) used *HEC-RAS* along with *MIKE21fm* to simulate groyne fields. However, little research has been conducted into the ability of higher-order numerical models to simulate river training works (Karmaker and Dutta, 2016; Chowdhury et al., 2018).

In this study, a porcupine screen, geobag, and a hybrid layout combining these have been modelled using the *CCHE-3D* and *OpenFOAM* models. In the *CCHE-3D* model, due to model constraints, the inclined members were represented as vertical members. In the *OpenFOAM* model, the actual model has been incorporated along with a parametric study, a detailed study of the hydrodynamic effects, as well as experimental calibration and validation.The primary goals of this study are to compare the performance of the open-source numerical-based hydrodynamic model *OpenFOAM* to the commercial CCHE-3D model, and highlight its use in analyzing performance of engineered river training works, as compared to nature based solutions. The Semi-Implicit Method for Pressure-Linked Equations (*SIMPLE*) algorithm (Patankar and Spalding, 1972) of *OpenFOAM* requires less computational time and resources. Previously, this model, along with experimental validation was used for simulation of jets (Ardalan and Vafaei, 2019; Ramezani et al., 2021) and spillways (Kocaer and Yarar, 2020). Some work has also been done with multiphase solvers in *FLUENT* (Gu et al., 2016) and *OpenFOAM* (Kocaer and Yarar, 2020)

with satisfactory results. However, due to the higher computational requirements of multiphase solvers and the relatively simple problem definition in this study, the *simpleFOAM* solver for single-phase steady and incompressible flow in *OpenFOAM* has been used. The best layout out of permeable river training work (porcupine), impermeable river training work (geobag), their combination (hybrid) and a commonly seen riparian vegetation (mangrove) structure has been chosen based on its ability to reduce velocity and divert flow. Further, their ability to produce lateral velocity components have been accessed, which are primarily responsible for nutrient exchange mechanisms observed in the previous chapter. Understanding the response of various river training works before implementation will significantly assist in river management, and will help in designing the most economical-*cum*-optimum layout suitable for a river reach, thus reducing their chances of failure.

4.3 Methodology

A 20 m × 1 m experimental setup was replicated within the three-dimensional hydrodynamic models *CCHE-3D* and *OpenFOAM*. The numerical models were calibrated with experimental results for engineered river training works such as porcupines, geobag, and a hybrid layout combining these. The validation results obtained for the *CCHE-3D* model were not satisfactory. Therefore, only the *OpenFOAM* numerical model, that was calibrated using engineered structure models in the laboratory, was used for accessing performances of both engineered as well as mangrove root structures in reducing longitudinal flow velocity, as well as generating secondary currents responsible for nutrient exchange mechanisms. This section discusses the adopted methodology in detail.

4.3.1 Experimental setup

All experiments have been carried out at the Fluvial Hydro-Ecological Laboratory at IIT Guwahati. The schematic diagram of its flume is shown in Figure 4.1. The flume has a sand bed, with a tray length and width of 18 m and 4 m respectively. But the width of the flume has been restricted to a 1 m width for this study. Two 15 $H.P.$ pumps and one 10 $H.P.$ pump are being used to drive and recirculate the flow between a hilltop tank, channel, and underground sump. To reduce the flow turbulence, some rough stones were put near the upstream

collecting chamber. The flumes' slope has been set to 3/2000 throughout the experiments. The bed is made of Brahmaputra rivers' sand with a median diameter of 5×10^{-4} m and a density of 2650 kg/m^3. The discharge in this flume is measured using a triangular notch at the flumes' upstream end, and the flow depth is measured using a digital point gauge. A three-dimensional Acoustic Doppler Velocitymeter (Nortek, 4 probes, 10 MHz Vectrino A.D.V.) is used to obtain instantaneous velocity measurements at a sampling frequency of 200 Hz. To remove spikes in the data, the obtained velocity time series has been processed using the accelerating threshold algorithm (Goring and Nikora, 2002). To conduct the experiments, a 0.69 m long and 0.28 m wide test section has been prepared at the flumes' centre, where the flow is fully developed to minimise upstream entry, downstream exit, and wall effects. Clear water and a Shields' parameter value of 0.045 have been used to simulate incipient motion in the experiments (Aamir and Sharma, 2015). Permeable and impermeable structure models have been placed in the centre of the test section, and flow characteristics have been determined through experiments. Porcupines have been fabricated using 7×10^{-3} m iron rods and geobags have been made using cloth bags with a 0.06 m diameter (equal to porcupine screen height).

4.3.2 River training works placement

A porcupine screen, a geobag screen, a hybrid layout and a mangrove structure (Figure 4.1) have been analysed using the *OpenFOAM* numerical model. The hybrid layout (Figure 4.1) is a combination of porcupine screens followed by geobag screens. With this design, the geobags' tip is less likely to be struck by high incoming velocity, which could result in scour holes. In this way, riverbank erosion could be addressed more effectively. The various layouts that have been used in this study are listed in Table 4.1.

4.3.3 Three-dimensional hydrodynamic flow modelling

In this study, initially both the finite volume-based *CCHE-3D* and *OpenFOAM* models were used, but due to the poor validation results of *CCHE-3D* model, it was only used for preliminary analysis. The *OpenFOAM* hydrodynamic model has been calibrated based on data collected in the laboratory for the cases of single-screen porcupine and geobag. After that, cases of dual-screen porcupine

Table 4.1: Various layouts of river training work tested in this study. '△' represents porcupine screen and '⟺' represents geobag screen

Layout Name	Porcupine/ Geobag screen layout	Hybrid layout
Single-screen porcupine	△△△	△△△ ⟺
Dual-screen porcupine	△△△ △△△	–
Geobag	⟺	–

and hybrid layouts have been used to validate it. Because of the lower computational requirements and the consideration of steady and incompressible flow in this case, the *simpleFOAM* (https://openfoamwiki.net/index.php/SimpleFoam) solver in *OpenFOAM* has been used. This iterative solver employs the *SIMPLE* algorithm (Patankar and Spalding, 1972) to solve the Navier-Stokes Equations. The $\kappa-\omega$ SST model (Menter, 1993, 1994), which combines the $\kappa-\varepsilon$ (Launder and Spalding, 1974) and $\kappa-\omega$ (Wilcox, 1988, 1993, 1994) turbulence models and outperforms these models in modelling free flow (Kocaer and Yarar, 2020), has been used to model turbulence.

4.3.3.1 OpenFOAM model governing equations

The continuity equation and three-dimensional Navier-Stokes equations are solved while the flow has been assumed to be steady and incompressible. In this case, the fluid under consideration has been clear water with uniform properties throughout. The no-slip boundary condition has been taken into account at the solid boundaries of the flow domain and the placed structures. The bed and banks of the flow domain have been assumed to be non-erodible, and the temperature effects on water viscosity have been ignored. Taking these assumptions into consideration, the continuity and momentum equations take the following form:

$$\frac{\partial u_i}{\partial x_i} = 0 \tag{4.1}$$

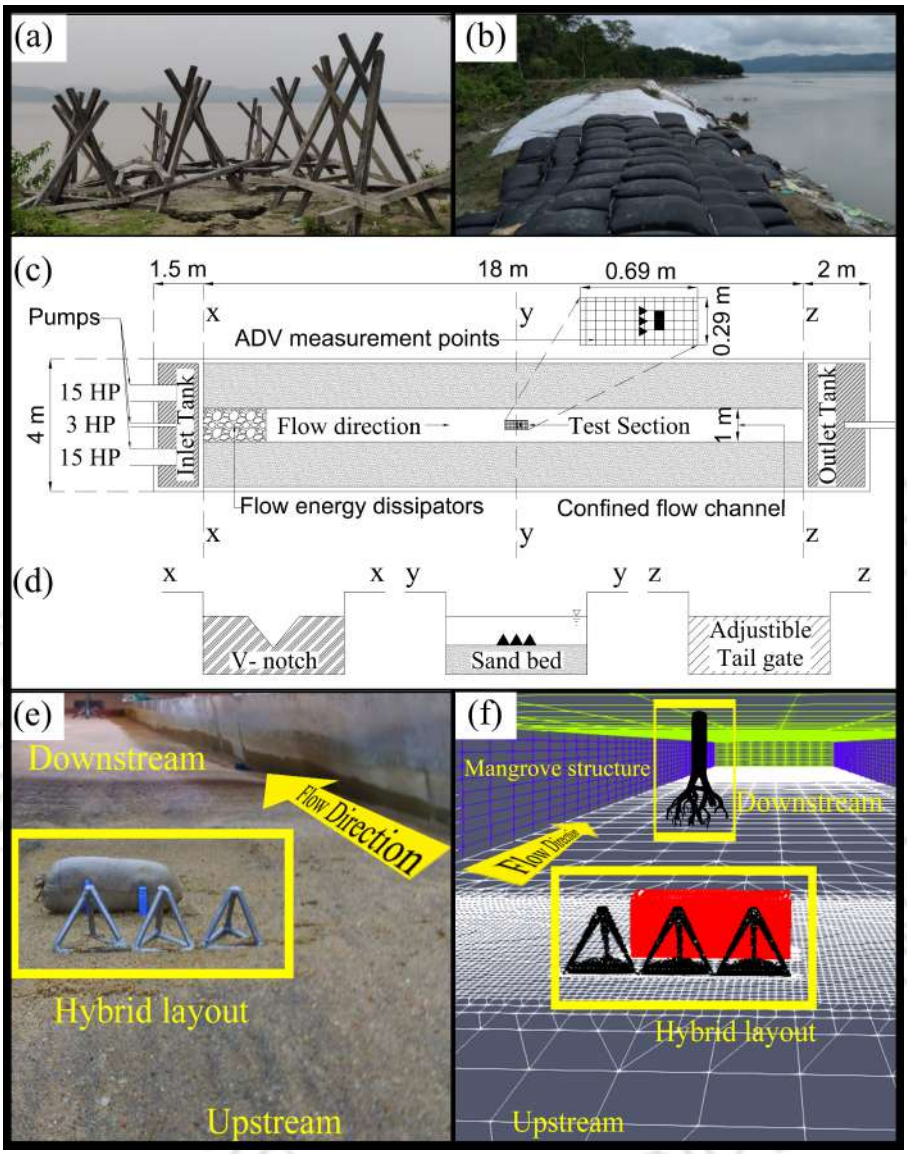

Figure 4.1: (a) Porcupines under emergent condition being deployed in the Brahmaputra river (b) Geobag embankment used for bank protection in the Brahmaputra river (c) Plan schematic view of the experimental flume (d) Cross-sectional schematic view of the experimental flume (e) Hybrid model in experiments (f) Hybrid model and mangrove structure in OpenFOAM

$$\frac{\partial u_i}{\partial t} + u_j \frac{\partial u_i}{\partial x_j} = -\frac{\partial p}{\partial x_i} + \frac{\partial}{\partial x_j}\left(\nu \frac{\partial u_i}{\partial x_j}\right) \tag{4.2}$$

Here, x_i and x_j represent the coordinate axes. The velocity magnitudes

corresponding to the x, y and z axes in the cartesian coordinate system are represented as u_i and u_j in the directions of $i, j = 1, 2$ and 3. Furthermore, ρ_f denotes fluid density, ν denotes fluid kinematic viscosity, p denotes pressure, and t denotes time. The equations for turbulence kinetic energy (κ), turbulence specific dissipation rate (ω), and turbulence viscosity (ν_T) are as follows:

$$\frac{\partial \kappa}{\partial t} + u_j \frac{\partial \kappa}{\partial x_j} = P_k - \beta^* k\omega + \frac{\partial}{\partial x_j}\left\{(\nu + \sigma_\kappa \nu_t)\frac{\partial k}{\partial x_j}\right\} \tag{4.3}$$

$$\frac{\partial \omega}{\partial t} + u_j \frac{\partial \omega}{\partial x_j} = \alpha S^2 - \beta\omega^2 + \frac{\partial}{\partial x_j}\left\{(\nu + \sigma_\omega \nu_t)\frac{\partial k}{\partial x_j}\right\} + 2(1 - F_1)\sigma_{\omega 2}\frac{1}{\omega}\frac{\partial \kappa}{\partial x_i}\frac{\partial \omega}{\partial x_i} \tag{4.4}$$

$$\nu_t = a_1 \frac{\kappa}{max(a_1\omega, SF_2)} \tag{4.5}$$

The closure coefficients and auxiliary relations used in the previous equations are as follows:

$$P_k = min\left(\tau_{ij}\frac{\partial u_i}{\partial x_j}, 10\beta^*\kappa\omega\right) \tag{4.6}$$

$$F_1 = \tanh\left\langle\left[min\left\{max\left(\frac{\sqrt{k}}{\beta^*\omega y}, \frac{500\nu}{y^2\omega}\right), \frac{4\sigma_{\omega 2}\kappa}{CD_{k\omega}y^2}\right\}\right]^4\right\rangle \tag{4.7}$$

$$F_2 = \tanh\left[\left\{max\left(\frac{2\sqrt{\kappa}}{\beta^*\omega y}, \frac{500\nu}{y^2\omega}\right)\right\}^2\right] \tag{4.8}$$

$$CD_{\kappa\omega} = max\left(2\rho_f\sigma_{\omega 2}\frac{1}{\omega}\frac{\partial k}{\partial x_i}\frac{\partial \omega}{\partial x_i}, 10^{-10}\right) \tag{4.9}$$

$$\phi = \phi_1 F_1 + \phi_2(1 - F_1) \tag{4.10}$$

$$\alpha_1 = \frac{5}{9}, \alpha_2 = 0.44; \beta_1 = \frac{3}{40}, \beta_2 = 0.0828, \beta^* = \frac{9}{100} \tag{4.11}$$

$$\alpha_{k1} = 0.85, \alpha_{k2} = 1; \sigma_{\omega 1} = 0.5, \sigma_{\omega 2} = 0.856 \tag{4.12}$$

Here, F_1 (Equation 4.7) and F_2 (Equation 4.8) are blending functions. Terms α_1 (Equation 4.11) and β_1 (Equation 4.11) are defined in the original model, while terms α_2 (Equation 4.11) and β_2 (Equation 4.11) are defined in the transformed model. The terms α (Equation 4.4) and β (Equation 4.4)

in the *SST* model are obtained by multiplying the corresponding terms in the equation with F_1 in $\kappa - \omega$ equation and in the transformed $\kappa - \varepsilon$ model with $(1 - F_1)$ and then adding them. After being discretized using the Finite Volume Approach and then using the *SIMPLE* algorithm, these equations are numerically solved. More details on the *OpenFOAM* model are presented in Appendix B.

4.3.3.2 Model implementation

River training works are typically found in either emergent or submerged conditions in the field, depending on the incoming flow conditions. They work well in low-flow situations. When there is a considerable amount of flow, these structures can become unstable because of the complex flow interactions around them. Accordingly, *OpenFOAM* steady flow simulations have been used to evaluate river training works such as porcupine screens, geobags, and hybrid layouts in submerged conditions, *i.e.*, when the water level is greater than the structure's height. For each case, the simulation time has been set to 10 hours, with a time step of 1 second. Following the simulations, the results have been extracted using *OpenFOAM*s' probe function along the depth and transect profiles. The *ParaView* utility (https://www.paraview.org) has been used to extract data for velocity contours, streamlines, and vectors. The above results have been further processed and plotted in the *Python IDE* (https://www.python.org) using the *matplotlib* module (https://matplotlib.org). These results are presented and discussed to understand better the flow patterns and hydraulics generated in the numerically modelled laboratory channel. The computational mesh has been generated using *OpenFOAM*'s *blockMesh* utility, which generates parametric meshes with grading and curved edges based on the experimental setup. The domain geometry has been decomposed into a set of one or more three-dimensional hexahedral blocks by this utility. This tool has been used to develop a mesh with 10,000 evenly spaced cells. The dimensions of each cell were 0.2 m x 0.1 m x 0.02 m. Then, porcupines and geobags were added to the model by making them into objects (*.stl* file format) in *FreeCAD*, an open-source *CAD* software (https://www.freecadweb.org). These objects have been placed in the centre of the initially generated mesh using *OpenFOAM*'s *snappyHexMesh* utility. At these locations, the grids gradually become finer. Thus, the total number of grid points in the final mesh varied considerably depending on the object's geometry. Additionally, the channel and object boundaries have been regarded as non-slip and non-erodible with the help of a wall function defined as *kqRWallFunction* within *OpenFOAM*. The *kqRWallFunction* approximates the zero-gradient condition for turbulent kinetic

energy (k), the square root of turbulent kinetic energy (q), and Reynold's stress tensor fields (R) in cases of high Reynolds number flow using wall functions. A series of parametric studies have been carried out to determine the optimal distance between the two objects as well as the optimal height of the geobag object. Once this distance and height have been established, they have been used in all hybrid layout cases.

4.3.3.3 Boundary conditions

The water level has been used as a downstream boundary condition, and the corresponding discharge has been calculated using Mannings' formula, which has been used as an upstream boundary condition. The Mannings' roughness coefficient has been obtained from Stricklers' formula using d_{50} for Brahmaputra rivers' sand (Dubey et al., 2014). As for this case, the downstream water level has been considered to be 0.2 m and the corresponding discharge has been calculated to be 0.023 m^3/s.

4.3.3.4 Calibration and validation of the model

The *OpenFOAM* model setup has been calibrated and validated in this study using measured velocity profiles from laboratory experiments conducted at the Indian Institute of Technology Guwahati. These velocity profiles have been obtained by placing scaled-down models of porcupines, geobags, and hybrid layouts in the laboratory flumes' test section and then measuring velocity using *ADV*. Single-screen porcupine and geobag layouts have been used for calibration, while dual-screen porcupine and hybrid layouts have been used for validation. The calibration and validation curve's (Figure 4.2) have been obtained by comparing the ratio's y'/Y_{max} and u/U_{avg} for experimental and simulated cases, where y' denotes the depth of the measurement location from the flume bed, Y_{max} denotes the total flow depth, u denotes the velocity at the measurement location, and U_{avg} denotes the depth averaged velocity at that location. The model has been run with a flow Froude number of 0.082 under subcritical flow conditions. As shown in Figure 4.2, the model has been calibrated and validated at three different locations: upstream, downstream, and in a zone of velocity deflection, which is in relation to the placement of the models of river training works. Ratios have been used to reduce the effects of approximations to model governing equations. Also, due to approximations, experimental and numerical modelling results differ. These distinctions, however, can be

overlooked because the goal of this research is to compare commonly used river training works based on the obtained velocity profiles. As shown in Figure 4.2, the model can reproduce the general behaviour of porcupine and geobag structures in the flume ($R^2 > 0.74$). Similar results have been obtained when the calibration results have been validated using the dual-screen porcupine and hybrid layout.

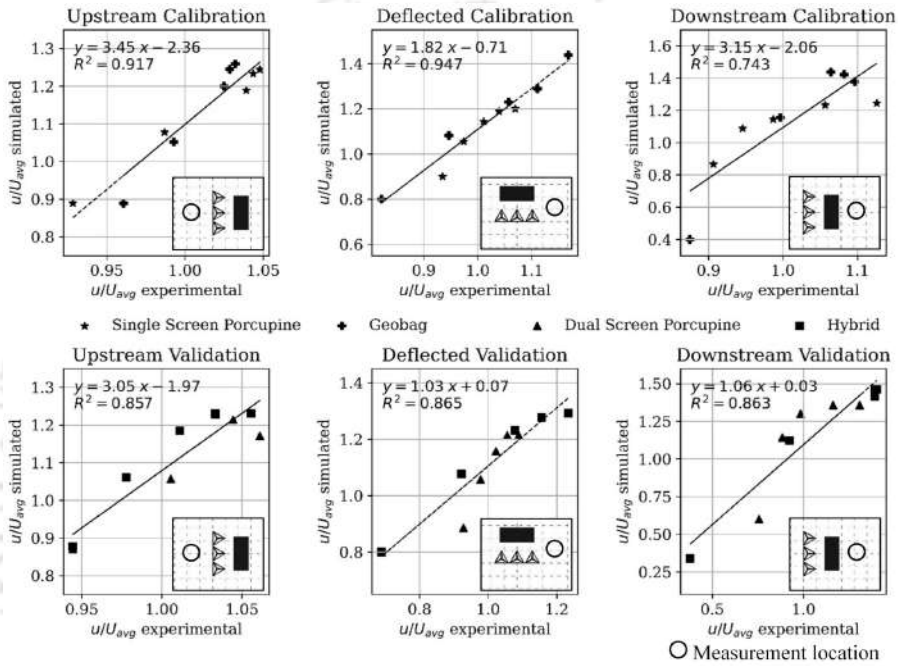

Figure 4.2: Calibration and validation results. R^2 for all the cases is above 0.74 for both calibration and validation.

4.4 Results

It was observed from the *CCHE* model simulation results that porcupine screen's provided considerable reduction in flow velocity which increases with number of porcupine screen's. In emergent case, dual screen porcupines reduced the velocity by 90%, followed by 50% by single screen porcupines. In deflected zone, the velocity increased by 85% in dual screen followed by 42.9% in single screen porcupine's. In the transition case, velocity reduction was 9.6% in case of dual screen porcupine's followed by 4.4% in case of single screen porcupine's. Thus, in case of high submergence, the effect of porcupine's in flow deflection

and velocity reduction was found to be negligible; hence, porcupine's are not suitable for high flow conditions. On the other hand, hybrid layout was also found to be most effective in emergent condition. The velocity reduction of a hybrid layout when compared with a geobag layout was found to be almost the same (94.36%). However in deflected region, the velocity of flow increased by 97.85% in dual screen hybrid, followed by 88.60% in single screen hybrid and 76.17% in only geobag layout, respectively. In the transition case, velocity reduction was 91.59% in case of dual screen hybrid, followed by 91.13% in single screen hybrid and 86.78% in only geobag layout. In the deflected region, the velocity of flow increased by 79.85% in case of dual screen hybrid layout, followed by 77.25% in case of single screen hybrid layout and then by 73.10% in case of only geobag layout. In submerged case, velocity reduction was 82.20% in dual screen hybrid and 77.29% in single screen hybrid and only geobag layout. In the deflected region, the velocity of flow increased by 59.49%, 54.21% and 50.25% in dual screen hybrid, single screen hybrid and only geobag layout, respectively. Even after using representative vertical members as a substitute for inclined members of the actual porcupine structure, it was observed that the *CCHE* model could replicate the trend that was observed both in the experimental and OpenFOAM numerical model study. However, the range of velocity obtained in the deflected and downstream zones are overpredicted by the model. On the other hand, *OpenFOAM* calibration and validation using experimental data have yielded satisfactory results ($R^2 > 0.74$). The model has been further used to evaluate the performance of various other commonly used layouts, their combinations, along with a nature based mangrove root structure.

4.4.1 Optimum parameters for the hybrid layout

An OpenFOAM simulated parametric study has been performed to design the best hybrid layout by varying the distance between the porcupine and the geobag as well as the height of the geobag. Table 4.2 lists these variable parameters. The probe function in OpenFOAM has been used to obtain velocity values at the upstream, downstream, zone of flow deflection, and two horizontal and three transverse transects, as shown in Figure 4.2. To define the geobag height, the height of the porcupine screen has been used as a reference. Similarly, the distance between the porcupine screen, and the geobag screen has been defined in terms of porcupine height. A number has then been assigned to each parameter combination.

The velocity measurements have been taken using probe function at a

Table 4.2: Details of hybrid layouts tested in the parametric study

Case No.	Flow condition	Porcupine height	Distance	Geobag height
1	Submerged ($Q = 0.023\ m^3/s$, $Y_{max} = 0.2\ m$)	H	0.5H	0.5 H
2		H	0.5H	H
3		H	H	0.5 H
4		H	H	H

height just above the height of geobag in cases 1 and 3 (0.0375 m), and this height is being used for measurements in the rest of the cases. This must be done to assess the effect of a submerged geobag in conjunction with an emergent porcupine in the hybrid layout. First, the case where no structure was being placed has been simulated, followed by the other cases. Then, for each case (other than the first), the percentage velocity decrease downstream and increase in the deflection zone have been calculated in comparison to the first case, *i.e.*, when no structure is present. The length of the zone of influence has been calculated by taking the maximum dimension of the low-velocity zone in the velocity contours. It has been extracted with *GIMP* open-source image processing software (https://www.gimp.org) at the node near the same depth previously determined (i.e., 0.0375 m), and the zone of influence length obtained has been normalised with the magnitude of velocity obtained at that zone. The findings are depicted in Figure 4.3.

4.4.2 Performance evaluation of layouts

In this study, five cases have been investigated: single-screen porcupine, dual-screen porcupine, geobag layout, a hybrid layout and a mangrove root structure. The parametric study results from section 4.4.1 have been used to select the optimal hybrid layout. Figure 4.4 depicts a sketch of a 3D hybrid layout model that has been used for simulation. Figure 4.4 also illustrates the locations of these structures in the numerically modelled flume.

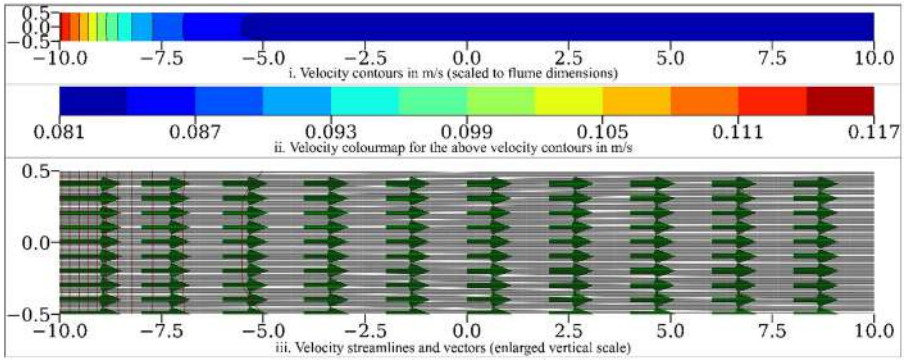

(a) No structure placed

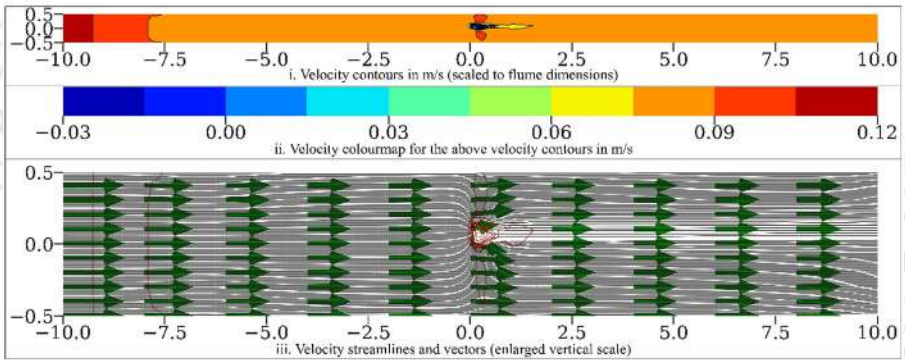

(b) Case 2: Distance between the porcupine and geobag is equal to half of the porcupine height

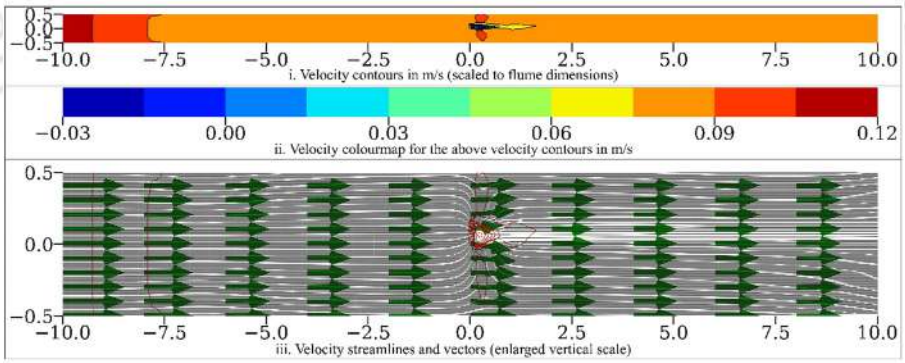

(c) Case 4: Distance between the porcupine and geobag is equal to the porcupine height

Figure 4.3: Velocity contour maps, streamlines and vectors for no structure, case 2 and case 4 respectively

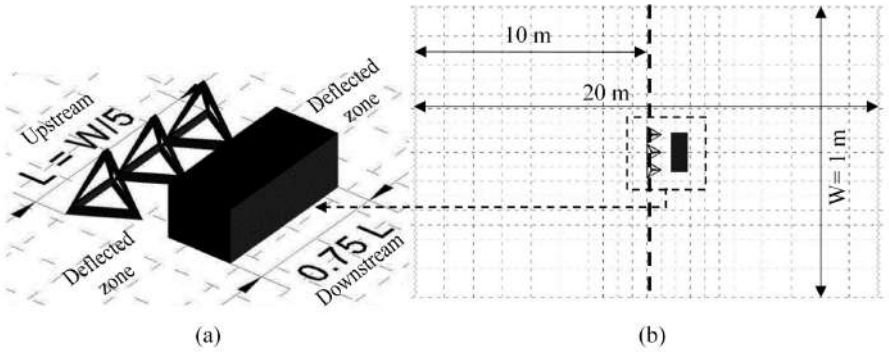

Figure 4.4: (a) 3D view of the model of the hybrid layout used (b) Schematic diagram showing dimensions of model geometry (not to scale)

4.5 Discussion

OpenFOAM was found to be more effective than *CCHE* at reproducing velocity fields acquired in the performed experiments due to its ability to simulate inclined members under the identical conditions. From the parameteric study using *OpenFOAM*, it can be seen that on an average, increasing the height of the geobag increased the effect of velocity reduction downstream by 8%. There has been a fairly small (0.57%) but still increasing effect in the deflection zone. On the other hand, increasing the distance between the porcupine screen and the geobag causes the effect of velocity reduction at downstream to be increased by 2.3% on average, and the effect of velocity increase at the deflection zone to be increased by 1.32% on average. Thus, the height of the geobag has been a major factor in velocity reduction. The velocity increase at the outer bank, on the other hand, has been dominated by the distance between the porcupine and the geobag. Case 2 (Figure 4.3) is found to be the most optimal layout in terms of overall performance in terms of flow velocity reduction, flow deflection, and the distance up to which the effect of the layout persists. In other words, by reducing the distance between the porcupine screen and the geobag and increasing the height of the geobag, the two structures function as a single unit rather than as two separate units. Before reaching the impermeable structure, the permeable structure reduces the intensity of the incoming flow. It dissipates flow energy to the point where the flow can no longer scour the bed. The flow is then diverted by the impermeable structure. However, if these units are placed too close together, they may become structurally unstable, and placing these units too close together may not be practical. These aspects

are beyond the scope of the current study. This parametric study thus shows that increasing the geobag height and decreasing the distance between the two structures improves the performance of the hybrid layout. Correspondingly, the hybrid layout tested in section 4.3.2 has been designed with the distance between the porcupine, and the geobag being less than the porcupines' height, and the geobags' height being equal to the porcupines' height.

For a comparison between the five cases *viz.* single-screen porcupine, dual-screen porcupine, geobag layout, hybrid layout and a mangrove root structure, similar to the parametric study, the performance has been evaluated based on the extent of longitudinal velocity reduction towards the downstream and flow diversion (due to secondary currents) towards the opposite bank. The best layout has been determined by its ability to dissipate the most energy, *i.e.*, more velocity reduction downstream and more flow deflection towards the opposite bank. When no structure is present, the longitudinal velocity profile has a vertical trend in the boundary layer region and a logarithmic trend in the remaining region due to the application of the wall boundary condition. When a logarithmic profile has been fitted, the following equation is obtained:

$$u = 0.0377\,(y') + 0.2059; (R^2 = 0.9642) \tag{4.13}$$

The velocity profiles in Figure 4.5 show that the longitudinal velocity at the downstream is greatly reduced, except for single-screen porcupine towards the downstream, which is due to less correlation, as shown in Figure 4.2. The flow surrounding the geobag layout will have less energy as a consequence of the porcupine screens' reduction in the longitudinal velocity. Hence, the porcupine screen will keep the geobag safe from scour hole failure.

The velocity profiles along a longitudinal transect in Figure 4.6 show the same trend and are comparable to the results obtained by Aamir and Sharma (2015). They too reported that increasing the number of porcupine screens causes a greater reduction in flow velocity and a longer zone of low velocity. Figure 4.5 also demonstrates that increasing flow depth reduces the impact of these river training structures, which is again consistent with their findings. Moreover, for hybrid and geobag layouts, an impermeable geobag structure causes a significant decrease in velocity between flow depths of 0.025 m and 0.075 m (Figure 4.5). Therefore, for engineered structures, the hybrid layout performs better in terms of velocity reduction and flow diversion. However, the performance of mangrove structure is much better, except that the depth from which significant longitudinal velocity reduction starts is beyond 0.075 m (Figure 4.5). It has also been found to be more effective at deflecting the flow. The velocity distributions in a transverse transect to the flow direction are depicted in Figure 4.6 at the upstream, centre, and downstream. The tested

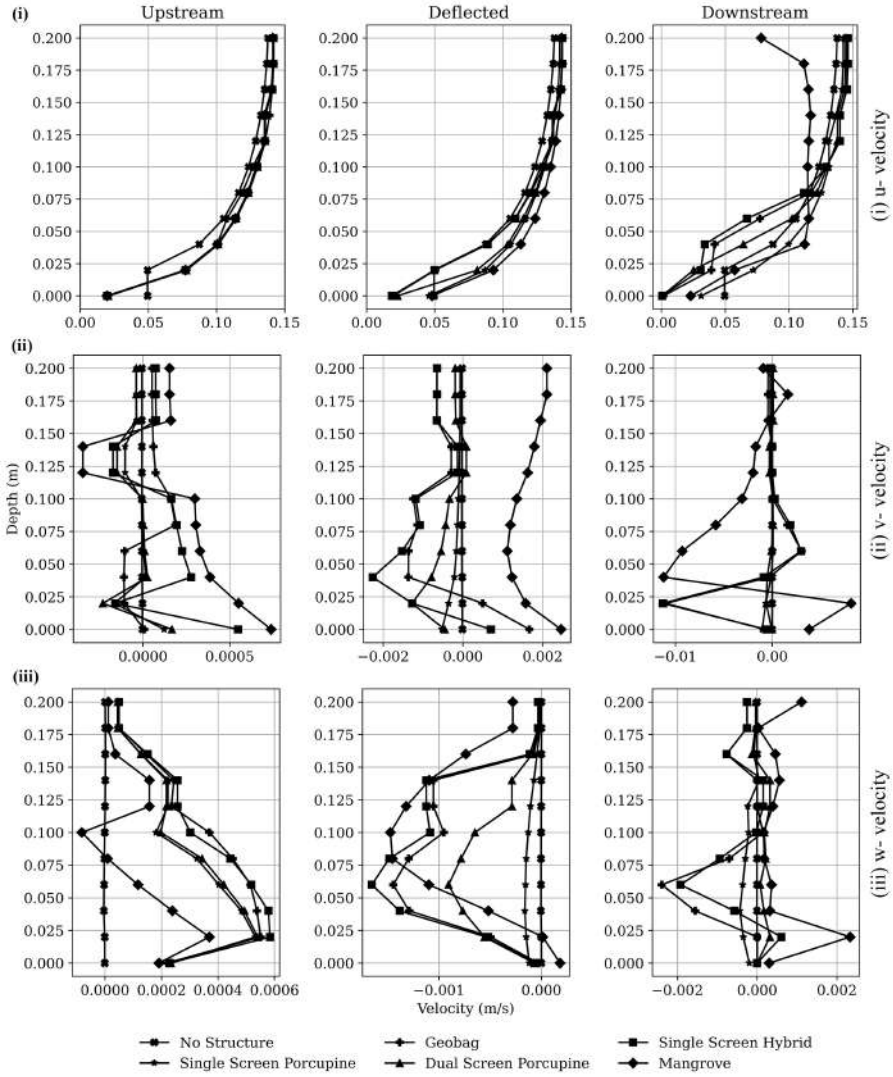

Figure 4.5: Velocity profiles along depth. Logarithmic velocity profile is obtained due to wall boundary condition (kqRWallFunction).

river training works are found to have a much stronger effect in the longitudinal direction than in the transverse direction. Furthermore, Figure 4.6 show that the effect of reduced flow velocity downstream is much stronger than the effect of increased flow velocity at the flow deflection zone. This will eventually assist dissipate flow energy and thereby reduce bank erosion.

Figure 4.7 depicts the results of performance comparisons in terms of downstream velocity reduction, deflected zone velocity increase, and zone

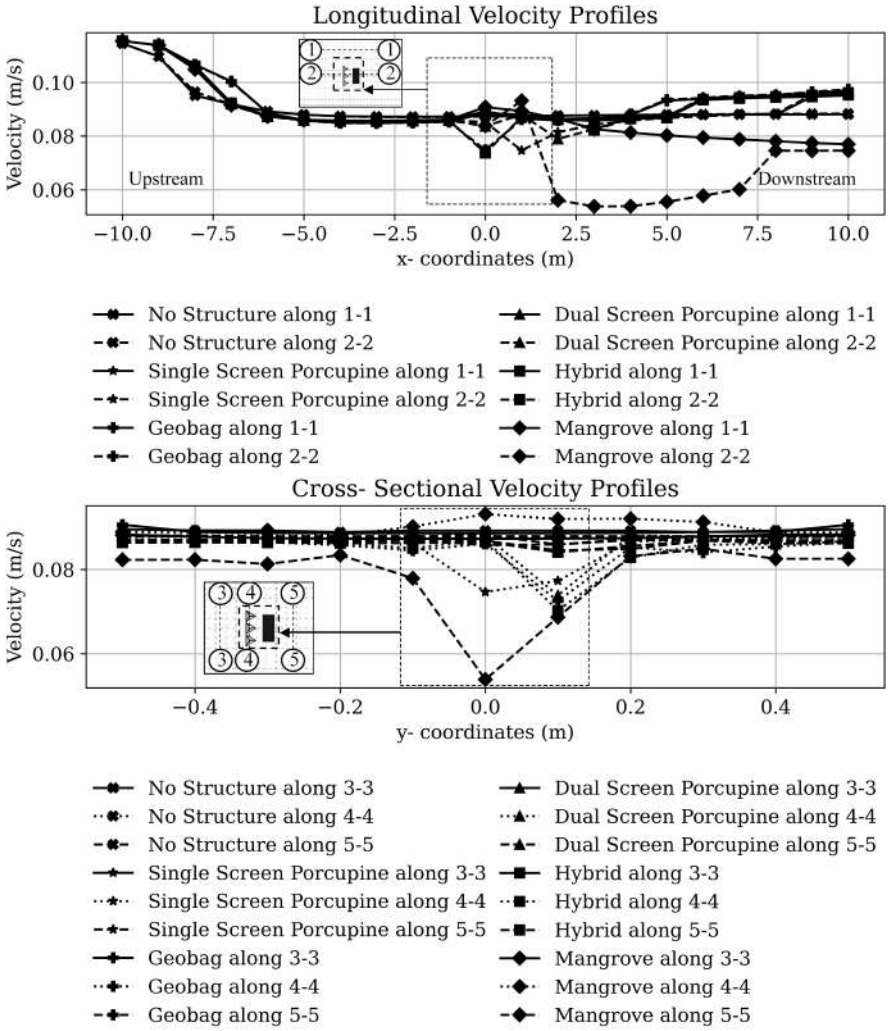

Figure 4.6: (a) Longitudinal velocity profiles. Flow velocity reduction is dominating the flow deflection (b) Cross-sectional velocity profiles. The influence of river training is most prominent in the central (4-4), followed by downstream (5-5) and then by upstream transect (3-3)

of influence. In downstream velocity reduction, the hybrid layout is 1.33%, 11.62%, and 13.34% more efficient than the geobag, dual-screen porcupine, and single-screen porcupine, respectively. Similarly, in terms of velocity increase at the deflection zone, the hybrid layout is 0.49%, 0.65%, and 0.92% efficient, respectively. The hybrid layouts' porcupine screen reduces flow velocity before it reaches the geobag, lowering the likelihood of scour hole formation at the impermeable structure's nose. The flow is then diverted to the opposite bank

by the impermeable structure (Figure 4.7). As a result, if placed in an area prone to bank erosion, this layout may be more effective in protecting the bank.

On the other hand, the mangrove structure is more efficient than hybrid layout by 0.75% in flow velocity reduction and 1.09% in deflection. For this reason, the mangrove structure is the most effective of the cases tested, even more than the hybrid layout, which combines the advantages of permeable and impermeable structures. It also produces significant amounts of secondary currents, which might act as a mechanism to drive the nutrient exchange mechanisms between river and riparian vegetation zones. Practical applications and pilot projects in riverbank erosion and water quality problems that occur in the field will improve our understanding of river response to the tested layouts.

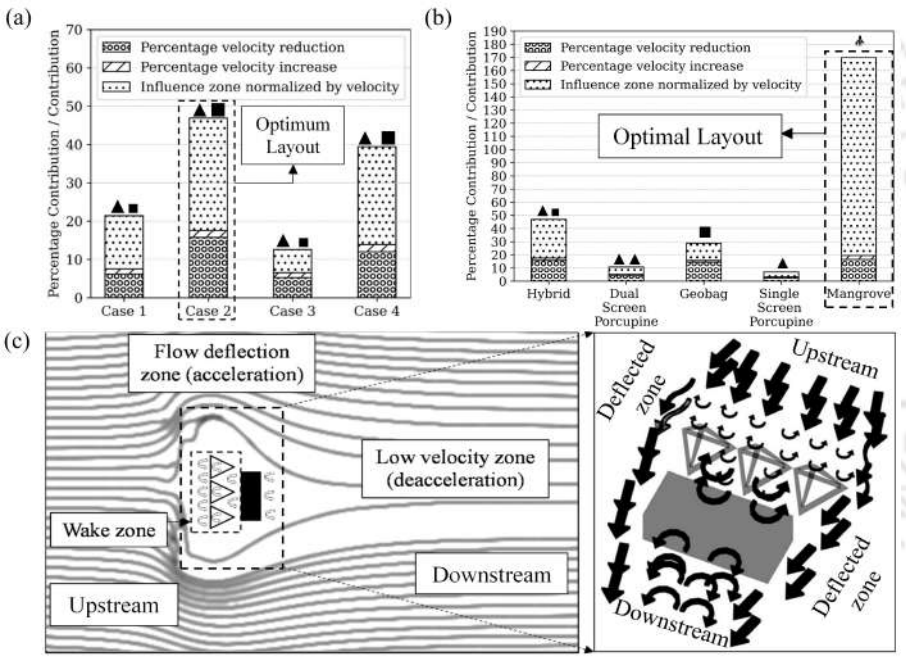

Figure 4.7: (a) Parametric study results for obtaining optimum hybrid layout. Details of the cases are shown in Table 4.2. (b) Overall performance of hybrid ($\triangle \Longleftrightarrow$), dual-screen porcupine ($\triangle\triangle$), geobag ($\Longleftrightarrow$), and single-screen porcupine ($\triangle$) layouts. The performance of hybrid is found to be the best out of all layouts tested in this study (c) Flow streamlines and turbulence patterns generated by the hybrid layout

Based on the results presented above, it can also be seen that low computational requirements algorithms, such as *SIMPLE*, can be used to conduct investigations to aid in the preliminary design of river training works. In the same way, more detailed hydro-ecological analyses can be done with more

complex multiphase models that can better represent the flow physics and nutrient balances.

4.6 Summary

An attempt has been made in this chapter to model the nutrient exchange mechanisms observed in the previous chapter using hydrodynamic modelling. The comparative performance of engineered structures, *viz.*, porcupine, geobag, and a combined hybrid layout, with that of natural mangrove structures as a means of river training has been assessed. The evaluation of performances is based on the degree of longitudinal velocity reduction towards the downstream and flow diversion towards the opposite bank, which are caused by the generated secondary currents, that may be considered as a mechanism that drives the nutrient exchanges. The analysis carried out in this chapter demonstrated that the mangrove structure outperforms engineered river training works, thus offering a feasible nature-based solution for mitigating river bank erosion, allowing better exchange of nutrients between river and riparian zone, thereby improving water quality.

5

Conclusions and future scope

This chapter provides an overview of the thesis and a roadmap for the future

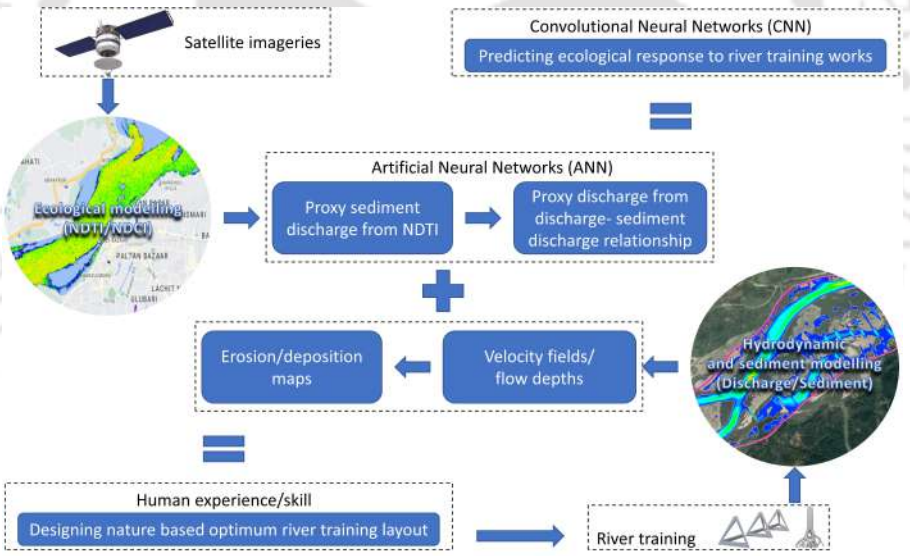

Contents

5.1 General

This is the concluding chapter of the thesis. The summary of the thesis is presented in the first section. It is followed by the section describing the future prospects.

5.2 Summary

There have been numerous studies on the estimation of water quality using satellite remote sensing. These studies have used Artificial Neural Networks (ANN) based models or indices like the $NDCI$ to predict $chl-a$ concentrations in selected regions. However, in order to comprehend coupled natural processes, multiple parameters must be studied simultaneously. The app developed in this study aims to enable monitoring of multiple river water quality parameters and terrestrial ecological parameters using both raw and level 2 satellite imageries, which can be very beneficial for water resources planning and management on a near real time basis. The aforementioned multiparameter analysis capabilities can help in enhancing the current understanding of coupled natural systems.

Using the app developed in this study, it has been found that nutrients play a significant role in the quantity and health of vegetation in an ecosystem. This was indicated by overall accuracies of 86 and 92, which were equivalent to Cohen Kappa values of 69 and 86 percent, respectively between $GNDVI$ with $NDVI$ in non-riparian areas. Overall accuracies of 97 and 100 percent were also found for riparian zones, which translate to a 94 and 100 percent Cohen Kappa, respectively. In the case of riparian vegetation zones, a constant nutrient exchange mechanism exists between the river and the riparian vegetations on its flood plains, which helps to maintain the ecological balance of the river ecosystem. These nutrient exchange mechanisms can be attributed to the turbulence structures generated by the riparian vegetation, which generates significant amount of lateral velocity components. Based on these principles, an optimal nature-based river training work can be designed along river banks, which could serve as an efficient and long-term solution to the water quality problems.

To design of the optimum nature based river training work, hydrodynamic studies can be conducted. Previous studies indicate that permeable river training works are a popular and cost-effective alternative for training a braided

river. However, during times of heavy flooding, these structures frequently fail to perform adequately. Impermeable structures, on the other hand, have the disadvantage of scour hole formation at the nose. Taking into account the foregoing, a novel hybrid layout has been tested in this study, which has the benefit of impermeable and permeable river training works. Model calibration and validation using experimental data have yielded satisfactory results ($R^2 > 0.74$). The model has been used to evaluate the performance of various other commonly used layouts and their combinations. In this study, it has been discovered that reducing the distance between the structures in a hybrid layout increases the layouts effectiveness by allowing it to function as a single unit. In addition, the hybrid river training layout has been the most effective of all the engineered river training cases studied. It reduces velocity by 1.33%, 11.62%, and 13.34% in its immediate downstream compared to geobag, dual-screen porcupine, and single-screen porcupine, respectively. Similarly, the flow diversion towards the opposite bank increases by 0.49%, 0.65%, and 0.92%, respectively. In addition, the performance of a natural mangrove structure was compared to that of the engineered porcupine, geobag and hybrid structures, and the role of its generated secondary currents in driving the nutrient exchange mechanisms in riparian vegetation zones was investigated. The mangrove structure has been found to be more efficient than hybrid layout by 0.75% in flow velocity reduction and 1.09% in deflection. However, to effectively regulate pollution as well as minimise bank erosion in Indian rivers, the ultimate design should also incorporate human experience and more simulation results.

Thus, it can be concluded that an integrated near real time monitoring and hydrodynamic modelling approach, as depicted in this study, with suitable inputs and boundary conditions could be used to plan various river training works. Such an approach will aid in effective sustainable management of large dynamic rivers like the Brahmaputra and the Ganga.

5.3 Future scope

The aim of this thesis is to develop an integrated hydro-ecological monitoring system for near real time management of water resources. To understand the physics behind the nutrient exchange mechanisms observed between the river and the riparian vegetation zones, a three dimensional hydrodynamic model was setup. There are three potential avenues for further research:

1. An integrated near real time hydro-ecological monitoring and modelling framework can be developed. Data from the field can be used to generate an *ANN* model connecting Normalised Difference Turbidity Index (*NDTI*) to sediment discharge. Using another *ANN* model developed with hydrodynamic model simulations, sediment discharge may be connected to discharge (Lane, 1955). River training works can also be simulated using *ANN* models for velocity fields, flow depths, and bathymetry. These *ANN* models can be merged into a Convolutional Neural Networks (*CNN*) model to forecast river training works' ecological response using the web-*GIS* application developed in this study. Further, optimisation principles can be incorporated to enable cost-benefit analysis for groyne fields (Kalita et al., 2014). Advanced Neural Network-based techniques can then be utilised to construct efficiency prediction models (Zhao et al., 2019a), service life prediction models (Zhao et al., 2019b), and energy dissipation evaluation models (Zhao et al., 2019c) for these river training works.

2. This study used *LANDSAT 8* and *Sentinel 2* imageries to generate maps of aquatic (*NDCI*) and terrestrial (*EVI, GNDVI, NDVI*) ecological parameters. There are several other ecological parameters, that can be estimated with various other sensors (Table 5.1). Exploring these parameters using various sensors will lead to a better understanding of the ecological interactions, due to increased evidence and more frequent observations as a result of increased temporal coverage.

3. The response of various species of vegetation on river water quality can be studied. This can be done by considering homogeneous patches in experiments/field and analyzing the resulting nutrient exchanges.

4. Advanced underwater drone technologies can be utilised to obtain concurrent field measurements. These measurements can be combined with satellite measurements to enhance the precision of estimations and to account for data gaps during the intervals between satellite passes.

Table 5.1: Water quality parameters estimation using remote sensing (Gholizadeh et al., 2016)

Parameter	Band combination	Sensor
Chlorophyll-a	$\frac{Green}{Red}$	LANDSAT 5 TM LANDSAT 5 MSS LANDSAT 7 ETM + SPOT IRS LISS III
	$\frac{NIR}{Red}$	LANDSAT 5 TM HICO PROBA-CHRIS MODIS MERIS AISA
	$\frac{Green}{Blue}$	LANDSAT 5 TM LANDSAT 7 ETM + MERIS PROBA-CHRIS EO-1 Hyperion
	$\frac{Blue}{Red}$	LANDSAT 5 TM LANDSAT 7 ETM +
	Blue	LANDSAT 5 TM
	Red	PROBA-CHRIS LANDSAT 5 TM CASI
	Green	LANDSAT 5 TM Daedalus Airborne-Thematic Mapper (ATM)
Colored dissolved Organic Matter (CDOM)	*Blue*	LANDSAT 5 TM EO-1 Hyperion SeaWIFS + MODIS-Aqua MODIS SeaWIFS HICO CZCS
	$\frac{Blue}{Green}$	ALOS AVNIR 2 MODIS SeaWIFS

	$\frac{Green}{Red}$	MODIS HICO EO-1 ALI EO-1 Hyperion SeaWIFS MERIS
Secchi disk depth	$\frac{Blue}{Green}$	LANDSAT 5 TM LANDSAT 5 MSS LANDSAT 7 ETM + ASTER and ETM +
	$\frac{Blue}{Red}$	LANDSAT 5 TM LANDSAT 5 MSS PROBA-CHRIS IKONOS
	$\frac{Green}{Red}$	LANDSAT 5 TM ALOS AVNIR-2 SPOT
	$Blue$	LANDSAT 5 TM MODIS
	Red	LANDSAT 5 TM
	$Green$	LANDSAT 5 MSS MODIS
Turbidity/ Total Suspended Solids	$\frac{Green}{Red}$	LANDSAT 5 TM PROBA-CHRIS IRS LISS III
	$\frac{Blue}{Red}$	LANDSAT 5 TM AISA
	$\frac{NIR}{Red}$	MODIS ALOS AVNIR-2
	NIR	SPOT LANDSAT 7 ETM + CASI
	Red	LANDSAT 7 ETM + LANDSAT 5 TM HICO PROBA-CHRIS
	$Green$	LANDSAT 5 MSS IRS LISS III

Total Phosphorous	*Blue*, *Green*/ *Red*, *Green*	LANDSAT 5 TM MODIS PROBA-CHRIS CASI SPOT
Water Temperature	*Thermal infrared*	TM ETM + OLI/ TIRS MODIS ASTER AVHRR Airborne-MODIS/ ASTER (MASTER)
	Microwave	Microwave Radiometers (MWRs)
Sea surface salinity		European Soil Moisture and- Ocean Salinity (SMOS) Aquarius L band radiometer on SAC-D SLFMR STARRS Other MWRs experiences Predicted indirectly with- salinity and temperature Predicted indirectly with- salinity and CDOM
Dissolved-Oxygen (DO), Biochemical-Oxygen-Demand (BOD), and Chemical-Oxygen-Demand (COD)		Landsat 5 TM Landsat 5 MSS WorldView-2 IRS LISS III MODIS MERIS AVHRR SeaWIFS SPOT

Appendix A: Google Earth Engine

https://earthengine.google.com/

Contents

A.1 Introduction

Google Earth Engine (*GEE*) is a cloud-based geospatial platform developed by Google that provides a suite of tools for satellite imagery analysis and geospatial data visualization. One of the key features of *GEE* is its ability to process and analyze large amounts of satellite imagery quickly and efficiently. It provides access to a wide range of satellite imagery (`https://developers.google.com/earth-engine/datasets`), including *LANDSAT*, *Sentinel-2*, and *MODIS*, among others. Users can access and analyze petabytes of data with a few lines of code, which makes it possible to analyze large-scale environmental changes, such as deforestation, land use/land cover changes, and monitor them in near real time. This makes *GEE* an essential tool for researchers and organizations that need to monitor and analyze environmental changes on a global scale.

Another significant benefit of *GEE* is its integration with other Google tools, such as *Google Drive* and *Google Cloud Storage*. This integration makes it easy to store and manage large datasets, collaborate with others, and share data-*cum*-analysis results with a broader audience. Furthermore, it provides an easy-to-use application programming interface (*API*) that allows users to access and analyze data using popular programming languages such as *Python* and *JavaScript*. This makes it easy for developers and data scientists to use and integrate it into their workflows.

GEE has many applications in various industries, including agriculture, forestry, urban planning, and environmental monitoring. In the agriculture industry, it is used to monitor crop growth, assess crop yield, and predict crop performance using machine learning algorithms. In the forestry industry, it is used to monitor forest cover, assess deforestation rates, and predict forest fires. In the urban planning industry, it is used to assess urbanization rates, identify areas of urban growth, and plan for sustainable urban development. In the environmental monitoring industry, it is used to monitor air and water quality, assess the impact of climate change, and study the spread of diseases.

A.2 Google Earth Engine Apps

GEE Apps (`https://www.earthengine.app/`) is a platform within *GEE* that allows developers and data scientists to create and deploy custom web applications that leverage the power of *GEE*. These apps provide users with interactive visualizations and analysis tools that allow them to explore and understand geospatial data in a more intuitive and engaging way. It provides a range of features and tools that make it easy to create custom web applications. These include templates for common use cases, such as monitoring land use or tracking changes in vegetation cover, as well as a powerful *JavaScript API* that allows developers to customize the functionality and appearance of their apps. In addition to its ease of use and customization options, *GEE Apps* also provides powerful data processing capabilities. Apps can access and analyze petabytes of geospatial data stored in the *GEE*, allowing users to perform complex analysis and modelling tasks directly within the app. This makes it easier to share data and insights with others and can lead to more informed decision-making.

The link to the demonstration of the application developed in this thesis can be found below:

https://youtu.be/LAlIx9OlDdY

Appendix B: OpenFOAM Hydrodynamic Model

https://www.openfoam.com/

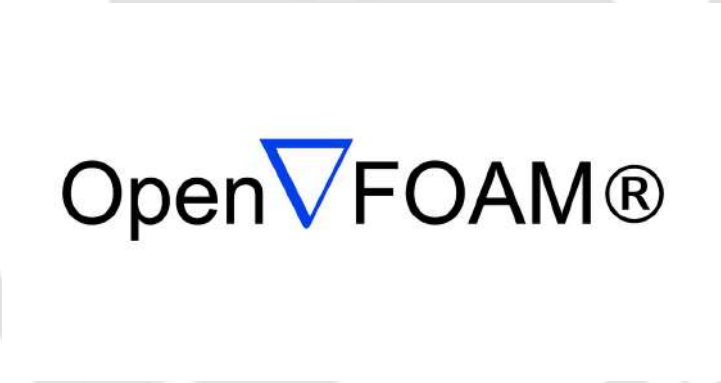

Contents

B.1 Introduction

OpenFOAM (Open Field Operation and Manipulation) is a free, open-source software package for computational fluid dynamics (*CFD*) simulation. It was first released in 2004 by the OpenCFD Ltd., which is a UK-based company. It is free to download and use, which makes it accessible to a wide range of users, including researchers, engineers, and students. Furthermore, because it is open-source, users can modify the code and share their modifications with the community. This promotes collaboration and innovation, which ultimately leads to better software and more accurate simulations. Since its inception, *OpenFOAM* has become one of the most widely used *CFD* software in various industries, including automotive, aerospace, energy, and environmental engineering. It is written in C++ programming language and uses object-oriented programming (*OOP*) concepts.

One of the main features of *OpenFOAM* is its flexibility. *OpenFOAM* allows users to modify or extend the code to suit their specific needs. Users can add their own models, solvers, boundary conditions, and post-processing tools. This makes *OpenFOAM* highly adaptable and suitable for a wide range of applications. Another advantage of *OpenFOAM* is its robustness. *OpenFOAM* is also highly scalable, meaning that it can run on a single workstation or on a high-performance computing cluster. *OpenFOAM* supports a wide range of solvers for different types of fluid flow problems. These include laminar and turbulent flows, compressible and incompressible flows, and multiphase flows. In addition to the $\kappa - \omega$ turbulence model used in this study, it also supports a variety of turbulence models, such as the Reynolds-averaged Navier-Stokes (*RANS*) models, the large eddy simulation (*LES*) models, $\kappa - \varepsilon$ models, and the detached eddy simulation (*DES*) models. This enables users to simulate complex fluid flow problems accurately and efficiently.

OpenFOAM has many applications in various industries. In the automotive industry, it is used to simulate the aerodynamics of cars and to optimize their design for better fuel efficiency and performance. In the aerospace industry, it is used to simulate the airflow around aircraft and to optimize their design for better lift and drag characteristics. In the energy industry, it is used to simulate the flow of fluids in oil and gas reservoirs and to optimize the extraction of oil and gas. In the environmental engineering industry, it is used to simulate the flow of water in rivers and oceans and to study the effects of pollution on aquatic life. More details on the model can be found in the following link:

https://openfoam.org

B.2 Data processing and analysis using Python

Python (`https://www.python.org/`) is a popular programming language that is widely used in the field of data science and data analysis. One of the main reasons for its popularity is its ability to handle large amounts of data and perform complex analysis using various libraries and modules. One such module is *matplotlib* (`https://matplotlib.org/`), which is a data visualization library that provides a wide range of tools for creating high-quality graphs, charts, and visualizations. It can be used for various data visualization tasks, such as plotting time series data, creating scatter plots, and generating histograms. It can also be used to create more advanced visualizations, such as heat maps and 3D plots. One of the main advantages of using *matplotlib* is its flexibility and customization options, which allow users to create customized visualizations tailored to their specific needs.

In addition *Python* also provides other modules such as *Pandas* (`https://pandas.pydata.org/`) and *NumPy* (`https://numpy.org/`) that are essential for data processing and analysis. *Pandas* is a data manipulation library that provides tools for data cleaning, filtering, and merging, while *NumPy* is a numerical computation library that provides tools for performing mathematical operations on arrays. Together, these modules provide a powerful toolkit for data processing and analysis in *Python*.

Bibliography

Aamir, M. and Sharma, N. (2015). Riverbank protection with porcupine systems: development of rational design methodology. *ISH Journal of Hydraulic Engineering*, 21(3):317– 332.

Adams, J. B. and Gillespie, A. R. (2006). *Remote Sensing of Landscapes with Spectral images: A Physical Modeling Approach*. Cambridge University Press, New York, USA.

Ahern, F., Goodenough, D., Jain, S., Rao, V., and Rochon, G. (1977). Use of clear lake as standard reflectors for atmospheric measurement. In *ERIM Proc. of the 11th Intern. Symp. on Remote Sensing of Environment*, volume 1, page 731–775.

Akter, A., Crapper, M., Pender, G., Wright, G., and Wong, W. (2012). Modelling the failure modes in geobag revetments. *Water Science and Technology: a Journal of the International Association on Water Pollution Research*, 65:418–425.

Ardalan, H. and Vafaei, F. (2019). CFD and experimental study of 45° inclined thermal- saline reversible buoyant jets in stationary ambient. *Environmental Processes*, 6:219–239.

Ashmore, P. (2013). Morphology and dynamics of braided rivers. *Treatise on Geomorphology*, 9:289–312.

Balla, D., Zichar, M., Kiss, E., Szabó, G., and Mester, T. (2022). Possibilities for assessment and geovisualization of spatial and temporal water quality data using a webGIS application. *International Society for Photogrammetry and Remote Sensing: International Journal of Geo-Information*, 11(2).

Bejarano, F. T., Hernández, F. A., Ibarra, D. R., Avila, D. M., and Márquez, L. M. (2020). Water quality assessment in a wetland complex using Sentinel 2 satellite images water quality assessment in a wetland complex using Sentinel 2 satellite images. *International Journal of Environmental Science and Technology*, 18:2345–2356.

Bhattacharjee, R., Gupta, A., Das, N., Agnihotri, A. K., Ohri, A., and Gaur, S. (2022). Analysis of algal bloom intensification in mid- Ganga river, India using satellite data and neural network techniques. *Environmental Monitoring and Assessment*, 194:1– 20.

Borah, J., Ahmed, M. F., Sarma, P. K., et al. (2010). Brahmaputra river islands as potential corridors for dispersing tigers: A case study from Assam, India. *International Journal of Biodiversity and Conservation*, 2(11):350–358.

Breiman, L. (2001). Random forests. *Machine learning*, 45:5– 32.

Bresciani, M., Giardino, C., Longhi, D., Pinardi, M., Bartoli, M., and Vascellari, M. (2009). Imaging spectrometry of productive inland waters. application to the lakes of Mantua. *Italian Journal of Remote Sensing*, 41(2):147–156.

Brivio, P., Giardino, C., and Zilioli, E. (2001). Determination of chlorophyll concentration changes in lake Garda using an image- based radiative transfer code for LANDSAT TM images. *International Journal of Remote Sensing*, 22(2- 3):487–502.

Burtenshaw, J. C., Oleson, E. M., Hildebrand, J. A., McDonald, M. A., Andrew, R. K., Howe, B. M., and Mercer, J. A. (2004). Acoustic and satellite remote sensing of blue whale seasonality and habitat in the Northeast Pacific. *Deep Sea Research Part II: Topical Studies in Oceanography*, 51(10-11):967–986.

Chang, H. (1998). *Fluvial Processes in River Engineering*. Krieger Publishing Company.

Chavez, P. S. et al. (1996). Image- based atmospheric corrections- revisited and improved. *Photogrammetric Engineering and Remote Sensing*, 62(9):1025–1035.

Chavez Jr, P. S. (1988). An improved dark- object subtraction technique for atmospheric scattering correction of multispectral data. *Remote Sensing of Environment*, 24(3):459–479.

Chembolu, V. and Dutta, S. (2018). An entropy based morphological variability assessment of a large braided river. *Earth Surface Processes and Landforms*, 43:2889–2896.

Chembolu, V., Kakati, R., and Dutta, S. (2019). A laboratory study of flow characteristics in natural heterogeneous vegetation patches under submerged conditions. *Advances in Water Resources*, 133:1–13.

Chowdhury, M. E., Hossain, A., and Muktadir, H. (2018). Evaluation of the river training work of Padma river through a mathematical approach. *Journal of Modern Science and Technology*, 6:25–62.

Das, B. (2018). Numerical method to compute water surface profile for converging compound channel. *Arabian Journal for Science and Engineering*, 43:5349–5364.

Das, N., Bhattacharjee, R., Choubey, A., Agnihotri, A. K., Ohri, A., and Gaur, S. (2022). Analysing the change in water quality parameters along river Ganga at Varanasi, Mirzapur and Ghazipur using Sentinel- 2 and LANDSAT-8 satellite data during pre- lockdown, lockdown and post- lockdown associated with COVID- 19. *Journal of Earth System Science*, 131:1–28.

Devi, T. B., Daga, R., Mahto, S. K., and Kumar, B. (2016). Drag and turbulent characteristics of mobile bed channel with mixed vegetation densities under downward seepage. *Journal of Fluids Engineering*, 138(7):1–13.

Devi, T. B. and Kumar, B. (2015). Turbulent flow statistics of vegetative channel with seepage. *Journal of Applied Geophysics*, 123:267–276.

Ding, H., Shi, J., Wang, Y., and Wei, L. (2015). An improved dark- object subtraction technique for atmospheric correction of LANDSAT 8. In *MIPPR 2015: Remote Sensing Image Processing, Geographic Information Systems, and Other Applications*, volume 9815, pages 128– 135. Society of Photographic Instrumentation Engineers.

Dozier, J. and Frew, J. (1981). Atmospheric corrections to satellite radiometric data over rugged terrain. *Remote Sensing of Environment*, 11:191– 205.

Duan, J. G., He, L., Fu, X., and Wang, Q. (2009). Mean flow and turbulence around experimental spur dike. *Advances in Water Resources*, 32(12):1717–1725.

Dubey, A. K., Gupta, P., Dutta, S., and Kumar, B. (2014). Evaluation of satellite- altimetry- derived river stage variation for the braided Brahmaputra river. *International Journal of Remote Sensing*, 35(23):7815– 7827.

Dwivedi, S., Mishra, S., and Tripathi, R. D. (2018). Ganga water pollution: A potential health threat to inhabitants of Ganga basin. *Environment International*, 117:327– 338.

Flynn, R. (2016). *Holy Literary License: The Almighty Publisher Chooses Fallible Mortals to Write, Edit, Select, Reject, Copy, and Translate Godstory*. Wings Press.

Franz, B. A., Bailey, S. W., Kuring, N., and Werdell, P. J. (2015). Ocean color measurements with the operational land imager on LANDSAT- 8: implementation and evaluation in SeaDAS. *Journal of Applied Remote Sensing*, 9(1):1–16.

Gao, J. (2009). *Digital Analysis of Remotely Sensed Imagery*. McGraw Hill LLC.

George, D. (1997). The airborne remote sensing of phytoplankton chlorophyll in the lakes and tarns of the English Lake District. *International Journal of Remote Sensing*, 18(9):1961– 1975.

Gholizadeh, M. H., Melesse, A. M., and Reddi, L. (2016). A comprehensive review on water quality parameters estimation using remote sensing techniques. *Sensors*, 16(8):1–43.

Gilja, G., Kuspilić, N., and Golubović, N. (2019). Impact of river training works on the Drava river flow regime. In *16th International symposium Water management & hydraulic engineering*, pages 89–99.

Gitelson, A. (1992). The peak near 700 nm on radiance spectra of algae and water: relationships of its magnitude and position with chlorophyll concentration. *International Journal of Remote Sensing*, 13(17):3367– 3373.

Gitelson, A., Garbuzov, G., Szilagyi, F., Mittenzwey, K., Karnieli, A., and Kaiser, A. (1993). Quantitative remote sensing methods for real-time monitoring of inland waters quality. *International Journal of Remote Sensing*, 14(7):1269– 1295.

Gitelson, A. A., Dall'Olmo, G., Moses, W., Rundquist, D. C., Barrow, T., Fisher, T. R., Gurlin, D., and Holz, J. (2008). A simple semi- analytical model for remote estimation of chlorophyll- a in turbid waters: Validation. *Remote Sensing of Environment*, 112(9):3582– 3593.

Gitelson, A. A., Kaufman, Y. J., and Merzlyak, M. N. (1996). Use of a green channel in remote sensing of global vegetation from EOS-MODIS. *Remote Sensing of Environment*, 58(3):289– 298.

Golombek, N. Y., Scheingross, J. S., Repasch, M. N., Hovius, N., Menges, J., Sachse, D., Lupker, M., Eglinton, T. I., Haghipour, N., Poulson, S. R., Gröcke, D. R., Latosinski, F. G., and Szupiany, R. N. (2021). Fluvial organic carbon composition regulated by seasonal variability in lowland river migration and water discharge. *Geophysical Research Letters*, 48(24):e2021GL093416. e2021GL093416 2021GL093416.

Gorelick, N., Hancher, M., Dixon, M., Ilyushchenko, S., Thau, D., and Moore, R. (2017). Google Earth Engine: Planetary- scale geospatial analysis for everyone. *Remote Sensing of Environment*, 202:18–27. Big Remotely Sensed Data: tools, applications and experiences.

Goring, D. and Nikora, V. (2002). Despiking acoustic doppler velocimeter data. *Journal of Hydraulic Engineering-American Society of Civil Engineers*, 128:117–126.

Goswami, D. C. (1985). Brahmaputra river, Assam, India: Physiography, basin denudation, and channel aggradation. *Water Resources Research*, 21(7):959–978.

Gu, Z., Cao, X., Jiao, Y., and Lu, W.-Z. (2016). Appropriate CFD models for simulating flow around spur dike group along urban riverways. *Water Resources Management*, 30:4559–4570.

Ha, N. T. T., Thao, N. T. P., Koike, K., and Nhuan, M. T. (2017). Selecting the best band ratio to estimate chlorophyll- a concentration in a tropical freshwater lake using Sentinel 2A images from a case study of lake Ba Be (Northern Vietnam). *ISPRS International Journal of Geo- Information*, 6(9).

Hadjimitsis, D., Papadavid, G., Agapiou, A., Themistocleous, K., Hadjimitsis, M., Retalis, A., Michaelides, S., Chrysoulakis, N., Toulios, L., and Clayton, C. (2010). Atmospheric correction for satellite remotely sensed data intended for agricultural applications: Impact on vegetation indices. *Natural Hazards and Earth System Sciences*, 10:89–95.

Han, L. and Rundquist, D. C. (1997). Comparison of NIR/red ratio and first derivative of reflectance in estimating algal-chlorophyll concentration: A case study in a turbid reservoir. *Remote Sensing of Environment*, 62(3):253– 261.

Hedger, R. D., Olsen, N. R., Malthus, T. J., and Atkinson, P. M. (2002). Coupling remote sensing with computational fluid dynamics modelling to estimate lake chlorophyll-a concentration. *Remote Sensing of Environment*, 79(1):116– 122.

Hestir, E. L., Brando, V. E., Bresciani, M., Giardino, C., Matta, E., Villa, P., and Dekker, A. G. (2015). Measuring freshwater aquatic ecosystems: The need for a hyperspectral global mapping satellite mission. *Remote Sensing of Environment*, 167:181– 195.

Hossain, M. (2016). Performance comparison between geo- bag and cement concrete block in river bank protection works. *International Journal of Engineering Technology, Management and Applied Sciences*, 4:56– 61.

Huete, A., Justice, C., and Van Leeuwen, W. (1999). *MODIS Vegetation Index (MOD13)*. University of Arizona.

Hunter, P. D., Tyler, A. N., Présing, M., Kovács, A. W., and Preston, T. (2008). Spectral discrimination of phytoplankton colour groups: The effect of suspended particulate matter and sensor spectral resolution. *Remote Sensing of Environment*, 112(4):1527–1544.

Järvelä, J. (2002). Flow resistance of flexible and stiff vegetation: a flume study with natural plants. *Journal of hydrology*, 269(1-2):44–54.

Järvelä, J. (2005). Effect of submerged flexible vegetation on flow structure and resistance. *Journal of Hydrology*, 307(1-4):233–241.

Jennifer, D., Li, H., Guangqian, W., and Xudong, F. (2011). Turbulent burst around experimental spur dike. *International Journal of Sediment Research*, 26(4):471– 523.

Jia, Y. and Wang, S. S. Y. (1999). Numerical model for channel flow and morphological change studies. *Journal of Hydraulic Engineering*, 125:924–933.

Jing, P., Tamai, N., and Kawahara, Y. (2002). Numerical modelling of local scour around spur dikes. *J. of Sediment Research*, 1:25–29.

Julien, P. (2018). *River Mechanics*. Cambridge University Press, United Kingdom.

Jutla, A. S., Akanda, A. S., Griffiths, J. K., Colwell, R., and Islam, S. (2011). Warming oceans, phytoplankton, and river discharge: implications for cholera outbreaks. *The American Journal of Tropical Medicine and Hygiene*, 85(2):303–308.

Kalita, H. (2020). A numerical model for 1D bed morphology calculations. *Water Resources Management*, 34:4975– 4989.

Kalita, H., Sarma, A., and Bhattacharjya, R. (2014). Evaluation of optimal river training work using GA based linked simulation- optimization approach. *Water Resources Management*, 28:2077– 2092.

Kar, S., Rathore, V., Sharma, R., Swain, S., et al. (2016). Classification of river water pollution using Hyperion data. *Journal of Hydrology*, 537:221–233.

Karaska, M. A., Huguenin, R. L., Beacham, J. L., Wang, M.-H., Jensen, J. R., and Kaufmann, R. S. (2004). AVIRIS measurements of chlorophyll, suspended minerals, dissolved organic carbon, and turbidity in the Neuse River, North Carolina. *Photogrammetric Engineering & Remote Sensing*, 70(1):125–133.

Karmaker, T. and Dutta, S. (2011). Erodibility of fine soil from the composite river bank of Brahmaputra in India. *Hydrological Processes*, 25:104–111.

Karmaker, T. and Dutta, S. (2013). Modelling seepage erosion and bank retreat in a composite river bank. *Journal of Hydrology*, 476:178–187.

Karmaker, T. and Dutta, S. (2016). Prediction of short- term morphological change in large braided river using 2D numerical model. *Journal of Hydraulic Engineering*, 142:1–13.

Kemmerer, A. J. and Butler, J. A. (1977). Finding fish with satellites. *Marine Fisheries Review*, 39(1):16–21.

Khan, M. N. and Mohammad, F. (2014). *Eutrophication: Challenges and Solutions*, pages 1– 15. Springer Netherlands, Dordrecht.

Kidova, A., Radecki-Pawlik, A., Rusnák, M., and Plesiński, K. (2021). Hydromorphological evaluation of the river training impact on a multi- thread river system (Belá River, Carpathians, Slovakia). *Scientific Reports*, 11:1–18.

Klemas, V. (2012). Remote sensing of environmental indicators of potential fish aggregation: An overview. *Baltica*, 25(2):99–112.

Kneizys, F. X. (1988). *Users guide to LOWTRAN 7*. Air Force Geophysics Laboratory.

Kobara, S. and Heyman, W. D. (2007). Caribbean- wide geospatial analysis of the location of transient reef fish spawning aggregation sites using remote sensing. *Proceedings of Gulf Caribbean Fish Institute*, 59:463–466.

Kocaer, O. and Yarar, A. (2020). Experimental and numerical investigation of flow over ogee spillway. *Water Resources Management*, 34:3949–3965.

Kotoky, P., Bezbaruah, D., Baruah, J., and Sarma, J. (2003). Erosion activity on Majuli: the largest river island of the world. *Current Science*, 84(7):929–932.

Kriegler, F. J., Malila, W. A., Nalepka, R. F., and Richardson, W. (1969). Preprocessing transformations and their effects on multispectral recognition. In *Remote Sensing of Environment*, pages 97–131.

Kuhn, C., de Matos Valerio, A., Ward, N., Loken, L., Sawakuchi, H. O., Kampel, M., Richey, J., Stadler, P., Crawford, J., Striegl, R., Vermote, E., Pahlevan, N., and Butman, D. (2019). Performance of LANDSAT- 8 and Sentinel- 2 surface reflectance products for river remote sensing retrievals of chlorophyll- a and turbidity. *Remote Sensing of Environment*, 224:104–118.

Lane, E. W. (1955). Preprocessing transformations and their effects on multispectral recognition. In *Proceedings of the American Society of Civil Engineers*, pages 1–17.

Launder, B. and Spalding, D. (1974). The numerical computation of turbulent flows. *Computer Methods in Applied Mechanics and Engineering*, 3(2):269–289.

Li, Y., Mi, W., Ji, L., He, Q., Yang, P., Xie, S., and Bi, Y. (2023). Urbanization and agriculture intensification jointly enlarge the spatial inequality of river water quality. *Science of the Total Environment*, 878:1–10.

Li, Z., Duan, P., Hu, S., Li, M., and Kang, X. (2022). Fast hyperspectral image dehazing with dark-object subtraction model. *IEEE Geoscience and Remote Sensing Letters*, 19:1–5.

Lillesand, T., Kiefer, R., and Chipman, J. (2015). *Remote Sensing and Image Interpretation*. Wiley.

lin Tang, X., Ding, X., and cong Chen, Z. (2007). Experimental and numerical investigations on secondary flows and sedimentations behind a spur dike. *Journal of Hydrodynamics*, 19(1):23–29.

Liu, H., He, X., Li, Q., Hu, X., Ishizaka, J., Kratzer, S., Yang, C., Shi, T., Hu, S., Zhou, Q., et al. (2021). Evaluation of ocean color atmospheric correction methods for Sentinel- 3 OLCI using global automatic in situ observations. *IEEE Transactions on Geoscience and Remote Sensing*, 60:1–19.

Mali, V., Veeranna, B., Parik, A., and Kuiry, S. (2020). Experimental and numerical study of flood dynamics in a river-network-floodplain set-up. *Journal of Hydroinformatics*, 22:793–814.

Markovic Brankovic, J., Markovic, M., and Kostic, A. (2021). A natural approach to river engineering practice. a case study of the Ljiljanska river. *Facta Universitatis- Series: Architecture and Civil Engineering*, 19:305–313.

Mayerle, R., Wang, S. S. Y., and Toro, F. M. (1995). Verification of a three-dimensional numerical model simulation of the flow in the vicinity of spur dikes. *Journal of Hydraulic Research*, 33(2):243–256.

Meena, S., Bhuyan, K., Chauhan, A., and Singh, R. (2021). Changes in the flood plains and water quality along the Himalayan rivers after the Chamoli disaster of 7 February 2021. *International Journal of Remote Sensing*, 42:6984– 7001.

Menter, F. (1993). Zonal two equation $\kappa-\omega$ turbulence models for aerodynamic flows. In *23rd Fluid Dynamics, Plasmadynamics, and Lasers Conference*, volume 2906, pages 1–7.

Menter, F. R. (1994). Two-equation eddy-viscosity turbulence models for engineering applications. *American Institute of Aeronautics and Astronautics Journal*, 32:1598–1605.

Mishra, S. and Mishra, D. R. (2012). Normalized difference chlorophyll index: A novel model for remote estimation of chlorophyll- a concentration in turbid productive waters. *Remote Sensing of Environment*, 117:394–406.

Modalavalasa, S., Chembolu, V., Dutta, S., and Kulkarni, V. (2023). Laboratory investigation on flow structure and turbulent characteristics in low sinuous compound channels with vegetated floodplains. *Journal of Hydrology*, 618:1–13.

Mohapatra, P. K. (2006). Mathematical modelling of scour around a bridge pier. In *Proceedings of The Seventh International Conference on HydroScience and Engineering, Michael Piasecki and College of Engineering, Drexel University.*

Molls, T., Hanif Chaudhry, M., and Wasey Khan, K. (1995). Numerical simulation of two- dimensional flow near a spur- dike. *Advances in Water Resources*, 18(4):227–236.

Moran, M. S., Jackson, R. D., Slater, P. N., and Teillet, P. M. (1992). Evaluation of simplified procedures for retrieval of land surface reflectance factors from satellite sensor output. *Remote Sensing of Environment*, 41(2-3):169–184.

Mustak, S. (2013). Correction of atmospheric haze in Resourcesat- 1 LISS- 4 MX data for urban analysis: an improved dark object subtraction approach. *International Archives of the Photogrammetry, Remote Sensing and Spatial Information Sciences*, 1:283–287.

Naik, B., Khatua, K. K., Wright, N., Sleigh, A., and Singh, P. (2018). Numerical modelling of converging compound channel flow. *Indian Society for Hydraulics Journal of Hydraulic Engineering*, 24(3):285–297.

Nandi, K. K., Pradhan, C., Dutta, S., and Khatua, K. K. (2022). How dynamic is the Brahmaputra? Understanding the process- form- vegetation interactions for hierarchies of energy dissipation. *Ecohydrology*, 15(3):1–16.

Neysiani, S. N., Roozbahani, A., Javadi, S., and Shahdany, S. M. H. (2022). Water resources assessment of Zayandeh-Rood river basin using integrated surface water and groundwater footprints and K- means clustering method. *Journal of Hydrology*, 614:1–15.

Nurdin, S., Mustapha, M. A., Lihan, T., and Zainuddin, M. (2017). Applicability of remote sensing oceanographic data in the detection of potential fishing grounds of Rastrelliger kanagurta in the archipelagic waters of Spermonde, Indonesia. *Fisheries Research*, 196:1–12.

Oberhagemann, K. (2011). Geotextile bag revetments for large rivers in Bangladesh. *Geotextiles and Geomembranes*, 29:402–414.

Oberhagemann, K., Haque, A., and Thompson, A. (2020). A century of riverbank protection and river training in Bangladesh. *Water*, 12:1–30.

Olmanson, L. G., Brezonik, P. L., and Bauer, M. E. (2013). Airborne hyperspectral remote sensing to assess spatial distribution of water quality characteristics in large rivers: The Mississippi river and its tributaries in Minnesota. *Remote Sensing of Environment*, 130:254– 265.

Ortiz, A. C., Ashton, A., and Nepf, H. (2013). Mean and turbulent velocity fields near rigid and flexible plants and the implications for deposition. *Journal of Geophysical Research: Earth Surface*, 118(4):2585–2599.

Otterman, J. and Fraser, R. (1976). Earth-atmosphere system and surface reflectivities in arid regions from LANDSAT MSS data. *Remote Sensing of Environment*, 5:247–266.

Page, B. P., Kumar, A., and Mishra, D. R. (2018). A novel cross-satellite based assessment of the spatio-temporal development of a cyanobacterial harmful algal bloom. *International Journal of Applied Earth Observation and Geoinformation*, 66:69–81.

Patankar, S. V. and Spalding, D. B. (1972). A calculation procedure for heat, mass and momentum transfer in three-dimensional parabolic flows. *International Journal of Heat and Mass Transfer*, 15:1787–1806.

Phinn, S., Roelfsema, C., Dekker, A., Brando, V., and Anstee, J. (2008). Mapping seagrass species, cover and biomass in shallow waters: An assessment of satellite multi-spectral and airborne hyper-spectral imaging systems in Moreton Bay (Australia). *Remote Sensing of Environment*, 112(8):3413–3425.

Picco, L., Mao, L., Cavalli, M., Buzzi, E., Rainato, R., and Lenzi, M. (2013). Evaluating short-term morphological changes in a gravel-bed braided river using terrestrial laser scanner. *Geomorphology*, 201:323–334.

Pradhan, C., Chembolu, V., and Dutta, S. (2019). Impact of river interventions on alluvial channel morphology. *Indian Society for Hydraulics Journal of Hydraulic Engineering*, 25(1):87–93.

Pradhan, C., Padhee, S., Bharti, R., and Dutta, S. (2022). A process- based recovery indicator for anthropogenically disturbed river system. *Scientific Reports*, 12(1):1–14.

Pradhan, N. S., Das, P. J., Gupta, N., and Shrestha, A. B. (2021). Sustainable management options for healthy rivers in South Asia: The case of Brahmaputra. *Sustainability*, 13(3):1–23.

Prasad, S., Saluja, R., and Garg, J. K. (2020). Assessing the efficacy of LANDSAT- 8 OLI imagery derived models for remotely estimating chlorophyll- a concentration in the upper Ganga river, india. *International Journal of Remote Sensing*, 41(7):2439–2456.

Principal Accountant General, Indian Audit and Accounts Department (2011). Report of 2011. In *Audit Report (Civil) of the Comptroller and Auditor General of India for the ended 31 March 2011 Government of Assam*. Comptroller and Auditor General of India.

Rahman, L. and Osman, S. (2015). River bank erosion protection using bamboo bandalling structure: a case study. *Journal of Civil Engineering*, 43(1):1– 8.

Ramezani, M., Abessi, O., and Firoozjaee, A. R. (2021). Effect of proximity to bed on 30° and 45° inclined dense jets: a numerical study. *Environmental Processes*, 8:1141–1164.

Reese, D. C., O'Malley, R. T., Brodeur, R. D., and Churnside, J. H. (2011). Epipelagic fish distributions in relation to thermal fronts in a coastal upwelling system using high- resolution remote- sensing techniques. *International Council for the Exploration of the Sea Journal of Marine Science*, 68(9):1865–1874.

Richter, R. (1990). A fast atmospheric correction algorithm applied to LANDSAT TM images. *Remote Sensing*, 11(1):159–166.

Rowan, L. C., Wetlaufer, P. H., Goetz, A.F.H. Billingsley, F., and Stewart, J. H. (1976). Discrimination of rock types and detection of hydrothermally altered areas in South-Central Nevada by the use of computer-enhanced ERTS images. *United States Geological Survey Professional Paper*, 883:1–35.

Sarker, M. H., Akter, J., and Ruknul, M. (2011). River bank protection measures in the Brahmaputra- Jamuna river: Bangladesh experience. In *International Seminar on River, Society and Sustainable Development, Dibrugarh University, India*, volume 121, pages 1–14.

Shafique, N. A., Fulk, F., Autrey, B. C., Flotemersch, J., et al. (2003). Hyperspectral remote sensing of water quality parameters for large rivers in the Ohio river basin. In *First Interagency Conference on Research in the Watershed, Benson, AZ*, pages 216–221. Citeseer.

Shucksmith, J., Boxall, J., and Guymer, I. (2010). Effects of emergent and submerged natural vegetation on longitudinal mixing in open channel flow. *Water Resources Research*, 46(4):1–14.

Singh, S. (1988). Estimation of multiple reflection and lowest order adjacency effects on remotely-sensed data. *International Journal of Remote Sensing*, 9(9):1433–1450.

Susuman, A. S., Lougue, S., and Battala, M. (2016). Female literacy, fertility decline and life expectancy in Kerala, India: an analysis from Census of India 2011. *Journal of Asian and African Studies*, 51(1):32–42.

Szabo, S., Gácsi, Z., and Bertalan-Balazs, B. (2016). Specific features of NDVI, NDWI and MNDWI as reflected in land cover categories. *Landscape and Environment*, 10:194–202.

Tamminga, A., Hugenholtz, C., Eaton, B., and Lapointe, M. (2015). Hyperspatial remote sensing of channel reach morphology and hydraulic fish habitat using an unmanned aerial vehicle (UAV): A first assessment in the context of river research and management. *River Research and Applications*, 31(3):379–391.

Taormina, R. and Chau, K.-W. (2015). Data-driven input variable selection for rainfall-runoff modelling using binary-coded particle swarm optimization and extreme learning machines. *Journal of Hydrology*, 529:1617– 1632.

Teillet, P. and Fedosejevs, G. (1995). On the dark target approach to atmospheric correction of remotely sensed data. *Canadian Journal of Remote Sensing*, 21(4):374–387.

Teraguchi, H., Nakagawa, H., Kawaike, K., Baba, Y., and Zhang, H. (2010). Morphological changes induced by river training structures: Bandal- like structures and groins. *Kyoto University Disaster Prevention Research Institute Annual Report B*, 53(B):595–606.

Tyler, A., Svab, E., Preston, T., Présing, M., and Kovács, W. (2006). Remote sensing of the water quality of shallow lakes: A mixture modelling approach to quantifying phytoplankton in water characterized by high- suspended sediment. *International Journal of Remote Sensing*, 27(8):1521–1537.

USEPA (2008). *National Coastal Condition Report III/U.S. Environmental Protection Agency, Office of Water, and Office of Research and Development.* U.S. Environmental Protection Agency, Office of Research and Development, Office of Water, Washington, D.C.

Vanhellemont, Q. (2020). Automated water surface temperature retrieval from LANDSAT 8/TIRS. *Remote Sensing of Environment*, 237:1–10.

Vapnik, V. (2013). *The Nature of Statistical Learning Theory*. Springer New York.

Vermeulen, B., Boersema, M., Hoitink, A., Sieben, A., Sloff, K., and Wal, M. (2018). Scale model of a training dam using lightweight granulates. *E3S Web of Conferences*, 40:1–7.

Vincent, R. K. (1972). An ERTS multispectral scanner experiment for mapping iron compounds. In *Proceedings of the Eleventh International Syposium on Remote Sensing of Environment*, pages 1239–1247.

Wal, M. (2020). Bank protection structures along the Brahmaputra- Jamuna river, a study of flow slides. *Water*, 12:1–28.

Wicaksono, P. (2017). Mangrove above- ground carbon stock mapping of multi-resolution passive remote-sensing systems. *International Journal of Remote Sensing*, 38(6):1551–1578.

Wicaksono, P. and Hafizt, M. (2013). Mapping seagrass from space: Addressing the complexity of seagrass LAI mapping. *European Journal of Remote Sensing*, 46:18–39.

Wicaksono, P. and Hafizt, M. (2018). Dark target effectiveness for dark-object subtraction atmospheric correction method on mangrove above-ground carbon stock mapping. *The Institution of Engineering and Technology Image Processing*, 12(4):582–587.

Wilcox, D. C. (1988). Reassessment of the scale-determining equation for advanced turbulence models. *American Institute of Aeronautics and Astronautics Journal*, 26:1299–1310.

Wilcox, D. C. (1993). Comparison of two-equation turbulence models for boundary layers with pressure gradient. *American Institute of Aeronautics and Astronautics Journal*, 31(8):1414–1421.

Wilcox, D. C. (1994). Simulation of transition with a two-equation turbulence model. *American Institute of Aeronautics and Astronautics Journal*, 32(2):247–255.

Wilson, C. (2007). Flow resistance models for flexible submerged vegetation. *Journal of Hydrology*, 342(3- 4):213–222.

Wilson, C., Stoesser, T., Bates, P., and Pinzen, A. B. (2003). Open channel flow through different forms of submerged flexible vegetation. *Journal of Hydraulic Engineering*, 129(11):847–853.

Wolanin, A., Rozanov, V., Dinter, T., Noël, S., Vountas, M., Burrows, J., and Bracher, A. (2015). Global retrieval of marine and terrestrial chlorophyll fluorescence at its red peak using hyperspectral top of atmosphere radiance measurements: Feasibility study and first results. *Remote Sensing of Environment*, 166:243–261.

Xu, H. (2006). Modification of normalised difference water index (NDWI) to enhance open water features in remotely sensed imagery. *International Journal of Remote Sensing*, 27(14):3025–3033.

Yoo, K. (2003). Nature friendly river training structure using groynes. In *Water Resources Research Department, Korean Institute of Construction Technology, Korea.*

Zhao, B., Ren, Y., Gao, D., and Xu, L. (2019a). Performance ratio prediction of Photovoltaic pumping system based on Grey Clustering and Second Curvelet Neural Network. *Energy*, 171:360–371.

Zhao, B., Ren, Y., Gao, D., and Xu, L. (2019b). Prediction of Service Life of Large Centrifugal Compressor Remanufactured Impeller Based on Clustering Rough Set and Fuzzy Bandelet Neural Network. *Applied Soft Computing*, 78(C):132–140.

Zhao, B., Ren, Y., Gao, D., Xu, L., and Zhang, Y. (2019c). Energy utilization efficiency evaluation model of refining unit Based on Contourlet neural network optimized by improved grey optimization algorithm. *Energy*, 185:1032–1044.

Zolfagharpour, F., Saghafian, B., and Delavar, M. (2022). Hydrological alteration and biodiversity change along the river network caused by anthropogenic activities and climate variability. *Ecological Processes*, 11:11–19.